

2009

# Laser microfabrication and testing of silicon carbide diaphragms for MEMS applications

Benjamin Pecholt  
*Iowa State University*

Follow this and additional works at: <https://lib.dr.iastate.edu/etd>

 Part of the [Mechanical Engineering Commons](#)

## Recommended Citation

Pecholt, Benjamin, "Laser microfabrication and testing of silicon carbide diaphragms for MEMS applications" (2009). *Graduate Theses and Dissertations*. 11989.

<https://lib.dr.iastate.edu/etd/11989>

This Thesis is brought to you for free and open access by the Iowa State University Capstones, Theses and Dissertations at Iowa State University Digital Repository. It has been accepted for inclusion in Graduate Theses and Dissertations by an authorized administrator of Iowa State University Digital Repository. For more information, please contact [digirep@iastate.edu](mailto:digirep@iastate.edu).

**Laser microfabrication and testing of silicon carbide diaphragms for MEMS applications**

by

**Benjamin Francis Pecholt**

A thesis submitted to the graduate faculty  
in partial fulfillment of the requirements for the degree of  
**MASTER OF SCIENCE**

Major: Mechanical Engineering

Program of Study Committee:  
Pal Molian, Major Professor  
Liang Dong  
Xinwei Wang

Iowa State University

Ames, Iowa

2009

Copyright © Benjamin Francis Pecholt, 2009. All rights reserved.

## TABLE OF CONTENTS

TABLE OF CONTENTS.....	ii
LIST OF FIGURES .....	v
LIST OF TABLES .....	viii
ACKNOWLEDGEMENTS .....	ix
CHAPTER 1. INTRODUCTION .....	1
1.1. Problem Statement.....	2
1.2. Research Objectives .....	2
1.3. Experimental Setup.....	4
References.....	6
CHAPTER 2. BACKGROUND .....	7
2.1. MEMS Pressure Sensors .....	8
2.1.1. Capacitive Sensor.....	11
2.1.2. Piezoresistive Sensor .....	11
2.2. Silicon Carbide MEMS Overview.....	12
2.3. Silicon Carbide Properties .....	12
2.4. Conventional Silicon Carbide Bulk Micromachining Techniques.....	15
2.4.1. Electrochemical Etching of SiC.....	16
2.4.2. High-Density Plasma Etching of SiC .....	18
2.5. Silicon Carbide MEMS Pressure Sensor Fabrication.....	21
2.6. Laser Micromachining.....	22
References .....	22
CHAPTER 3. A REVIEW OF LASER MICROSCALE PROCESSING OF SILICON CARBIDE.....	26
3.1. Abstract.....	26
3.2. Introduction .....	26
3.3. Overview of SiC Laser Processing.....	27
3.4. Additive Laser Processing.....	34
3.4.1. Doping and Annealing of Silicon Carbide.....	34
3.4.2 Metallization of SiC Substrates .....	38

3.4.3. Pulsed Laser Deposition of Silicon Carbide Thin Films .....	39
3.4.4. Nanoparticle formation .....	41
3.5. Subtractive Laser Processing.....	42
3.6. Conclusion .....	46
Acknowledgements .....	47
References .....	47
<b>CHAPTER 4. ULTRAFAST LASER MICROMACHINING OF 3C-SIC THIN FILMS FOR MEMS DEVICE FABRICATION .....</b>	<b>61</b>
4.1. Abstract.....	61
4.2. Introduction .....	62
4.3. Experimental details .....	65
4.4. Results and discussion .....	66
4.5. Conclusions .....	85
Acknowledgements .....	86
References .....	86
<b>CHAPTER 5. RAPID PROTOTYPING OF BULK 6H-SIC MEMS STRUCTURES USING A Q-SWITCHED ND:YAG LASER.....</b>	<b>93</b>
5.1. Abstract.....	93
5.2. Introduction .....	93
5.3. Experimental Details .....	96
5.4. Results and Discussion .....	98
5.5. Conclusions .....	109
Acknowledgements .....	110
References .....	110
<b>CHAPTER 6. MECHANICAL BEHAVIOR OF LASER MICROMACHINED 6H-SIC DIAPHRAGMS .....</b>	<b>114</b>
6.1. Introduction .....	114
6.2. Experimental Details .....	115
6.3. Numerical Models for Diaphragm Deflection.....	119
6.4. Pressure Testing Results.....	123
6.5. Micro Indentation Testing Results .....	126
6.6. Conclusions .....	130
References .....	131
<b>CHAPTER 7. CONCLUSIONS AND RECOMMENDATIONS FOR FUTURE WORK .</b>	<b>133</b>

7.1. Summary.....	133
7.2. Uncertainties of Laser Micromachining of MEMS components.....	134
7.3. Mechanical Consistency of Diaphragms .....	136
7.4. Laser System Considerations for Faster Production.....	137
7.5. Sensor Design and Implementation .....	137
7.6. High Temperature Pressure Testing .....	138
APPENDIX A. LASER BEAM CALCULATIONS .....	141
A.1. Spot Size .....	141
A.2. Depth of Focus.....	141
APPENDIX B. DIAPHRAGM DEFLECTION EQUATIONS .....	143
B.1. Diaphragm Deflection under Uniform Loading (Hinged Boundary Condition) .....	144
B.2. Diaphragm Stiffness under Concentrated Loading (Hinged Boundary Condition)...	145
APPENDIX C. DIAPHRAGM DEFLECTION EQUATIONS .....	147
C.1. Diaphragm Deflection under uniform Loading (Hinged Boundary Condition) .....	148
C.2. Diaphragm Stiffness under Concentrated Loading (Hinged Boundary Condition)...	149
APPENDIX D. PRESSURE TESTING APPARATUS OPERATIONAL NOTES .....	151
D.1. DVRT Specifications.....	151
D.2. DVRT Apparatus .....	152
D.3. Pressure Vessel Apparatus.....	155
APPENDIX E. Nd:YAG MICROMACHINING OF 3C-SIC THIN FILM CANTILEVERS	160
E.1. Introduction .....	160
E.2. Experimental Details.....	160
References .....	166

## LIST OF FIGURES

Figure 1. Schematic of pressure sensor operation .....	10
Figure 2. Silicon Carbide polytype stacking sequences [1].....	13
Figure 3. 6H-SiC Diaphragm fabricated using electrochemical etching [27] (Reprinted from Sensors and Actuators A v112, 1, p.36-43 copyright 2004 with permission from Elsevier) .	18
Figure 4. Inductively coupled plasma (ICP) system schematic with two independent RF generators [23] .....	19
Figure 5. Deep Reactive Ion Etch of 6H-SiC to create a diaphragm structure following an in situ Ar ion etch.....	21
Figure 6. ArF laser micromachined trench on amorphous SiC [116]. (Reprinted from Sensors and Actuators A v136, 2, p.554-563 copyright 2007 with permission from Elsevier) .....	43
Figure 7. Femtosecond laser micromachined rotor in 3C-SiC thin films deposited on silicon before and after partial release from substrate [31] .....	46
Figure 8. Single-shot ablation rates of 3C-SiC thin films.....	67
Figure 9. Microchannels generated by (a) 120-fs laser (b) 90-ns laser under identical conditions: pulse energy 60 $\mu\text{J}$ , spot size 4 $\mu\text{m}$ , speed 1000 $\mu\text{m s}^{-1}$ . .....	69
Figure 10. Femtosecond micromachined holes in 3C-SiC thin film deposited on silicon at a speed of 1000 $\mu\text{m s}^{-1}$ ; (a) 750 $\mu\text{J}$ (b) 500 $\mu\text{J}$ (c) 250 $\mu\text{J}$ .....	72
Figure 11. Femtosecond laser micromachined holes in 3C-SiC thin films deposited on silicon with 30 pulses (a) 50 $\mu\text{J}$ (b) 200 $\mu\text{J}$ .....	72
Figure 12. Femtosecond laser micromachined channels in 3C-SiC thin films deposited on silicon at a speed of 20 (a) 5 $\mu\text{J}$ ; (b) 2.5 $\mu\text{J}$ ; (c) 1.5 $\mu\text{J}$ .....	73
Figure 13. Femtosecond laser micromachined rotor in 3C-SiC thin films deposited on silicon (a) 60 $\mu\text{J}$ ; (b) 8 $\mu\text{J}$ .....	75
Figure 14. High-magnification views of the center section of rotor displayed on Figure 6 (b) .....	76
Figure 15. Femtosecond laser micromachined microrotor in 3C-SiC thin films deposited on silicon (a) after laser ablation (b) after subsequent etching in Koh .....	77
Figure 16. Femtosecond laser micromachined channel at pulse energy of 1.2. Note the formation of 50-100 nm diameter nanoparticles at the edge (a) microchannel (b) edge of microchannel.....	78
Figure 17. Femtosecond laser micromachined channel at a pulse energy of 0.06 (a) microchannel (b) structures within the microchannel.....	79
Figure 18. Femtosecond laser micromachined rotor in 3C-SiC thin films deposited on silicon using a pulse energy of 1.2 $\mu\text{J}$ (a) Rotor; (b) Magnified view of central portion .....	80
Figure 19. Single-shot, femtosecond laser micromachined region in 3C-SiC thin films deposited on silicon (pulse energy = 0.5 $\mu\text{J}$ ).....	81
Figure 20. X-ray diffraction spectra of 3C-SiC films of (a) CVD thin film and (b) Laser nanostructured thin film.....	82
Figure 21. Auger electron spectra of 3C-SiC films: (a) Laser-irradiated at 0.45 J cm; (b) Laser irradiated and then Ar-ion etched; (c) Un-irradiated .....	83
Figure 22. XYZ microstepper and microminiature DVRT setup used to measure the profile depth of the machined regions .....	98

Figure 23. Schematic of the laser processing a) laser micromachining of the rough side of the wafer b) laser micromachining of the polished side indicated intermittent transmittence.	100
Figure 25. A pictorial representation of a single ‘pass’ made while laser machining with the XY table	101
Figure 24. Ablation depth as a function of energy density for a single laser trace during scribing at a scan speed of $1 \text{ mm s}^{-1}$ , 3 kHz machining on the backside	101
Figure 26. Diaphragm structure immediately after laser micromachining with an intentional plough mark of the surface material	103
Figure 27. Laser micromachined structure with three tier levels after chemical etching a) stereoscopic view b) closeup of the bottom structure	105
Figure 28. Effect of diaphragm size on the machining time	107
Figure 29. Effect of diaphragm size on the unit area covered per second	107
Figure 30. Ultra-short pulse laser micromachined circular diaphragm with $500 \mu\text{m}$ diameter and $200 \mu\text{m}$ depth	109
Figure 31. Normal quantile plot for the depth of a diaphragm machined at 0.35 W average power, overlap $10 \mu\text{m}$ , $1\text{mm/s}$ scan speed, and 4 passes	116
Figure 32. Schematic of the DVRT pressure testing apparatus	117
Figure 33. Schematic of the DVRT measuring the location of the diaphragm under left) no load right) with a pressurized load	118
Figure 34. Deflection versus thickness for a $2.5 \times 2.5 \text{ mm}$ diaphragm under a distributed load	121
Figure 35. Deflection versus diaphragm thickness for a $1.5 \times 1.5 \text{ mm}$ diaphragm with a hinged boundary condition	122
Figure 36. Deflection versus diaphragm thickness for a $1.5 \times 1.5 \text{ mm}$ diaphragm with a clamped boundary condition	123
Figure 37. Pressure Testing Data for Sample 1 ( $2.5 \times 2.5 \text{ mm}$ diaphragm)	124
Figure 38. Pressure Testing Data for Sample 2 ( $1.5 \times 1.5 \text{ mm}$ diaphragm)	125
Figure 39. Test 1 of Sample 3 (maximum load 0.5 N)	127
Figure 40. Test 2 of Sample 3 (maximum load of 2.0 N)	127
Figure 41. Test 3 of Sample 3 (maximum load of 3.0 N)	128
Figure 42. Test 4 of Sample 3 (maximum load of 4.0 N)	128
Figure 43. Test 5 of Sample 3 which resulted in fracture of the diaphragm structure (maximum load of 5.0 N)	129
Figure 44. DVRT pressure testing apparatus	153
Figure 45. DVRT pressure testing apparatus schematic	154
Figure 46. DVRT operational Schematic	155
Figure 47. Pressure vessel used for testing the diaphragms	157
Figure 48. Pressure vessel and DVRT apparatus	158
Figure 49. Feedthrough used on the apparatus	159
Figure 50. Laser passes on 3C-SiC A) $1 \text{ mm s}^{-1}$ B) $5 \text{ mm s}^{-1}$ C) $7 \text{ mm s}^{-1}$ D) $9 \text{ mm s}^{-1}$	161
Figure 51. Cantilever micromachining schematic	162
Figure 52. Laser micromachined cantilever before release	163
Figure 53. Cantilever structure after release	164

Figure 54. Cantilever micromachining schematic with duplicated passes to improve the edge quality ..... 164  
Figure 55. Microscope image of a 3C-SiC cantilever fabricated using the finishing passes and released using the anisotropic etch..... 165

## LIST OF TABLES

Table 1. Project Objectives .....	3
Table 2. Electrical properties of silicon carbide .....	14
Table 3. Mechanical properties of silicon carbide .....	15
Table 4. Laser processing applications for silicon carbide .....	30
Table 5. Optical absorption for excimer lasers .....	31
Table 6. Surface enrichment and modification of SiC.....	33
Table 7. Diffusion coefficients .....	36
Table 8. Pulsed laser deposited parameters .....	40
Table 9. Laser ablation rates .....	44
Table 10. Optical properties of silicon carbide with common lasers.....	96
Table 11. Laser micromachining parameters and the resulting roughness and depth of removed material for a scan rate of $1 \text{ mm s}^{-1}$ .....	104
Table 12. Laser micromachining parameters and the theoretical material removal rate for $0.5 \times 0.5 \text{ mm}$ and $1 \times 1 \text{ mm}$ square diaphragms .....	108
Table 13. Diaphragm process parameters .....	115
Table 14. Pressure Testing fit data and estimated diaphragm thickness.....	125
Table 15. Micro indentation tests conducted on Sample 3 .....	126
Table 16. Diaphragm thickness calculated from the slope from Tests 1-5 with clamped and hinged boundary conditions.....	130
Table 17. 3C-SiC cantilever structure indentation testing.....	166

## ACKNOWLEDGEMENTS

I truly appreciate having had the opportunity to work on this project and the personal growth and knowledge I gained working on it. I owe a special debt of gratitude to my major advisor Dr. Molian for his support and guidance in this project. His willingness to allow me the freedom to explore various aspects of this project is a true testament to his great patience. I would like to thank Yaunyaun Dong for laying the ground work for this research in her thesis and for her experimental contributions made to chapter 4 of this report.

Thank you to Xinwei Wang and Liang Dong for supporting me by being a part of my program of study and reviewing my work.

Thank you to Dr. Byrd for lending the pressure vessel for the experimentation used in testing the samples in the pressurized environment, and to Dr. Shrotriya for loaning use of the DAQ system used for pressurized tests and for his guidance in area of membrane modeling. I would like to thank Jim Dautremont for helping to maintain and troubleshoot the laser equipment and for patiently assisting me on numerous occasions. The efforts of Larry Couture and Gaylord Schandrett are greatly appreciated for maintaining the Mechanical Engineering student shop and making it convenient for my usage.

Thank you to Quantronix Laser for their assistance in the production of the Laser micromachined diaphragm used in Chapter 5 and MTS Nano for their testing support of the cantilevers tested in Appendix D of this report. Thanks are also due to Dr. Chris Zorman of Case Western Reserve University for providing CVD deposited thin film wafers.

I am also grateful to the National Science Foundation (NSF) for supporting this research work under the grant CMMI-0619115 and finally a special thanks to the US taxpayers that makes this work and other work like it possible.

## CHAPTER 1. INTRODUCTION

MicroElectroMechanical Systems (MEMS) are increasingly becoming an integral part of daily life with many uses in popular consumer electronics, industrial applications, and biomedical applications as sensors, actuators, and resonators. MEMS devices will continue to be highly desirable because of their compact size, functionality, and cost compared to conventional devices.

MEMS devices are typically based on conventional materials used in the integrated circuit (IC) industry where the most common material is silicon. Many of these materials are not suitable for applications in high temperature and harsh environments. Silicon carbide on the other hand is a material that has grown interest because of developments that have led to the ability to grow bulk single crystalline wafers and deposit single crystalline thinfilms. Silicon carbide is well suited for such applications due to its highly robust thermal, mechanical and electronic properties [1-3]. One specific niche application is the MEMS pressure sensor which if developed on a commercial scale would rapidly find many applications in power generation, aerospace applications, engine diagnostics, chemical processing and many others.

While silicon carbide remains a favored material for harsh environment pressure sensors due to its properties, its extreme inertness has lead to difficulties in bulk micromachining deep structures  $>100 \mu\text{m}$ . To date the best means of fabricating diaphragm structures suitable for MEMS applications suffer from low etch rates on the order of  $1 \mu\text{m min}^{-1}$  and poor selectivity. Laser micromachining has been realized as a means of fabricating many devices [4-8]. Some examples of lasers successfully micromachining bulk single

crystalline silicon carbide for via hole formation [4-7] and for diaphragms [8]. Should laser micromachining become a viable fabrication method, it may allow for rapid prototyping and the achievement of structures not yet realized with conventional methods.

### **1.1. Problem Statement**

To investigate the viability of various lasers for the microfabrication of single crystalline SiC diaphragms suitable for MEMS pressure sensor devices.

### **1.2. Research Objectives**

This research is funded by NSF grant CMMI-0619115 where the original research objectives from the NSF grant proposal included plans to use bulk 3C-SiC and femtosecond lasers which had to be modified for the practical purposes, i.e. 3C-SiC is not commercially available and other laser systems were found to be useful for machining bulk SiC. The modified objectives used in this paper compared to the original objectives are shown in Table 1.

**Table 1. Project Objectives**

Original Objective	Proposal Objectives	Actual Objective/Result	Reason for Change
1	Use "non-thermal" ultrashort pulsed lasers to produce membranes	Use nanosecond pulsed lasers to produce membranes	Nanosecond lasers are a mature technology and offer a greater system stability than existing ultrashort lasers. Success has been shown in the literature for Nd:YAG and Excimer lasers in nanosecond pulses
1	Produce circular membranes	Produce Square diaphragms	Square diaphragms are more easily produced using the square shaped Excimer laser. Additionally square machining was found to be more easily achieved using the Nd:YAG laser (see Chapter 5 for details)
1	Bulk micromachine 3C-SiC	Bulk micromachine 4H-SiC and 6H-SiC	Bulk single crystalline 3C-SiC wafers are not commercially available and recent success in 4H-SiC and 6H-SiC pressure sensors indicates that results of laser micromachining could be easily integrated to existing technology
1	Integrate piezoresistive strain gauge and temperature compensation.	-	Piezo resistive strain gauges on 4H-SiC and 6H-SiC are a well studied technology and are not studied in this report
2	Understand the fundamental interactions (ablation mechanisms) between the femtosecond pulsed laser and 3C-SiC at 800-nm wavelength	Understand the fundamental interactions (ablation mechanisms) between the UV Excimer and Nd:YAG pulsed laser and 4H-SiC and 6H-SiC at 248 and 1064 nm, respectively	
3	Determine etch profile, etch rate, undercutting, precision, tolerance, surface roughness and volume production for SiC membranes.	*	
4	Develop the pressure sensors by integrating all circuit elements onto a monolithic chip	-	The electronic fabrication for 4H-SiC and 6H-SiC pressure sensors are understood and have been shown by others
4	Determining process control requirements and methods for diaphragm reproducibility, high temperature contact and pad materials, and packaging with aluminum nitride (AlN).	-	Further statistical studies are required to validate the process control of laser micromachining.
5	Pressure-test MEMS the sensors up to 1000 psi for temperatures up to 800°C so as to use in a variety of energy related applications.	-	Pressure testing was carried out independent of the electronics to characterize the diaphragm only

- indicates the objective was not yet obtained

\* indicates the objective was not changed and obtained

### 1.3. Experimental Setup

#### **Nd:YAG Laser**

Series 700 Lee Laser

Q-switched

$\lambda = 1064 \text{ nm}$

Repetition Rate: 1.5-50 kHz

Pulse Width:  $< 100 \text{ ns}$

Max Average Power 8W

Lenses:

A Plano-Convex lens (EFL 65 mm)

Reflective Objective : 25x magnification, 8.0 mm FL, 0.4 NA., 14.5 mm WD.

#### **Femtosecond Laser**

Spectra Physics Hurricane X

Chirped Pulse Amplification

$\lambda = 800 \text{ nm}$

Repetition Rate: 1 kHz

Pulse Width: 120 fs

Lens: Reflective Objective Lens

#### **XY Table**

LabMotion (Coherent, Inc.) Series 640 Linear Motion

Linear Travel: 50mm

Max Speed  $10 \text{ mm s}^{-1}$

Minimum Resolution: 1  $\mu\text{m}$

Repeatability: 5  $\mu\text{m}$

### **XYZ Table**

Newmark Systems

Linear Travel: 50 mm (X,Y) and 25.4 mm (Z)

Minimum Resolution: 0.02  $\mu\text{m}$

Repeatability: 5  $\mu\text{m}$

### **Profilometer**

Dektak II Surface Profilometer

### **Differential Voltage Reluctance Transducer (DVRT)**

Model M-DVRT-PE-3

Plunger Length: 3 mm

Resolution: 1.5  $\mu\text{m}$

Repeatability: 1.0  $\mu\text{m}$

### **Pressure Vessel**

1 Gallon capacity Autoclave reactor

Snap-Tite, Inc.

## References

1. Mehregany, M. and C.A. Zorman, *SiC MEMS: opportunities and challenges for applications in harsh environments*. Thin Solid Films, 1999. **355-356**: p. 518-524.
2. *The MEMS Handbook*, ed. M. Gad-el-Hak. 2002, Boca Raton, FL, USA: CRC Press.
3. Beheim, G.M., *Deep Reactive Ion etching for Bulk Micromachining of Silicon Carbide*, in *The MEMS Handbook*, M. Gad-el-Hak, Editor. 2002, CRC Press: Boca Raton, FL, USA.
4. Anderson, T.J., et al., *Comparison of Laser-Wavelength Operation for Drilling of Via Holes in AlGaIn/GaN HEMTs on SiC Substrates*. Journal of Electronic Materials, 2006. **35**(4): p. 675-679.
5. Zoppel, S., et al., *Laser micro machining of 3C-SiC single crystals*. Microelectronic Engineering, 2006. **83**: p. 1400-1402.
6. Farsari, M., et al., *Efficient femtosecond laser micromachining of bulk 3C-SiC*. Journal of Micromechanical Microengineering, 2005. **15**: p. 1786-1789.
7. Anderson, T., et al., *Laser ablation of via holes in GaN and AlGaIn/GaN high electron mobility transistor structures*. Journal of Vacuum Science Technology B, 2006. **24**(5): p. 2246-2249.
8. Dong, Y., in *Mechanical Engineering*. 2003, Iowa State University: Ames, IA, USA.

## CHAPTER 2. BACKGROUND

MicroElectroMechanical Systems (MEMS) are devices that integrate both electrical and mechanical components with characteristic feature lengths in the range of 1 to 1000  $\mu\text{m}$  to perform the functions of microscopic machines. MEMS devices take advantage of the electrical and mechanical properties of materials to perform the tasks of sensing, switching, and actuation which has led to a diverse number of applications such as automobile airbag deployment sensors, projector micro mirror arrays, optical switches, inkjet nozzles, and biological, chemical sensors, and many more [2]. Today, with the expansion of MEMS applications, the MEMS market has grown to a multi-billion dollar industry with 200-300 different companies worldwide involved in their manufacture [3]. In 2007 the global market for MEMS systems reached \$8 billion and it is expected to grow to \$9.86 billion by 2010 [3].

MEMS devices are fabricated using techniques borrowed from the integrated circuit (IC) industry which allows for integration of mechanical components and integrated circuitry. The nature of the fabrication process has led to an early adoption of silicon as the material of choice for MEMS devices; however, this is changing as new fabrication techniques for different materials are explored. The conventional fabrication techniques are heavily dependent upon masking and lithographic patterning techniques but also include: deposition of sacrificial layers, anisotropic and isotropic chemical etching of select layers, thermal diffusion and ion implantation of impurities. MEMS device fabrication begins with a so-called substrate typically made from silicon with thickness (200-400)  $\mu\text{m}$  and thin layers commonly referred to as thin films ( $<10 \mu\text{m}$ ) are added to the substrate through various deposition or oxidation processes. With the process of lithographic patterning, and etching of

selective sacrificial layers, these deposited layers can be patterned with material specific etch processes to allow for a great complexity of structures and devices. Typically when the bulk substrate is being etched, it is referred to as bulk micromachining which is a commonly used phrase in this report from this point onward. The patterning of thin films and sacrificial layers is known as surface micromachining and will also be referenced from here on. These processes are widely used for MEMS fabrication because they allow for large batch fabrication and the seamless integration of monolithic mechanical and electrical components.

The small size of MEMS components allows exploitation of scaling laws to create devices that would be impractical on a larger size scale. Micron sized components are susceptible to forces that are negligible at larger scales such as Coulomb forces and adhesive stiction forces while the effects of gravity play less important role due to their low masses. Lower mass and high surface area also means that MEMS components can be rapidly heated and cooled. Common forms of actuation for MEMS components includes electrostatic and thermally actuated components. Similarly other scaling laws have been utilized to create an array of ingenious devices that take advantage of the small size of MEMS devices.

## **2.1. MEMS Pressure Sensors**

There are numerous MEMS devices that fall into the category of MEMS sensors such as accelerometers, gyroscopes, and pressure sensors; however none have been as successful as the MEMS pressure sensor which was the harbinger of MEMS technology. The first silicon MEMS pressure sensor was fabricated by Honeywell in the 1960s and by the 1980s the MEMS pressure sensors were a highly successful commercial product [4]. The long

history of the MEMS pressure sensor has led to its design evolution and adaption for a wide range of industries from aerospace to biomedical [4, 5].

MEMS sensors can vary in complexity but their systems use three fundamental sub-systems that include: an actuator, a transducer, and signal conditioning. There are numerous types of MEMS pressure sensors; however the most common technique is the diaphragm based pressure sensor which has as its fundamental component, a thin flexible diaphragm that deflects (actuator) when there is a pressure applied across the two sides of the diaphragm. A diaphragm deflecting under an applied pressure can be seen in Figure 1. The diaphragm acts as the actuator while the resistance or capacitance change acts as the transducer and the output is measured by some signal conditioning circuitry as in conventional pressure transducers. There are various schemes of designing the sensor that allow for different reading types: absolute that measures the pressure against a vacuum reference, gauge pressure that measures the pressure against atmosphere and differential that measures two pressures relative to each other.

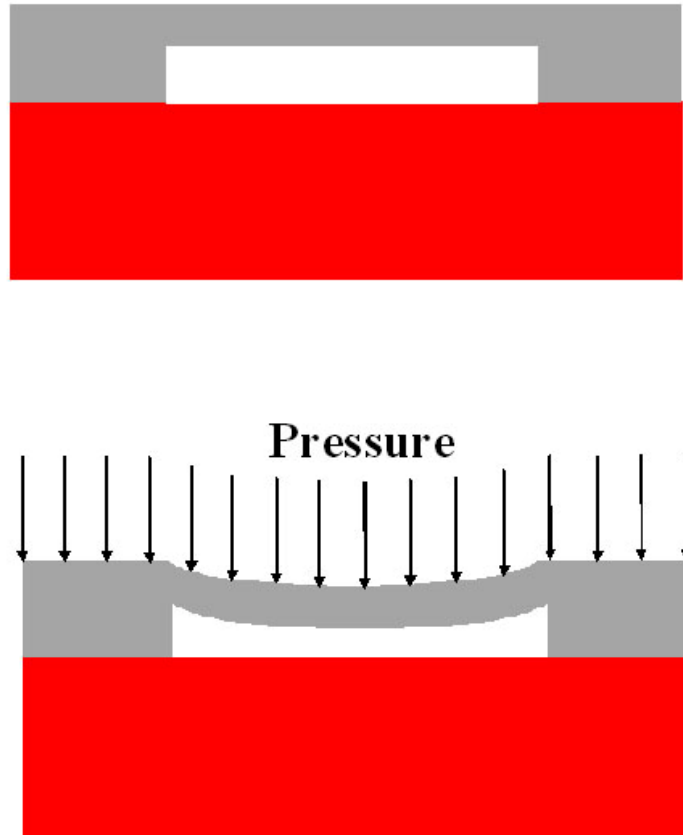


**Figure 1. Schematic of pressure sensor operation**

The pressure sensor diaphragm is modeled using the fundamental Navier elastic body equation while applying a variety of geometries and boundary conditions. As a general rule the diaphragms are modeled as thin plate with hinged boundary conditions [5]. For more information on the use of the Navier equation as it pertains to a square diaphragm refer to Chapter 6. Using the solution to the Navier equation a relationship can be developed between the deflection and stress induced on the surface of the diaphragm which is the basis for the two primary kinds of diaphragm sensors: the capacitive-type sensor and the piezoresistive-

type sensors respectively. The capacitive sensor measures the change in deflection while the piezo-resistive measure the induced stress.

### **2.1.1. Capacitive Sensor**

The capacitive-type sensor operates by measuring the capacitance between the membrane and an unmoving substrate that forms a system of two electrodes. As pressure is applied to the system, the diaphragm bends towards the electrode and reduces the effective gap and changes the capacitance. The capacitive sensor is advantageous over the piezoresistive type sensor because it can be scaled to smaller sizes and has less dependence upon the dimensional tolerance of the piezoresistors [5]. The disadvantage of the capacitive type sensor is that the capacitance change is non-linear and large device impedance requires that the signal conditioning circuitry to be integrated close to the sensor device [5].

### **2.1.2. Piezoresistive Sensor**

The most common piezoresistive-type pressure sensor is made from bulk silicon where an anisotropic etch is used to fabricate the diaphragm and conductive traces are built into the diaphragm surface using a doping process [5]. The piezoresistive effect is a property of crystalline materials whereby resistance changes when a stress is applied caused by shifting in the crystal structure which modifies the flow of current. The piezoresistive-type sensor takes advantage of this effect and by measuring the strain induced on the surface of the diaphragm by measuring the change in resistance. The piezoresistors are arranged in a bridge circuit that allows for a linear voltage output as a function of the change in resistance. The piezoresistive effect is also affected by temperature and can lead to an imbalance on the

circuit bridge if not properly accounted for which becomes problematic for applications with a large temperature variation.

## 2.2. Silicon Carbide MEMS Overview

Silicon carbide MEMS are a relatively new area in the MEMS field and is being driven by the highly desirable properties of silicon carbide that make it an ideal candidate for high voltage and harsh environment applications such as: RF MEMS, optical MEMS, accelerometers, and pressure sensors [6]. RF MEMS applications include RF switches, micromechanical resonators, and filters [7] which are attractive due to the ability operate at higher frequency, power density, and reliability in comparison to conventional silicon devices. Accelerometers and pressure sensors made of silicon carbide are highly desirable for niche applications in high temperature and harsh environments. Accelerometers could likely find usage in high temperature combustion and turbine engines and pressure sensors capable of harsh environments would be advantageous for oil drilling applications [6].

## 2.3. Silicon Carbide Properties

Silicon carbide exhibits robust mechanical and chemical stability making it inert to most etchants, and in comparison to Silicon, more exotic methods of fabrication are required to fabricate MEMS structures. For this reason it is unlikely that silicon carbide based MEMS pressure sensors will ever achieve the same ubiquity as the silicon based devices, nevertheless niche applications that can only be met by higher performance materials will persist.

There are over 250 known silicon carbide polytypes where the polytype is defined by the variations in planar stacking of the Si-C bilayers. The stacking orientation of 3C (ABC), 4H (ABAC), and 6H (ABCACB) respectively are shown in Figure 2.

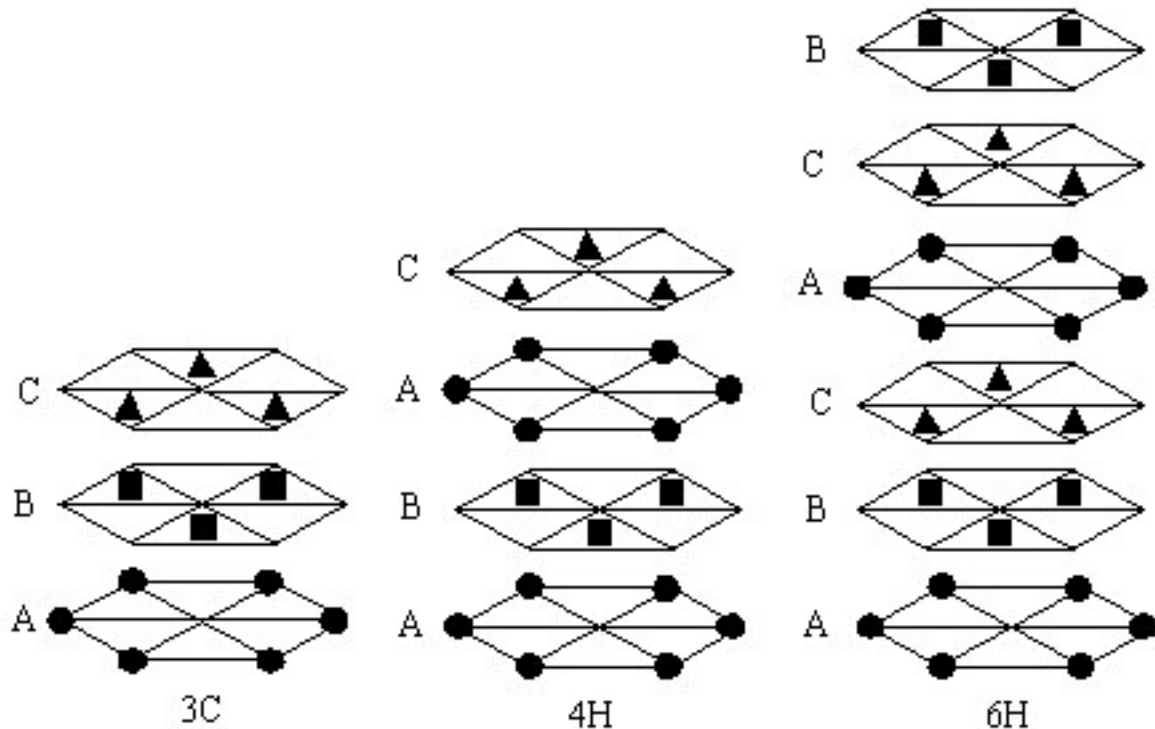


**Figure 2. Silicon Carbide polytype stacking sequences [1]**

However, only the 3C, 4H, and 6H polytypes can be grown as single crystal SiC and are therefore of practical importance for microelectronics and MEMS applications. 4H and 6H substrates are commercially available as wafers up to 100 mm diameter. Work is still progressing for 3C wafers, however 3C-SiC has the versatility of being deposited via Chemical Vapor Deposition (CVD). 3C-SiC can be deposited as polycrystalline SiC (poly-SiC) on  $\text{SiO}_2$  and  $\text{Si}_3\text{N}_4$  substrates [8] or can be grown as a heteroepitaxial single crystalline film on Si wafers [9-11]. Similarly, amorphous SiC films can be deposited using CVD

techniques. Properties vary significantly between polytypes [12] such as carrier mobility and electronic bandgap. Only 3C-SiC exhibits anisotropic properties and has higher saturation velocity, and lower band gap (2.3 eV) compared to 4H-SiC (3.2 eV) and 6H-SiC (3.0 eV) [1]. Due to the difficulties in growing bulk single crystalline 3C-SiC, it has yet to be made commercially available, but ongoing research has led to limited supply of bulk single crystal wafers with polished surfaces [13, 14]. In terms of bulk single crystals 4H-SiC is typically favored for microelectronics applications over 6H-SiC because of its higher carrier mobility. Electronic properties of SiC compared to silicon are listed in Table 2.

**Table 2. Electrical properties of silicon carbide**

	Si	3C-SiC	4H-SiC	6H-SiC
Band Gap (eV)	1.12 [1]	2.36 [15]	3.23 [1, 15]	3.0 [1, 15]
Breakdown field (V cm <sup>-1</sup> )	3 x 10 <sup>5</sup>	10 <sup>6</sup> [15]	(3 ÷ 5) x 10 <sup>6</sup> [15]	(3 ÷ 5) x 10 <sup>6</sup> [15]
Static Dielectric Constant	11.9 [1]	9.72 [1, 15]	Typically values for 6H used [15]	$\perp$ c-axis 9.66 [15] $\parallel$ c-axis 10.03
Electron Mobility	1350 [1]	1000 [1]	$\perp$ c-axis 950 [1] $\parallel$ c-axis 1150	$\perp$ c-axis 500 [1] $\parallel$ c-axis 100
@ Nd = 10 <sup>16</sup> cm <sup>-3</sup> (cm <sup>2</sup> V <sup>-1</sup> s <sup>-1</sup> )				
Hole Mobility	480 [1]	40 [1]	120 [1]	90 [1]
@ Nd = 10 <sup>16</sup> cm <sup>-3</sup> (cm <sup>2</sup> V <sup>-1</sup> s <sup>-1</sup> )				
Saturation Velocity (10 <sup>7</sup> cm s <sup>-1</sup> )	1.0 [1]	2.5 [1]	2.0 [1]	2.0 [1]

SiC has also been attractive for MEMS applications due to its favorable mechanical properties including high wear resistance, stiffness, and hardness; these properties have already led to the widespread use of SiC in industrial applications such as tools and abrasives. SiC is comparable to other hard materials such as diamond and Al<sub>2</sub>O<sub>3</sub>. Its hardness

on the Moh's scale (9) is similar to that of  $\text{Al}_2\text{O}_3$  (9) [16]. In terms of Knoop hardness SiC ( $2480 \text{ kg/mm}^2$ ) is also comparable to  $\text{Al}_2\text{O}_3$  ( $2100 \text{ kg/mm}^2$ ) and is approximately three times greater than silicon [16]. In addition to its ability to be used under harsh conditions, SiC offers greater reliability in MEMS devices relative to silicon due to the lower surface reactivity. The mechanical properties of SiC compared to silicon are summarized in Table 3.

**Table 3. Mechanical properties of silicon carbide**

	Si	3C-SiC	4H-SiC	6H-SiC
<b>Young's Modulus (Gpa)</b>	130[17]	424	-	448[18]
<b>Lattice Parameter (Å)</b>	5.43[1]	4.36[1, 19]	<b>a</b> 3.08[1, 19] <b>c</b> 10.05	<b>a</b> 3.08[1, 19] <b>c</b> 15.12
<b>Density (<math>\text{g cm}^{-3}</math>)</b>	2.3[1]	3.2[1, 19]	3.2[1]	3.2[1, 19]
<b>Melting Point (<math>^{\circ}\text{C}</math>)</b>	1420[1]	2830[1]	2830[1]	2830[1]
<b>Moh's Hardness</b>	6.5	9[1]	9[1]	9[1]
<b>Bulk Modulus (<math>\text{dyn cm}^{-2}</math>)</b>	$9.78 \times 10^{10}$ [20]	$2.5 \times 10^{12}$ [15]	$2.2 \times 10^{12}$ [15]	$2.2 \times 10^{12}$ [15]
<b>Debye Temperature (K)</b>	~650 [20]	1200[19]	1300 [15]	1200 [15]
<b>Thermal Conductivity (<math>\text{W cm}^{-1}\text{C}^{-1}</math>)</b>	1.5 [1]	3.6 [15]	3.7 [15]	4.9 [15]
<b>Thermal diffusivity (<math>\text{cm}^2 \text{s}^{-1}</math>)</b>	0.9[17]	1.6 [15]	1.7 [15]	2.2 [15]
<b>Thermal Expansion (<math>10^{-6} \text{C}^{-1}</math>)</b>	2.6[1]	3.8[1]	-	$\perp$ c-axis 4.3 [15] $\parallel$ c-axis 4.7

## 2.4. Conventional Silicon Carbide Bulk Micromachining Techniques

Silicon Carbide MEMS are developmentally hindered by the hardness and chemical inertness properties of silicon carbide. These same properties have lead to the use of silicon carbide widely being used as a lapping, polishing, and machining material. Silicon carbide is only known to be etched by liquid etchants: phosphoric acid at  $215^{\circ}\text{C}$  and alkaline solution

of  $K_3Fe(CN)_6$  above  $100^\circ C$  [21]. Alternatively silicon carbide can be etched by disordering the crystal lattice during ion bombardment followed by chemical etching resulting in sub micron depth trenches after each bombardment-etch step [21]. However, it is not a practical method of etching silicon carbide. The most successful methods of fabricating structures deep enough to be viable for diaphragm fabrication are electrochemical etching and dry etching methods.

As an alternative to etching material from a bulk material silicon carbide can be deposited using a chemical vapor deposition (CVD) technique, however only thin layers of single crystalline 3C-SiC can be deposited onto Si substrates [22]. Bulk silicon carbide can also be deposited with a CVD process onto pre-fabricated Si molds, however only poly-SiC can be deposited in pre-fabricated molds and it suffers from poor mechanical and electrical properties [23]. For this reason bulk micromachining of single crystalline SiC has remained the preferred approach to achieving high performance SiC MEMS devices.

### 2.4.1. Electrochemical Etching of SiC

Electrochemical etching proceeds by generating holes in the process which breaks the SiC to  $SiO_x$  and  $CO_x$  which are then attacked by the electrolyte solutions [21].

Electrochemical etching of SiC has proven to be a successful method for SiC due to the ability to selectively etch n-type layers utilizing a p-type layer as an etch stop. The primary methods of electrochemical etching used are photoelectrochemical (PEC) and the dark chemical etching (EC). PEC etching developed by Shor at Kulite Semiconductor, is advantageous in the fast etching of shallow structures with etch rates as high as  $25 \mu m \text{ min}^{-1}$  [24] and used in applications such as piezoreistor patterning [25]. PEC was used by Okojie et

al. to pattern the piezo-resist layer for a 6H-SiC MEMS pressure sensor device [25], however PEC was later abandoned in favor of  $\text{NF}_3$  dry etching for this step [26].

Dark electrochemical etching on the other hand, has been demonstrated for etching deep structures ( $> 100 \mu\text{m}$ ) [27]. p-type 6H-SiC successfully erodes during dark EC etching [27] while n-type 6H-SiC results in the formation of porous SiC which is removed via subsequent thermal oxidization and conventional etchant solutions [28, 29]. Dark etching has also been used as a means of producing p-type 6H-SiC diaphragms [27] and functional pressure sensors [26] using an ITO mask. Chang et al. was able to fabricate a diaphragm structure  $20 \mu\text{m}$  [27] thick as shown in Figure 3 while the etch depth can be precisely controlled using etch stops. The process is limited by the ability to grow heteroepitaxial layers and the associated cost. In general the lateral selectivity of electrochemical etching is poor and suffers from filleted sidewalls as seen in Figure 2. Additionally the etch rates for obtaining a high quality diaphragm should be on the order of  $1 \mu\text{m min}^{-1}$ [30]. When using EC etching a substrate with more than 2 alternating layers, as is commonly required for a complete, the junction voltages should be carefully considered to be higher than that of the etching potential for the piezoresistor epitaxial layer to prevent it from being eroded while the diaphragm is fabricated. The reader should refer to reference: [30] for more detail on this subject.

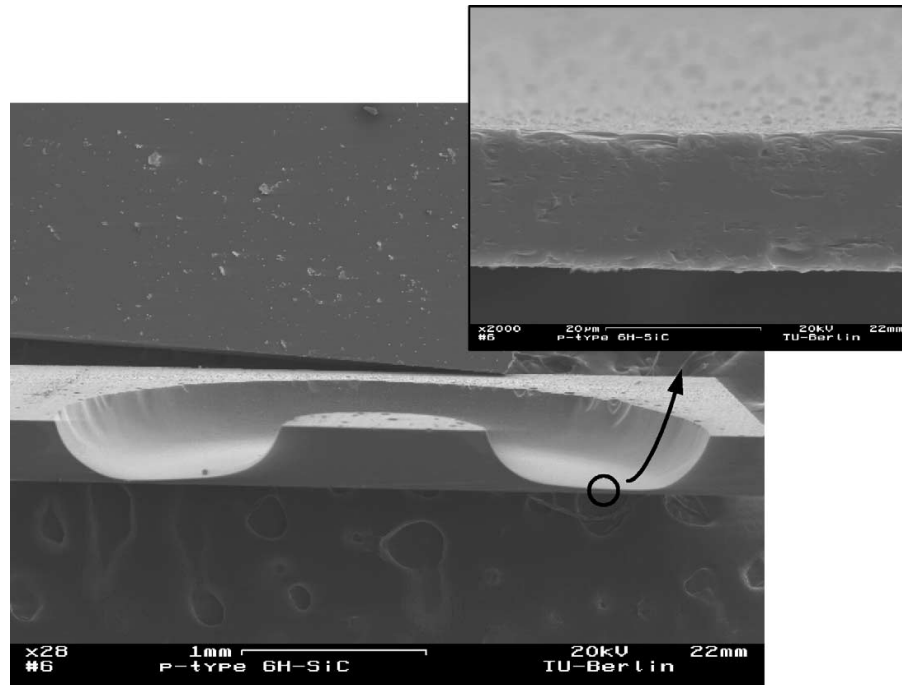


**Figure 3. 6H-SiC Diaphragm fabricated using electrochemical etching [27] (Reprinted from Sensors and Actuators A v112, 1, p.36-43 copyright 2004 with permission from Elsevier)**

#### 2.4.2. High-Density Plasma Etching of SiC

Dry etching of silicon carbide can be achieved in High-Density Plasma (HDP) etch chambers where a highly reactive plasma is generated and interacts with the substrate. Typically  $\text{SF}_6$  or  $\text{ClF}_6$  reactive gases are used for SiC. Plasma is a charged gas with equal numbers of positively and negatively charged species. The most common HDP methods are inductively coupled plasma (ICP) and electron cyclotron resonance (ECR) [23].

Electron Cyclotron Resonance (ECR) uses the injection of microwaves into a chamber to create a plasma which is controlled by magnets. ECR has been reported to have etch rates as high as  $4500 \text{ \AA min}^{-1}$  [6] on 6H-SiC, however ICP is usually used instead of ECR because of its relative simplicity and lower cost compared to ECR systems [23].

Inductively Coupled Plasma Etch (ICP) uses a chamber surrounded by a coil that uses a time varying magnetic field to generate the plasma. The ICP process operates at lower pressures and generates a higher density of ions than other methods; this minimizes scattered ions leading to straighter sidewalls, but suffers from the micromasking effect that produce grass like structures [23]. ICP etching of silicon carbide with fluorine gases is inherently anisotropic allowing deep structures to be etched. ICP using a  $\text{NF}_3$  gas was reported as having an etch rate as high as  $9,700 \text{ \AA min}^{-1}$  for etching structures on 6H-SiC [6]. A higher etch rate of  $2 \text{ \mu m min}^{-1}$  was reported for  $\text{SF}_6$  gas and ultimately the basis of the highly successful DRIE process for SiC [23]. The ICP process has been used for shallow etch steps such as the single step process for fabricating thin film resonators [6] and patterning the piezoresistive layer on the surface of a 6H-SiC MEMS diaphragm .

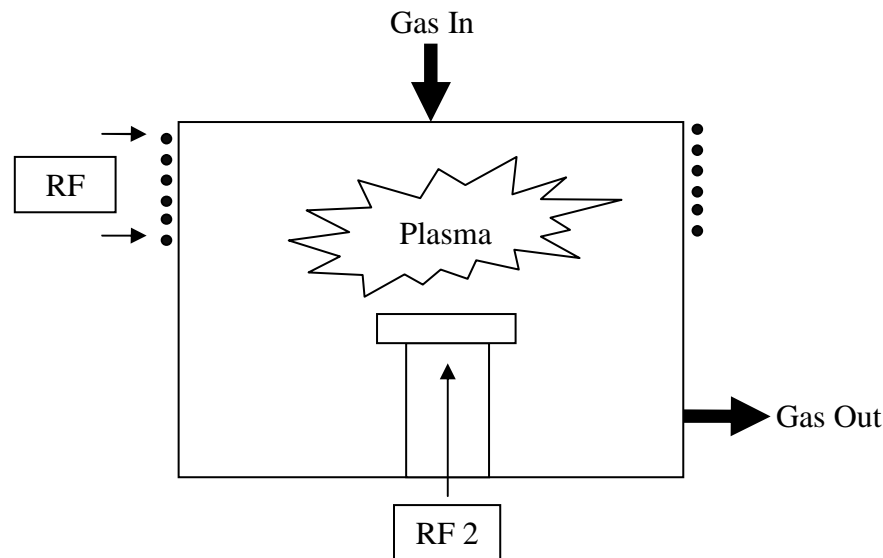


**Figure 4. Inductively coupled plasma (ICP) system schematic with two independent RF generators [23]**

ICP is the basis for the highly successful DRIE process that uses a SF<sub>6</sub> and Ar gas mixture with either a Nickel or ITO mask. The DRIE process on silicon refers to a RIE process that uses alternating isotropic plasma etch and passivation etch to prevent curved sidewalls, DRIE with just the etch step in silicon is inherently more isotropic [23]. While DRIE of SiC can obtain etch rates on the order of 2 μm min<sup>-2</sup> [2], higher quality smooth etch profiles are obtained at a rate of 0.22 μm min<sup>-1</sup> [23]. DRIE has been used by Okojie et al. to fabricate a monolithic 6H-SiC MEMS pressure sensor diaphragm with great success to fabricate high quality diaphragms that exhibit excellent surface quality machined from bulk material 245 μm deep (See Figure 5) [26]. The highly smooth surface quality that is obtainable with DRIE requires the use of Argon sputtering after ICP processing [23]. Ongoing work in the area of DRIE involves obtaining an aspect ratio greater than six [23] to make it viable for producing other MEMS devices.

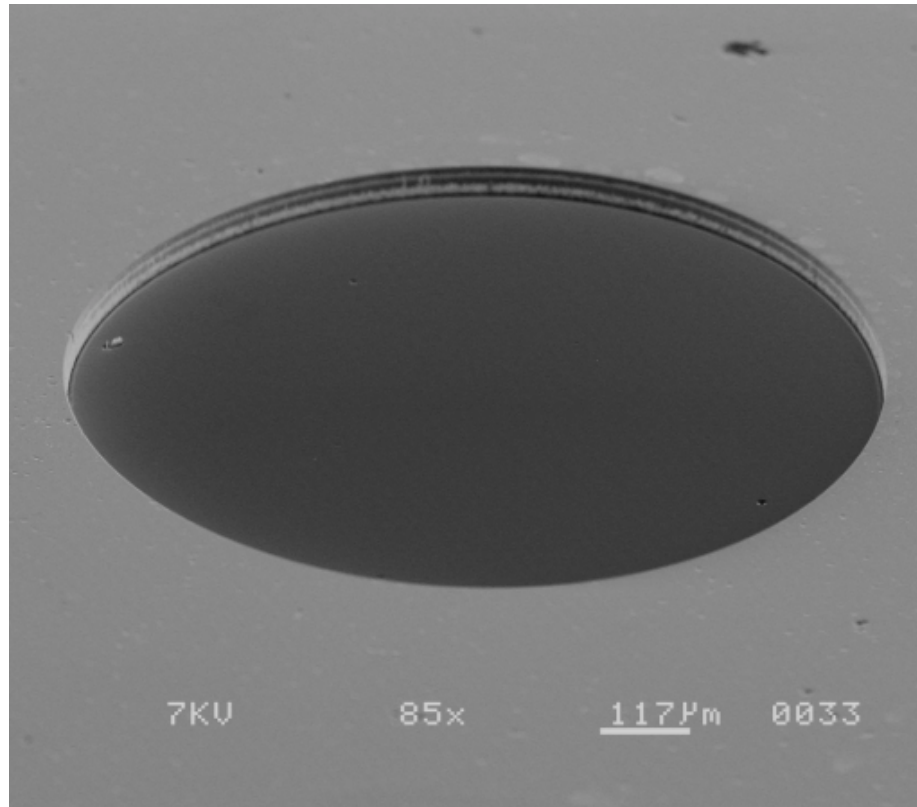


**Figure 5. Deep Reactive Ion Etch of 6H-SiC to create a diaphragm structure following an in situ Ar ion etch**

## **2.5. Silicon Carbide MEMS Pressure Sensor Fabrication**

Much progress has already been made by Okojie et al. from the NASA Glenn Research Center has already made great progress in the development of single crystalline silicon carbide MEMS pressure sensors. This work has recently resulted in a technology license to Endevco Corp. (San Juan Capistrano, CA) for commercial development [32]. The work by Okojie et al. has primarily focused on EC etching and more recently DRIE methods to fabricate the diaphragms due to its intrinsic dimensional control. Early work by Okojie et al. focused on EC etching of the diaphragm using an epitaxial layered substrates followed by a PEC etch of the epitaxial piezoresistor layers, but later work focused on DRIE methods for etching diaphragms.

## 2.6. Laser Micromachining

There are a wide variety of laser types and are usually selected for an application based on their output wavelength and the duration of the pulse (also known as pulse width). Most laser beams have a spatial Gaussian distribution of intensity across the beam cross section and a temporal Gaussian distribution of intensity through the pulse duration. By convention the pulse width is measured as the full-width half-max (FWHM) of the temporal intensity of the beam. Conventional lasers have pulse widths on the order of (<100) nanoseconds ( $10^{-9}$ ), but emerging ultra-short pulsed laser technologies include lasers with pulse widths on the order of picoseconds ( $10^{-12}$ ) and femtoseconds ( $10^{-15}$ ). In this report laser micromachining is investigated with several types of lasers: Ultra short pulse, Excimer, and Nd:YAG. In the nanosecond regime the laser has high heating effects while in the sub picosecond regime results in non-thermal ablation and less dependence upon the optical properties of the material.

### References

1. *Process Technology for Silicon Carbide*. EMIS Processing, ed. C.-M. Zetterling. 2002, London, UK: INSPEC, The Institution of Electrical Engineers. 176.
2. *The MEMS Handbook*, ed. M. Gad-el-Hak. 2002, Boca Raton, FL, USA: CRC Press.
3. *Plunkett's Nanotechnology & MEMS Industry Research Center*. 2008, Plunkett's Research Ltd.
4. Bryzek, J., *Impact of MEMS technology on society*. Sensors and Actuators A, 1996. 56: p. 1-9.

5. Park, J.-S., C. Wilson, and Y.B. Gianchandani, *Micromachined Pressure Sensors*, in *The MEMS handbook*, M. Gad-el-Hak, Editor. 2002, CRC Press: Boca Raton, FL, USA.
6. *Silicon Carbide Micro ElectroMechanical Systems for Harsh Environments*, ed. R. Cheung. 2006, London, UK: Imperial College Press.
7. Melzak, J.M., *Silicon Carbide for RF MEMS*. IEEE MTT-S International Microwave Symposium digest, 2003. **3**: p. 1629-1632.
8. Nakashima, S., K. Kisoda, and J.P. Gauthier, *Raman determination of structures of long-period SiC polytypes*. Journal of Applied Physics, 1994. **75**(10): p. 5354-5360.
9. Wu, C.H., C.A. Zorman, and M. Mehregany, *Growth of polycrystalline SiC films on SiO<sub>2</sub> and Si<sub>3</sub>N<sub>4</sub> by APCVD*. Thin Solid Films, 1999. **355-356**: p. 179-183.
10. von Berg, J., et al., *High Temperature Piezoresistive  $\beta$ -SiC-on-SOI Pressure Sensor for Combustion Engines*. Materials Science Forum, 1998. **264-268**(1101-1106).
11. Yakimova, R., et al., *Structure Evolution of 3C-SiC on Cubic and Hexagonal Substrates*. Materials Science Forum, 2006. **527-529**: p. 283-286.
12. Bechstedt, P., et al., *Polytypism and Properties of Silicon Carbide*. Physica Status Solidi (b), 1997. **202**: p. 35-62.
13. Farsari, M., et al., *Efficient femtosecond laser micromachining of bulk 3C-SiC*. Journal of Micromechanical Microengineering, 2005. **15**: p. 1786-1789.
14. Zoppel, S., et al., *Laser micro machining of 3C-SiC single crystals*. Microelectronic Engineering, 2006. **83**: p. 1400-1402.

15. *Properties of Advanced Semiconductor Materials: GaN, AlN, InN, BN, SiC, SiGe*, ed. M.E. Levinshtein, S.L. Rumyantsev, and M.S. Shur. 2001, New York, NY, USA: John Wiley & Sons, Inc. 194.
16. Mehregany, M. and C.A. Zorman, *SiC MEMS: opportunities and challenges for applications in harsh environments*. Thin Solid Films, 1999. **355-356**: p. 518-524.
17. *Semiconductor Sensors*, ed. S.M. Sze. 1994, New York, NY, USA: John Wiley & Sons, Inc.
18. Atwell, A.R., et al., *Simulation, fabrication and testing of bulk micromachined 6H-SiC high-g piezoresistive accelerometers*. Sensors and Actuators A, 2003. **104**: p. 11-18.
19. *Properties of Silicon Carbide*. EMIS Datareviews Series, ed. G.L. Harris. Vol. 13. 1995, London, UK: INSPEC, the Institution of Electrical Engineers.
20. *Properties of Crystalline Silicon Carbide*. EMIS Datareviews Series, ed. R. Hull. Vol. 20. 1999, London, UK: INSPEC, the International Society of Electrical Engineers.
21. Zhuang, D. and J.H. Edgar, *Wet etching of Gan, AlN and SiC: a review*. Materials Science and Engineering: R: Reports, 2005. **48**(1): p. 1-46.
22. Nagasawa, H. and K. Yagi, *3C-SiC Single-Crystal Films Grown on 6-Inch Si Substrates*. Physica Status Solidi (a), 1997. **202**: p. 335-358.
23. Beheim, G.M., *Deep Reactive Ion etching for Bulk Micromachining of Silicon Carbide*, in *The MEMS Handbook*, M. Gad-el-Hak, Editor. 2002, CRC Press: Boca Raton, FL, USA.
24. Shor, J.S. and A.D. Kurtz, *Dopant-selective etch stops in 6H and 3C-SiC*. Journal of Applied Physics, 1997. **81**: p. 1546-1551.

25. Okojie, R.S., et al.  *$\alpha(6H)$ -SiC Pressure Sensors at 350°C*. in *International Electron Devices Meeting*. 1996. San Francisco, CA, USA.
26. Okojie, R.S., et al., *Characteristics of a hermetic 6H-SiC Pressure Sensor at 600°C*, in *AIAA Space 2001 Conference and Exposition*. 2001: Albuquerque, NM, USA. p. 1-8.
27. Chang, W.-H., *Micromachining of p-type 6H-SiC by electrochemical etching*. *Sensors and Actuators A*, 2004. **112**: p. 36-43.
28. Chang, W.-H., et al., *Electrochemical Etching of n-type 6H-SiC Without UV Illumination*. *Journal of MicroElectroMechanical Systems*, 2006. **15**(3): p. 548-552.
29. Shor, J.S., R.M. Osgood, and A.D. Kurtz, *Photoelectrochemical conductivity selective etch stops for SiC*. *Applied Physics Letters*, 1992. **60**(8): p. 1001-1003.
30. Okojie, R.S., *Fabrication and Characterization of Single-Crystal Silicon Carbide MEMS*, in *The MEMS Handbook*, M. Gad-el-Hak, Editor. 2002, CRC Press: Boca Ranton, FL, USA.
31. Pearton, S.J., *Wet and dry etching of SiC*, in *Process technology for silicon carbide devices* C.-M. Zetterling, Editor. 2002, INSPEC: London, UK.
32. Martin, K. *NASA Technology Licensed for New MEMS Pressure Sensors*. 2008 May 2, 2008 [cited Jan 16, 2009]; Available from:  
[http://www.nasa.gov/centers/glenn/news/AF/2008/Mar08\\_Sensors\\_NR.html](http://www.nasa.gov/centers/glenn/news/AF/2008/Mar08_Sensors_NR.html).

## CHAPTER 3. A REVIEW OF LASER MICROSCALE PROCESSING OF SILICON CARBIDE

An excerpt from a paper submitted to Journal of Laser Applications (2008)

B. Pecholt, S. Gupta, and P. Molian

### 3.1. Abstract

A review of various laser techniques for microscale processing of SiC for microelectronics and MEMS applications is presented. SiC is an excellent material for harsh environments due to its outstanding mechanical, thermal, and chemical properties. However, its extreme stability and inert properties created difficulties in conventional microfabrication methods to fabricate devices and has offered an opportunity for the exploration of laser processing as an alternative. Many aspects of laser processing of SiC are investigated across the globe using wavelengths ranging from 193 to 1064 nm and pulse widths from nanoseconds to femtoseconds with results indicating that lasers can become successful tools for SiC microprocessing in the future. This paper is categorized into additive and subtractive laser techniques in order to facilitate a discussion of all processes used for fabricating microdevices.

### 3.2. Introduction

The success of microelectronics has been followed by rapid development in MicroElectroMechanical Systems (MEMS) resulting in a wide array of device applications which impact our daily life. In particular, an increased demand for devices capable of functioning at high temperatures and in harsh environments accounts for the emergence of Silicon Carbide (SiC) as a preferred material. The continued interest of SiC is primarily due

to advancements in deposition and crystalline growth techniques and its ability to be used at high temperature in highly erosive or corrosive environments [1-4]. Many areas of industry would benefit from implementation of SiC MEMS sensors including: oil drilling, avionics and spacecraft systems, and engine, turbine, and industrial process control. SiC has already been used for high temperature pressure sensors[5-12], accelerometers[13], micromotors[14, 15], and CMOS compatible devices[6]. SiC is also of interest for high power electronics and RF and microwave applications[16, 17]. Some of the more notable properties of SiC are the high saturation drift velocity, high bandgap, high thermal stability, high thermal conductivity, low diffusion rates, and chemical inertness. Unfortunately some of these properties are also barriers to the fabrication of microelectronics and MEMS devices. Major challenges that still exist in include: dielectric deposition, etching, oxidation, metallization, and doping. Laser processing has been explored in these areas as both additive (annealing, deposition, surface alteration, and doping) and subtractive (ablation) processes. Here we provide a review of SiC laser processing relevant to these areas with the expectation that continued development will lead to a proliferation of SiC devices.

### **3.3. Overview of SiC Laser Processing**

Laser micromachining has several advantages over conventional microfabrication techniques due to its minimization of processing steps, its ability to be used as a CNC prototype tool, and scalability through serial or batch processing. Lasers have been explored as tools for SiC processing since the early 1980s, but yet to achieve widespread use for microelectronics and MEMS applications. Virtually every laser applicable to

microfabrication has been explored: traditional excimer, Nd:YAG, and CO<sub>2</sub> [18-20], the more novel lasers such as the N<sub>2</sub> [21], Ar<sup>+</sup> [22], Cu Vapor [23, 24] and the emergent picoseconds [25] and femtosecond lasers [26-33]. Table 4 summarizes the laser types and their applications for SiC processing. Nanosecond pulsed UV lasers such as excimer and frequency tripled and quadrupled Nd:YAG are most widely used [20, 26, 34-38] due to their prevalence and the high optical absorption of crystalline SiC at UV wavelengths single crystalline SiC is practically transparent at visible wavelengths, but has an optical absorption on the order of 10<sup>-5</sup> cm<sup>-1</sup> in the UV regime due to the higher-than-band gap photon energy. On the contrary, polycrystalline and amorphous SiC, can absorb light in the visible and near IR spectra; this is a necessary condition for the success of lasers to ablate amorphous SiC [22, 33, 39, 40] and poly-SiC [18-20]. IR pulses have also been explored for single crystalline 4H-SiC where the ability to machine is a result of photons directly interacting with the lattice rather than through electrons [20, 41-43]. Lasers with ultrashort pulse widths ( $\tau_p < 1$  picosecond) have been gaining interest in the laser micromachining community due to their ability to machine virtually any material including high bandgap dielectrics irrespective of the laser wavelength. Ultrashort laser processing of SiC has been shown to machine with high precision due to their pulses being faster than heat dissipation [26]. The occurrence of nanostructures on the surface of SiC is a unique phenomena to femtosecond lasers which is stimulating researchers to pursue further studies. It's well known that laser micromachining can be quite complicated by collateral thermal effects such as melt, recast, and heat affected zone (HAZ) and these effects are accentuated for nanosecond pulsed lasers. Thermal heating also plays an important role for annealing, doping, and non-congruent ablation processes. In general, semiconductor light absorption is dominated by photon-induced electron transitions from the

valence to the conduction band by forming electron-hole pairs, and excess kinetic energy is transferred to the lattice as phonons within picoseconds resulting in heating[26]. Therefore, it is of interest to discuss the success of the heat dissipation studies from the literature [46, 60-63] where researchers have focused primarily on the use of pulsed excimer lasers for annealing. As a rule of thumb the heat flow into the material is determined by the thermal penetration length,  $L_e$ , which is defined by Equation 1. From this it is evident that the thermal penetration length of nanosecond lasers should be orders of magnitude higher than that of the femto, and even picoseconds lasers.

#### Equation 1

$$L_e = 2\sqrt{D\tau_p}$$

Where

$D$ : Material Thermal Diffusivity

$\tau_p$ : Laser Pulse Width

Detailed modeling has been employed using a modified heat diffusion equation (Equation 2) and the Beer-Lambert equation (Equation 3).

#### Equation 2

$$\frac{\partial T}{\partial t} = \frac{\alpha}{\rho C_p} I(z, t) + \frac{1}{\rho C_p} \frac{\partial}{\partial z} \left( \kappa \frac{\partial T}{\partial z} \right)$$

#### Equation 3

$$I(z, t) = I_o(t)(1 - R)\exp(-\alpha z)$$

**Table 4. Laser processing applications for silicon carbide**

Application	Laser	$\lambda$ (nm)	Material	Comment
Annealing	Excimer	193, 248, 308	Ion implanted damage zones (amorphous)	Ion implanted zones recover from amorphous to polycrystalline up to 500 nm deep [33, 44-51]
	Nd:YAG	355 nm	Amorphous film on dielectric	direct write of a-SiC converted to poly-SiC ~50nm, thick [39]
	Argon (CW)	514.5 nm	Amorphous film	Direct write of recrystallized zones of a-SiC to poly-SiC [22, 40]
Via Hole Drilling	CO <sub>2</sub> 30ns Q-switched	10.6 $\mu$ m	4H-SiC	High ablation rate 0.47-1.8 $\mu$ m pulse <sup>-1</sup> [41, 42, 52]
	Excimer	248	4H-SiC	Ablation rate ~0.23 $\mu$ m pulse <sup>-1</sup> [53]
	Ti:Sapphire (femtosecond pulses)	800	4H-SiC	Ablation rate ~0.25 $\mu$ m pulse <sup>-1</sup> [54]
<i>In situ</i> doping	Nd:YAG	1064	4H-SiC, 6H-SiC	n-type (nitrogen) doping 600 nm deep junction p-type (Al <sup>+</sup> ) doping 4.3 $\mu$ m deep junction [55]
	Excimer	193	4H-SiC, 6H-SiC	n-type (nitrogen) doping 50 nm deep junction p-type (Al <sup>+</sup> ) doping 150 nm deep junction
Electroless Metallization	Excimer	193, 308	Single Crystal (Hexagonal)	Catalytic sites of Si nanoclusters and thermal stress facilitates electroless [56, 57]
	Cu-Vapor	510		Cu and Ni contacts [23, 24]
Nanostructuring	Ti:Sapphire (femtosecond pulses)	800	3C-SiC, 4H-SiC, 6H-SiC	Circular Polarization: Spherical Nanoparticles [28-31, 54, 58, 59] Linear Polarization: Nanoripples

Where

$T$ : Absolute Temperature

$t$ : Time

$\rho$ : Density

$C_p$ : Specific Heat

$\kappa$ : Thermal Conductivity

$I_o$ : Laser Intensity at the Surface

$R$ : Surface Reflectivity

$\alpha$ : Optical Absorption

$z$ : Depth below Surface

$I(z,t)$ : Laser intensity at a depth  $z$  below the surface

Equation 2 and Equation 3 are commonly used for pulsed excimer laser annealing [34, 35, 47, 63], but have also been used to model heating during dopant incorporation [55]. UV lasers are useful for annealing SiC surfaces disordered by ion implantation because the optical absorption of amorphous SiC and crystalline SiC are on the same order of magnitude which Table 5 summarizes the optical absorption of crystalline and amorphous SiC for the excimer laser family.

**Table 5. Optical absorption for excimer lasers**

	ArF		KrF		XeCl		
	Crystalline	Amorphous	Crystalline	Amorphous	Crystalline	Amorphous	
Reflectivity (R%)	40	34.6	28.6	33.6	24.3	32.4	[63]
optical absorption (cm <sup>-1</sup> )	1.50 x 10 <sup>6</sup>	1.10 x 10 <sup>6</sup>	1.40 x 10 <sup>5</sup>	8.70 x 10 <sup>5</sup>	4.50 x 10 <sup>4</sup>	6.00 x 10 <sup>5</sup>	[63]

The laser irradiation model and heating has been used to optimize laser parameters that reach the melting temperature of 4H-SiC and 6H-SiC[63] substrates for annealing where the occurrence of melting is verified through *in situ* reflectivity measurements[46]. Reitano and Baeri were able to predict the thermal evaporation of a 6H-SiC target for pulsed laser deposition (PLD) over the fluence range 0.4 to 1.6 J cm<sup>-2</sup> [34]. However, beyond 1.6 J cm<sup>-2</sup> the material was removed at a higher rate than predicted by the model suggesting molten material ejection from the surface [34, 35].

SiC undergoes non-congruent sublimation during thermal processing and laser heating results in an array of seemingly contradictory results such as oxidized [23, 24, 56, 57], carbon-rich (C-rich) or silicon-rich (Si-rich) surfaces [64]. Meanwhile, PLD of SiC films under high vacuum conditions exhibited excellent stoichiometry [65]. Some researchers [20, 66] reported that SiC begins to sublimate at temperatures between 1800°C and 2000°C yet does not melt until 2700°C. Still many others cited the occurrence of non-congruent sublimation at temperatures as low as 1000°C in bulk heating [67-71]. The non-congruent sublimation during bulk heating in vacuum proceeds with the breaking of Si-C bonds at approximately 1000°C and thermodynamically re-arrange on the surface where near surface Si quickly begins to sublimate leaving behind a carbon-rich layer [67, 69-71]. The remains of the carbon-rich layer reduce the subsequent sublimation of Si with a diffusion-limited process [71]. The primary vapor constituents of thermally decomposed SiC are Si, SiC<sub>2</sub>, and Si<sub>2</sub>C where an overall decrease in the Si to C ratio occurs in the vapor at higher temperature [72].

While the thermal decomposition of SiC in bulk heating has been well studied, there is no analogous, singular study reporting on the decomposition due to laser irradiation [64]. It has

been shown that non-congruent sublimation is also associated with laser ablation except that, in the case of the laser as a heating source, the optical properties of SiC play an important role in selecting the constituent removed from the surface [23, 73]. As a general rule excimer lasers produce Si-rich regions while IR Nd:YAG lasers seem to produce C-rich regions. Table 6 shows an overview of various laser processing conditions and their effects on the surface characteristics. Pehrsson and Kaplan[66] found that multiple pulses from an ArF laser over the range of 0.4 – 0.6 J cm<sup>-2</sup> resulted in a rise in carbon on the surface, but beyond this range resulted in a Si-rich region.

**Table 6. Surface enrichment and modification of SiC**

SiC	Laser	$\lambda$ (nm)	Pulse Width	Atmosphere	Laser Energy (J cm <sup>-2</sup> )	Effect
3C-SiC	ArF	193	14 ns	8 x 10 <sup>-10</sup> Torr	<0.400 0.400-0.600 >0.600 2.000	No change A rise carbidic then graphite surface as the number of pulses increases Si-rich surface 200nm thick Si region covering an underlying C-rich region
6H-SiC	Nd:YAG (with VUV-Raman Cell)	VUV-266	8 ns	1 x 10 <sup>-4</sup> Torr	1.06	Ablation: Graphitic Surface on Base
Hexagonal	ArF, XeCl	193, 308	30 ns	Air	1-3,5	Si-rich covered with SiO <sub>2</sub>
Hexagonal	Cu-Vapor	514	15 ns	Air, Water, or 1x10 <sup>-1</sup> Torr	10-20	Si-rich surface
6H-SiC	Nd:YAG	1064	-	Argon (30 psi)	6.65	C-rich (back side of wafer)
95% relative density SiC	KrF	248	30 ns	Air	1.8	Disorderd region with oxidized surface

They hypothesized that excimer laser pulses tend to generate a graphite layer and its subsequent removal as the energy is trapped in this layer would reveal the underlying silicon[66]. On the contrary, the Nd:YAG laser with its photon energy below the band gap results in a poor coupling with the material and mostly thermal effects causing evaporation of silicon [23, 73]. This has been explained as the reason why Nd:YAG lasers at 1064 and 532

nm result in C-rich surfaces [23, 73]. A notable exception to this hypothesis is the formation of graphite surfaces when ablating 6H-SiC using a vacuum UV Raman cell with a frequency-quadrupled Nd:YAG laser (VUV-266 nm) [37]. As expected, oxide formation is associated with the processing of SiC in the presence of oxygen [75]. For example the excimer ablation of SiC on the range of 1-3.5 J cm<sup>-2</sup> in the presence of oxygen leads to the formation of a surface oxides and an underlying Si-rich layer[57] where only the enrichment of Si was reported under high vacuum conditions [33].

### 3.4. Additive Laser Processing

Additive laser processing for SiC microelectronics and MEMS research is being driven by the challenges in traditional processing of SiC such as doping, annealing, and deposition on insulating substrates. Additive laser processing, as defined here, involves the addition of material or to meet a specific functionality of the surface through laser processing. This includes traditional techniques namely, laser annealing, pulsed laser deposition, and *in situ* laser doping, but also includes techniques unique to SiC such as metallization, electroless metal deposition, and nanoparticle formation.

#### 3.4.1. Doping and Annealing of Silicon Carbide

Carriers are introduced into SiC using group III and V elements to form the respective p-type and n-type conducting materials. The most commonly investigated elements are boron and aluminum as acceptors and nitrogen and phosphorus as donors [76]. Conventional diffusion process for SiC remains impractical because temperatures greater than 2000°C are required [76]. Ion implantation results in a disordered surface requiring thermal annealing to partially recover the crystal at temperatures as high as 1100°C [77] and activation of

impurities requires temperatures in excess of 1500°C [39]. These elevated temperatures are problematic due to both the thermal damage incurred on the SiC and the fact that conventional furnaces used in the semiconductor industry are typically limited to 1300°C [76]. Other alternatives such as impurity introduction during epitaxial growth have been explored, however, this limits the development of devices.

### **3.4.1.1. In situ laser doping of Silicon Carbide**

*In situ* laser doping has been explored as an alternative to these conventional processes; principally nitrogen and aluminum have been the most investigated dopants. Laser doping exhibits high diffusion rates, orders of magnitude over conventional thermal diffusion methods[64] as summarized in Table 7. Functional devices and structures such as Schottky diodes, Ohmic contacts

[73], p-n junctions, and LEDs[78, 79] have been demonstrated. Metallized contacts also exhibited an increase of 40% reflectivity suggesting it may be useful for optics and optoelectronic applications[61].

**Table 7. Diffusion coefficients**

Process	Material	Doping Constituent	Diffusion Coefficient (cm <sup>2</sup> s <sup>-1</sup> )		Temperature	Laser		
			Fast Branch	Slow Branch		Type	Wavelength	
In Situ laser doping	6H-SiC	Nitrogen	2.4 X 10 <sup>-5</sup>	9.26 x 10 <sup>-6</sup>	-	Nd:YAG	1064 nm	[60]
	4H-SiC	Al	1.2 x 10 <sup>-5</sup>	1.3 x 10 <sup>-6</sup>	-	KrF	248 nm	
Thermal Diffusion	6H-SiC	Nitrogen	-	5 x 10 <sup>-12</sup>	1800-2450°C	-	-	[76]
	6H-SiC	Al	-	3 x 10 <sup>-14</sup> - 6 x 10 <sup>-12</sup>	1800-2300°C	-	-	

Three major categories of laser doping are: laser thermal processing (LTP), gas immersion laser doping (GILD), and laser-induced solid phase doping (LISPD). LTP involves a shallow ion implantation followed by laser heating to distribute and activate the carriers. GILD involves the use of a gaseous precursor which is thermally decomposed by the beam and incorporated into the molten surface as an impurity. LISPD is a category of laser doping whereby the substrate is heated under the beam but does not achieve the melt. It can be carried out with either a dopant film or gaseous precursor similar to that used for GILD. Solid-state diffusion is aided by the deliberate formation of vacancies that facilitate the diffusion of impurities through the material, known as effusion-diffusion.

Trimethylaluminum ((CH<sub>3</sub>)<sub>3</sub>Al) (TMA) was used for introduction of aluminum with LTP and GILD methods and N<sub>2</sub> gas for doping nitrogen. The principal lasers investigated for *in situ* laser doping are Nd:YAG lasers operating at 1064 nm and pulsed excimer lasers. Nd:YAG and excimer lasers act as bulk heating and surface heating tools respectively. As a result Nd:YAG lasers have been shown to generate much deeper dopant profiles for both aluminum and nitrogen [55].

### 3.4.1.2. Annealing of Silicon Carbide

Annealing of amorphous and poly-crystalline SiC is of interest for recovering surfaces damaged by ion implantation and specifically for MEMS applications where annealing amorphous SiC layers can achieve epitaxial and insulating layers [17]. In comparison to bulk thermal annealing, laser annealing has the advantage of being highly selective and rapid heating to reduce the thermal effects of non-congruent sublimation. Epitaxial growth reactors have been used for doping, however, ion implantation has been shown to be successful [76]. There has been controversy regarding whether laser-induced recrystallization takes place through solid [45-47] or liquid phase recrystallization [33, 39, 44, 46-48, 80]. For example independent findings by Hishida *et al.*[45] and Ahmed *et al.*[48] revealed opposition effects with the same laser. Both groups used XeCl lasers to anneal Al<sup>+</sup> ion-implanted 6H-SiC, however, Hishida reported solid-phase recrystallization [45] while Ahmed [48] reported liquid phase recrystallization. Both researchers used laser energy densities well above the melting threshold of XeCl lasers for both crystalline and amorphous SiC [63]. Hishida also reported a percentage of dopant activation over 4 orders of magnitude lower than that of Ahmed. Solid-phase recrystallization has been reported for conventional thermal annealing of ion-implanted 6H-SiC at 940°C proceeding with epitaxial regrowth [81]. However there is no such phenomenon in laser annealing where solid phase recrystallization proceeds after either a single pulse just below the melt threshold or multiple pulses well below the melt threshold [45]. It is still uncertain that epitaxial solid-phase recrystallization is possible. Hishida *et al.* suggested that the recrystallization may be seeded by nucleation sites of un-damaged crystal structure if the surface is not completely amorphitized by the ion-implantation [45]. In contrast melt-phase annealing has been shown

to be seeded by the underlying SiC crystal [44, 48], but the ability to fully recover the crystal through annealing has been disputed due to the poly-crystalline nature of the annealed surfaces [47]. The presence of melt phase during laser irradiation has been experimentally verified using *in situ* reflectivity measurements [46, 48] and is supported by the uniform impurity profile which cannot be explained by diffusion models [44, 48]. Melt phase can be achieved within a single shot, however the depth of the melt zone is affected by the heat diffusion characteristics of the material as discussed in Section 1.4. Polycrystalline layers exhibit higher resistance to melting and heat damage compared to the underlying amorphous layer, thus a multi-pulse approach where the energy is increased can lead to greater amount of recovery [39]. For example a comparison between Ahmed *et al.* [48] who used a single pulse energy to achieve recrystallization layer (75 nm thick) versus Boutupoulos *et al.* who used the multi-pulse method to achieve a recovered layer 240-280 nm thick [39].

Crystallization of CVD amorphous SiC films has been achieved for insulating layers such as SiO<sub>2</sub> and high-temperature glass [22, 33, 40, 82]. Visible lasers have been used for this purpose due to the high optical absorption of amorphous SiC [22, 46, 82]. Also novel, combined UV-IR lasers have been used for this type of work [51].

### 3.4.2 Metallization of SiC Substrates

Perhaps one of the more intriguing phenomena in laser processing of SiC is the formation of metal-like surfaces through non-congruent ablation. Contacts are formed by laser heating via the formation of either C-rich or Si-rich depending upon the processing conditions [57, 64, 73] and have been shown to demonstrate ohmic properties [23, 64, 73].

Formation of C-rich contacts can be achieved through the use of frequency-doubled Nd:YAG

lasers and Si-rich contacts through the use of pulsed excimer lasers [73]. The mostly thermal nature of the Nd:YAG lasers with its photon energy below the band gap leads to thermal evaporation of Si and excimer lasers result in the selective ablation of carbon [23, 64, 73]. Salama et al. reported the formation of ohmic contacts with resistance over the range of 0.04-0.12  $\Omega$ -cm for both 4H-SiC and 6H-SiC substrates [73]. Regions ablate by pulsed excimer lasers have also been shown to facilitate the deposition of electroless Cu and Ni metals [23, 24, 56, 57]. Laser ablation causes the formation of two different catalytic centers that facilitate the deposition of metals from electroless solutions:

Si nano-clusters and bending of conduction band from mechanical stresses [23].

These catalytic sites remain stable over a long period of time and the metallization layers can be stripped and deposited repeatedly [56].

### 3.4.3. Pulsed Laser Deposition of Silicon Carbide Thin Films

An array of conventional growth techniques for single crystalline SiC are available such as Chemical Vapor Deposition (CVD), Carbonization [83], Molecular Beam Epitaxy (MBE) [84] and photo, plasma or laser CVD [85] but these methods suffer from poor film quality due to contamination with hydrogen compounds caused by high substrate temperature in the process. Pulsed Laser Deposition (PLD) is an alternative technique with advantages such as low substrate temperature, high deposition rate, and relative ease of producing stoichiometric films [65]. Processing conditions for PLD films are summarized in Table 8. 3C-SiC films have been deposited on Si at lower substrate temperature [77, 86-90]. Interestingly Soto et al. found for SiC films deposited under argon environment exhibited better stoichiometry than those grown under nitrogen or even vacuum conditions [91]. The PLD

films are greatly affected by the surface preparation and the processing conditions[92, 93]. High-quality epitaxial films were dependent on type of substrate used ( $\alpha$ -SiC or  $\beta$ -SiC), substrate temperature, laser parameters such as photon energy, frequency, wavelength and pulse width. Films exhibiting crystallinity were observed when substrate temperature was between 700°C[86] and 800°C [89, 94]. All films deposited between 400 and 800°C are extremely smooth with roughness on the order of  $0.40 \pm 0.2$  nm. Roughness increases substantially with temperature. Roughness of  $4.70 \pm 0.8$  nm for the film deposited at 950°C was attributed to the formation of large crystallites [77]. Annealing following deposition has also been reported to facilitate the conversion from polycrystalline to single crystalline films [89, 90, 94]. Conversion of amorphous to 3C-SiC films occurs at 980°C [95] while conversion to 4H-SiC occurs in the range of 1100°C to 1400°C [94].

**Table 8. Pulsed laser deposited parameters**

Deposited Film	Laser	$\lambda$ (nm)	$\tau$	Repetition Rate (Hz)	Pulse Energy (mJ)	Energy Density ( $J\ cm^{-2}$ )	Substrate Temperature	Annealing Temperature	
4H-SiC	XeCl	308	25 ns	-	-	-	850°C	1100°C - 1400°C	[94]
3C-SiC	ArF	193	17 ns	3	150-200	-	800°C	980°C	[95]
6H-SiC	Nd:YAG	266	ns, ps	-	-	-	1100°C - 1200°C	-	[93]
3C-SiC	KrF	248	25 ns	5, 10	-	2.5	700°C	-	[96]
-	KrF	248	25 ns	100	-	5	250°C	-	[97]
-	KrF	248		5-10	500	-	500°C	-	[92]
3C-SiC	XeCl	308	20 ns	1	520	-	800°C	-	[86]
3C-SiC	KrF	248	20 ns	10	-	3.2	400-950°C	1100°C	[98]
3C-SiC	KrF	248	20 ns	10	-	5	370°C	800° - 1200°C	[99]
3C-SiC	Ti:Sapphire	800	50 fs	$1 \times 10^3$	-	0.100-0.300	500-800°C	-	[87]

### 3.4.4. Nanoparticle formation

Nanostructured surfaces are useful for applications in quantum electronics, optoelectronics, tribiology, and NEMS. Laser-induced nanostructures on 6H-SiC were demonstrated to have decreased reflectivity and increased optical absorption by as much as 39% [100]. *In situ* formation of nanoripples under laser irradiation was first reported on the surface of germanium using a ruby laser [101]. More recently femtosecond lasers have been reported to form spherical nanoparticles and periodic nanoripples on a variety of dielectrics and semiconductor materials with feature size from  $\lambda/3$ -  $\lambda/10$  where  $\lambda$  is the wavelength [102-109].

Nanostructure formation occurs at low energy fluences well below that required for inducing melt and ablation. Spherical nanoparticles form under circularly polarized beams while nanoripples are associated with linearly polarized beams. The nanoripples are oriented perpendicular to the electric field of the laser beam [102, 105, 108, 110]. Similar results were also reported for crystalline SiC [28, 29, 58, 59, 100, 111]. There is still controversy over the exact mechanism that causes the formation of nanoripples but it has been attributed to phenomena such as Coulomb explosion [28, 29], self assembly [106, 107], and laser beam interference with the plasma [103].

The majority of the work carried out in femtosecond laser-induced formation of nanoparticle has been the irradiation of small regions of the surface with multiple pulses. The high peak power of the femtosecond laser and Gaussian profile of beam lead to a large energy fluence distribution across the beam. Nanoparticles have been found to form within discrete regions associated with the varying energy density resulting in concentrically aligned regions of nanoparticles [29, 58, 59]. Dong and Molian determined threshold regimes for

three distinct nano-structured zones under a circularly polarized beam. The structure regions are: a transition zone, a ripple zone with ripples parallel to the electric field, and a center zone caused by heat, melt, and recast [27, 29]. Similarly, Tomita *et al.* also observed regions associated with the energy density of the beam on 4H-SiC using a linearly polarized beam with more pronounced nanoripples [58]. The formed nanoripples were oriented parallel to the electric field of the beam only at the center, and the peripheral zones formed perpendicular to it [58]. In the interest of developing surfaces useful for device applications, long range coverage of surfaces with nanostructures have also been explored with linearly polarized beams [112] and circularly polarized beams [31] to create a long range array of nanostructures in the beam tracks. Juodkazis et al. established a region greater than 10 x 10 mm region of nanoripples by raster scanning a beam [112]. Spherical nanoparticle formation in the beam tracks were reported with a track width of several microns over a length of tens of microns [31]

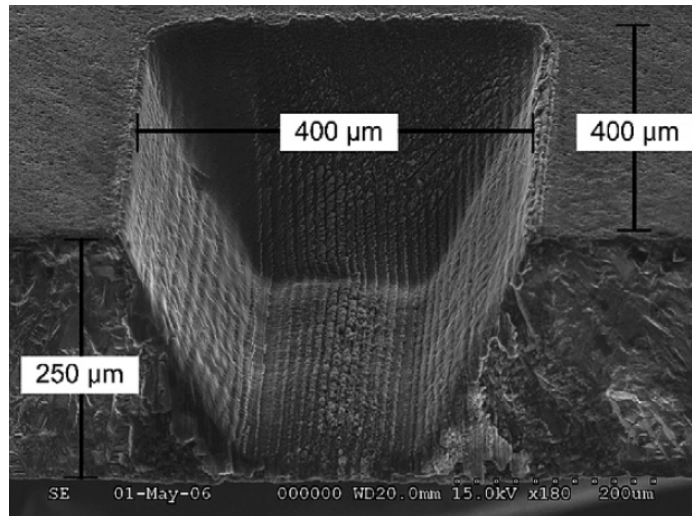
### 3.5. Subtractive Laser Processing

Material removal of SiC through laser ablation has been investigated extensively on all polytypes – single, polycrystalline, and amorphous - SiC. Conventional MEMS and microfabrication techniques involve the use of masking, wet etching of specific crystal orientations or dry etching using reactive ion etching. However, the chemical inertness and hardness of SiC slow down wet etching and dry etching methods although DRIE has enjoyed the most success as subtractive micromachining process for SiC with etch rates of  $2 \mu\text{m min}^{-1}$  [113]. The interest in etching SiC has also inspired the exploration of more novel processing

methods such as PhotoElectroChemical (PEC) etching which has achieved etch rates of  $25 \mu\text{m min}^{-1}$  [114].

In contrast laser ablation of SiC is capable of high etch rates on the order of hundreds of microns per second [41, 42, 52], reduces the number of processing steps by avoiding the need for masking, machining is independent of crystal structure, and curved surfaces are possible. However, laser micromachining of structures on SiC has principally been limited to via hole formation[26, 32, 41, 42, 52, 115]. Only a few MEMS structures have been laser micromachined. Laser ablation for micromachining of SiC is certainly a promising area of microfabrication. Not only can lasers achieve etch rates on the order of hundreds of  $\mu\text{m min}^{-1}$ , but material removal of SiC through laser ablation has been demonstrated to be consistent over tens to hundreds of pulses[41, 114, 115] for UV, IR, and femtosecond lasers with few special exceptions[114]. Ablation rates are summarized in Table 9.

**Figure 6. ArF laser micromachined trench on amorphous SiC [116]. (Reprinted from Sensors and Actuators A v136, 2, p.554-563 copyright 2007 with permission from Elsevier)**



Laser ablation of the crystalline SiC polytypes is principally investigated using UV-lasers[26, 36, 115, 117] due to the high optical absorption. Similar behavior was noted in amorphous SiC[63]. Using an excimer laser, Desbiens and Masson were able to machine deep structures up to 200  $\mu\text{m}$  in amorphous SiC wafers[116]. They determined that machining conditions were optimized for low energy and high repetition rates with high scan speeds [116]. Thin diaphragm structures as seen in Figure 6 were machined using fluence of  $5 \text{ J cm}^{-2}$ , repetition rate of 100 Hz, and scan speed of  $170 \mu\text{m s}^{-1}$  [116].

**Table 9. Laser ablation rates**

Material	Wavelength (nm)	Pulse Width	Fluence ( $\text{J cm}^{-2}$ )	Ablation Rate (nm/pulse)	Repetition Rate (Hz)	Temporal Ablation Rate ( $\mu\text{m}/\text{min}$ )	Atmosphere			
3C-SiC	248	14	ns	2	40	100	240*	8.00E-10	Torr	[66]
	248	34	ns	8	100	100	600*	Air		[26]
	193	25	ns	8	100*	100	600*			
	1026	400	fs	1.2	60*	-	-			
	1040	300	fs	10.60	-	-	600-900			
-	<200	fs	105-180	-	50,000	33000-15600	-		[32]	
4H-SiC	1060	30	ns	-	470-1800*	8	229-870	N <sub>2</sub> Flow		[41, 42, 52]
	248	30	ns	-	230	100	1380*	Air		[53]
	800	120	fs	20	250	-	-	Air		[54]
	355, 532, 1064	-	-	-	-	$60 \times 10^3$	3000	Air		[118]
	355, 532, 1064	30	ns	-	-	8	120-840	-		[119]
6H-SiC	266	8	ns	1.06	35	1	2.10	1.00E-04	Torr	[36-38]
	308	15	ns	2.20	60	100	360*	1.00E-06	Torr	[34, 35]
a-SiC	193	5	ns	-	200*	100	1200*	Air		[116]

\* Interpolation of reported data

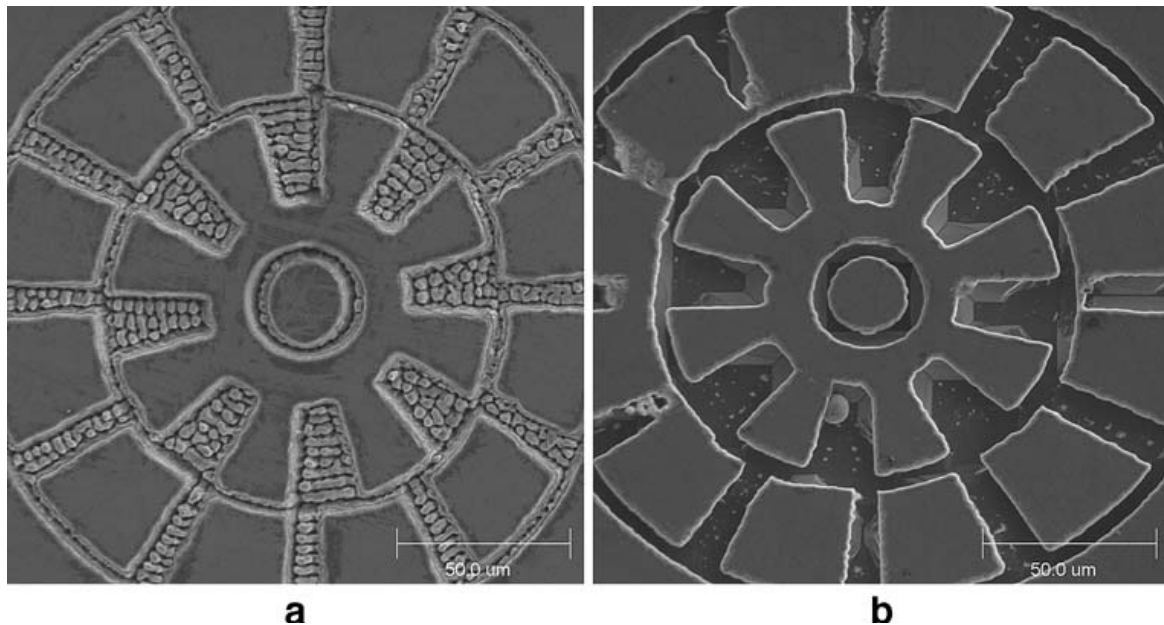
Excimer lasers are advantageous because of their large beam size and uniform energy distribution and ability to be used with masking operations, however there has yet to be a SiC structure formed using masking techniques. Despite the poor optical absorption of single crystalline SiC, visible[23] and IR[20] photons are capable of coupling directly with the

lattice and generating absorbing species resulting in high etch rates. Kim, Pearton, and co-workers reported high etch rates  $229\text{-}870\ \mu\text{m min}^{-1}$  on single crystalline 4H-SiC using a  $10.6\ \mu\text{m}$  laser with repetition rate of 10 Hz for drilling via holes[41, 42, 52]. Similarly, high etch rates were reported for a Nd:YVO<sub>4</sub> laser at wavelengths 355, 532, 1064 nm and 30 ns pulse widths, however the lower wavelengths produced better sidewalls, and the lowest amounts of debris[118, 119]. In contrast to single crystals, amorphous and polycrystalline SiC enjoys more machining versatility with these lasers due to the high optical absorption in this regime. This has allowed for highly selective control of the depth and thereby enable the machining of complex 3D structures aided by the use of high repetition rates[24, 75]. Krutz *et al.* used Q-switched Nd:YAG ( $\lambda = 1064\ \text{nm}$   $\tau_p = 10\ \text{ns}$ ) to machine complex 3D structures in poly-SiC stock material such as 3D semi-spherical depression and thread structures[75]. Surface quality was optimized when using a fluence less than  $15\ \text{J cm}^{-2}$  and scan speeds less than  $10\ \text{mm s}^{-1}$  [75].

Femtosecond pulses have been shown to have excellent machining properties because of their ultrafast interaction times resulting in low thermal diffusion, and their multi-photon absorption which negates the requirement for matching a specific laser wavelength to a material. Femtosecond lasers have been have produced low HAZ and fast etch rates in via hole formation[26, 31, 32], 3C-SiC thin film scribing[31] and 4H-SiC bulk material removal[54]. Dong and Molian reported high quality femtosecond laser micromachining of single crystalline 3C-SiC[27, 29-31]. Pulse energy ranging from (1-10  $\mu\text{J}$ ) was found to be optimal for producing high resolution, damage free features. In this range, high quality 3C-SiC micro-rotors were patterned[31]. Figure 7 shows SEM micrographs of the micro-rotor before and after KOH release. It was found that as the energy increases ( $>20\ \mu\text{J}$ ) more

damage was done to the structure. Lower pulse energy produces a well defined profile with little contamination and minimal thermal damages as shown in Figure 2. Similarly diaphragm structures as deep as 100  $\mu\text{m}$  were formed on 4H-SiC by trepanning the beam with respect to the substrate[54]. Femtosecond lasers are not immune to thermal effects. For pulse energies greater than 50  $\mu\text{J}$  significant amount of recast layer and damaged fragments[31] were observed are attributed to the formation of plasma. However, high repetition (50 MHz) rates have been shown by Farsari et al. to have little impact on the thermal saturation of 3C-SiC.

**Figure 7. Femtosecond laser micromachined rotor in 3C-SiC thin films deposited on silicon before and after partial release from substrate [31]**



### 3.6. Conclusion

Due to its outstanding properties, SiC is highly desirable for microelectronics and MEMS applications in harsh and hostile environments. However, the development of these devices are limited by the inability to use conventional microfabrication techniques. Laser

microprocessing of silicon carbide has been explored for both additive and subtractive processes. Effective laser processing has been demonstrated in numerous areas of SiC microfabrication as a flexible means of processing. With fewer steps and is capable of parallel processing. Nanosecond lasers in the UV regime have been investigated more widely in the literature with some indication that the IR-spectrum could be used for appropriate applications such as via hole drilling and contact formation. Femtosecond lasers have yet to enjoy the same widespread commercial success as of the nanosecond lasers, but have been successfully shown to produce precision SiC structures with minimal HAZ and formation of stoichiometric nanoparticles and nano-ripples on the surfaces of crystalline SiC.

## Acknowledgements

This material is based in part upon work supported by the National Science Foundation under Grant Number CMMI-0619115. Any opinions, findings, and conclusions or recommendations expressed in this material are those of the author(s) and do not necessarily reflect the views of the National Science Foundation.

## References

1. Mehregany, M. and C.A. Zorman, *SiC MEMS: opportunities and challenges for applications in harsh environments*. Thin Solid Films, 1999. **355-356**: p. 518-524.
2. Zorman, C.A. and M. Mehregany. *Silicon Carbide for MEMS and NEMS - An Overview*. in *Sensors*. 2002: Proceedings of IEEE.

3. Sarro, P.M., *Silicon carbide as a new MEMS technology*. Sensors and Actuators A, 2000. **82**: p. 210-218.
4. *Silicon Carbide Micro ElectroMechanical Systems for Harsh Environments*, ed. R. Cheung. 2006, London, UK: Imperial College Press.
5. von Berg, J., et al., *High Temperature Piezoresistive  $\beta$ -SiC-on-SOI Pressure Sensor for Combustion Engines*. Materials Science Forum, 1998. **264-268**(1101-1106).
6. Pakula, L.S., et al., *Fabrication of a CMOS compatible pressure sensor for harsh environments*. Journal of Micromechanical Microengineering, 2004. **14**: p. 1478-1483.
7. Young, D.J., et al., *High-Temperature Single-Crystal 3C-SiC Capacitive Pressure Sensor*. IEEE Sensors Journal, 2004. **4**(4): p. 464-470.
8. Kuo, H.-I., C.A. Zorman, and M. Mehregany. *Fabrication and Testing of Single Crystalline 3C-SiC Devices using a Novel SiC-on-Insulator Substrate*. in *12th International Conference on Transducers, Solid-State Sensors, Actuators and Microsystems*. 2003. Cleveland, OH, USA.
9. Okojie, R.S., et al.  *$\alpha(6H)$ -SiC Pressure Sensors at 350°C*. in *International Electron Devices Meeting*. 1996. San Francisco, CA, USA.
10. Okojie, R.S., et al. *Failure Mechanisms in MEMS Based Silicon Carbide High Temperature Pressure Sensors*. in *45th annual IEEE International Reliability Physics Symposium*. 2007. NASA Glen Research Center, Cleveland, OH, USA.
11. Ned, A.A., et al., *Improved SiC Leadless Pressure Sensors for High Temperature*, in *Twenty-First Transducer Workshop*. 2004: Lexington, MD, USA.

12. Okojie, R.S., A.A. Ned, and A.D. Kurtz, *Operation of  $\alpha(6H)$ -SiC pressure sensor at 500°C*. Sensors and Actuators A, 1998. **66**: p. 200-204.
13. Atwell, A.R., et al., *Simulation, fabrication and testing of bulk micromachined 6H-SiC high-g piezoresistive accelerometers*. Sensors and Actuators A, 2003. **104**: p. 11-18.
14. Lohner, K.A., et al., *Microfabricated Silicon Carbide Microengine Structures*. Material Research Symposium Proceedings, 1999. **546**: p. 85-90.
15. Yasseen, A.A., C.A. Zorman, and M. Mehregany, *Fabrication and Testing of Surface Micromachined Polycrystalline SiC Micromotors*. IEEE Electron Device Letters, 2000. **21**(4): p. 164-166.
16. Hornberger, J., et al. *Silicon Carbide (SiC) Semiconductor Power Electronics for Extreme High-Temperature Environments*. in *IEEE Aerospace Conference Proceedings*. 2004.
17. Melzak, J.M. *Silicon Carbide RF MEMS*. in *IEEE MTT-S Interational Microwave Symposium*. 2003. Solon, OH, USA.
18. Shigematsu, I., et al., *Analysis of constituents generated with laser machining of Si<sub>3</sub>N<sub>4</sub> and SiC*. Journal of Material Science Leters, 1998. **17**: p. 737-739.
19. Sciti, D. and A. Bellosi, *Laser Micromachining of Silicon Carbide*. Key Engineering Materials, 2002. **206-213**: p. 305-308.
20. Wood, R.F. and D.H. Lowndes, *Laser Processing of Wide Band Gap Semiconductors and Insulators*. Defects and Amorphous Materials, 1985. **12**: p. 475-497.
21. Medvid, A. and P. Lytvyn, *Dynamics of Laser Ablation of SiC*. Materials Science Forum, 2004. **457-460**: p. 411-414.

22. Palma, C., M.C. Rossi, and C. Sapia, *CW-laser crystallisation of amorphous SiC alloys*. Electronics Letters, 1998. **34**: p. 1430-1431.
23. Lyalin, A.A., et al., *Pulsed Laser Activation and Electroless Metallization of SiC Single Crystal*, in *High Temperature Electronics Conference HITEC*. 1998: Albuquerque, NM, USA. p. 308-312.
24. Dolgaev, S.I., et al., *Laser-induced fast etching and metallization of SiC ceramics*. Applied Surface Science, 1997. **109-110**: p. 559-562.
25. Jandeleit, J., et al., *Fundamental investigations of micromachining by nano-and picosecond laser radiation*. Applied Surface Science, 1998. **127-129**: p. 885-891.
26. Zoppel, S., et al., *Laser micro machining of 3C-SiC single crystals*. Microelectronic Engineering, 2006. **83**: p. 1400-1402.
27. Dong, Y. and P. Molian, *Femtosecond pulsed laser ablation of 3C-SiC thin film on silicon*. Applied Physics A, 2003. **77**: p. 839-846.
28. Dong, Y. and P. Molian, *Coulomb explosion-induced formation of highly oriented nanoparticles on thin films of 3C-SiC by the femotsecond pulsed laser*. Applied Physics Letters, 2004. **84**(1): p. 10-12.
29. Dong, Y. and P. Molian, *In-situ formed nanoparticles on 3C-SiC film under femtosecond pulsed laser irradiation*. Physica Status Solidi (a), 2005. **202**(6): p. 1066-1072.
30. Dong, Y., C.A. Zorman, and P. Molian, *Femtosecond pulsed laser micromachining of single crystalline 3C-SiC structures based on a laser-induced defect-activation process*. Journal of Micromechanical Microengineering, 2003. **13**: p. 680-685.

31. Pecholt, B., et al., *Ultrafast laser micromachining of 3C-SiC thin films for MEMS device fabrication*. International Journal of Advanced Manufacturing Technology, 2007.
32. Farsari, M., et al., *Efficient femtosecond laser micromachining of bulk 3C-SiC*. Journal of Micromechanical Microengineering, 2005. **15**: p. 1786-1789.
33. Urban, S. and F. Falk, *Laser crystallization of amorphous SiC thin films on glass*. Applied Surface Science, 2001. **184**(1-4): p. 356-361.
34. Reitano, R., P. Baeri, and N. Marino, *Excimer laser induced thermal evaporation and ablation of silicon carbide*. Applied Surface Science, 1996. **96-98**: p. 302-308.
35. Reitano, R. and P. Baeri, *Excimer laser induced thermal evaporation and ablation of silicon carbide*. Nuclear Instruments and Methods in Physics Research B, 1996. **116**: p. 369-372.
36. Zhang, J., et al., *Precise microfabrication of wide band gap semiconductors (SiC and GaN) by VUV-UV multiwavelength laser ablation*. Applied Surface Science, 1998. **127-129**: p. 793-799.
37. Zhang, J., et al., *Direct photoetching of single crystal SiC by VUV-266 nm multiwavelength laser ablation*. Applied Physics A: Materials Science & Processing, 1997. **64**: p. 367-371.
38. Sugioka, K.M., Katsumi. *Novel technology for laser precision microfabrication of hard materials*. in *First International Symposium on Laser Precision Microfabrication*. 2000: SPIE.
39. Boutopoulos, C., et al., *Laser annealing of Al implanted silicon carbide: Structural and optical characterization*. Applied Surface Science, 2007. **253**: p. 7912-7916.

40. Palma, C. and C. Sapia, *Laser Pattern-Write Crystallization of Amorphous SiC Alloys*. Journal of Electronic Materials, 2000. **29**(5): p. 607-610.
41. Kim, S., et al., *SiC via holes by laser drilling*. Journal of Electronic Materials, 2004. **33**(5): p. 477-480.
42. Kim, S., et al., *High-Rate Laser Ablation for Through-Wafer Via Holes in SiC Substrates and GaN/AlN/SiC Templates*. Journal of Semiconductor Technology and Science, 2004. **4**(4): p. 217-221.
43. *Laser Ablation: Principal and Application*, ed. J.C. Miller. 1994, New York, NY, USA: Springer-Verlag.
44. Chou, S.Y., et al., *Annealing of implantation damage and redistribution of impurities in SiC using pulsed excimer laser*. Applied Physics Letters, 1990. **56**: p. 530-532.
45. Hishida, Y., et al., *Excimer Laser Annealing of Ion-implanted 6H-Silicon Carbide*. Materials Science Forum, 2000. **338-342**: p. 873-876.
46. Baeri, P., C. Spinella, and R. Reitano, *Fast Melting of Amorphous Silicon Carbide Induced by Nanosecond Laser Pulse*. International Journal of Thermophysics, 1999. **20**(4): p. 1211-1221.
47. Hedler, A., et al., *Excimer laser crystallization of amorphous silicon carbide produced by ion implantation*. Applied Surface Science, 2003. **205**: p. 240-248.
48. Ahmed, S., C.J. Barbero, and T.W. Sigmon, *Activation of ion implanted dopants in  $\alpha$ -SiC*. Applied Physics Letters, 1995. **66**: p. 712-714.
49. Sands, D., et al., *Optical Characterization of Lattice Damage and Recovery in Ion-Implanted and Pulsed Excimer Laser Irradiated 4H-SiC*. Materials Science Forum, 2000. **338-342**.

50. Key, P.H., et al., *Infrared reflectivity of ion-implanted and pulsed excimer laser irradiated 4H-SiC*. Thin Solid Films, 2000. **364**: p. 200-203.
51. Cho, N.I., et al., *Laser annealing effect of SiC films prepared by PECVD (plasma enhanced chemical vapor deposition)*. Thin Solid Films, 2002. **409**: p. 1-7.
52. Pearton, S.J., et al., *Enhanced functionality in GaN and SiC devices by using novel processing*. Solid-State Electronics, 2004. **48**(10-11): p. 1965-1974.
53. Zenketes, K., et al., *Via Hole Formation in Silicon Carbide by Laser Micromachining*. Materials Science Forum, 2006. **527-529**: p. 1119-1121.
54. Dong, Y., in *Mechanical Engineering*. 2003, Iowa State University: Ames, IA, USA.
55. Tian, Z., et al., *Effects of different laser sources and doping methods used to dope silicon carbide*. Acta Materialia, 2005. **53**: p. 2835-2844.
56. Shafeev, G.A., et al., *Electroless metallization of SiC after laser ablation*. Surface Coatings Technology, 1996. **80**: p. 224-228.
57. Shafeev, G.A., et al., *Uncongruent laser ablation and electroless metallization of SiC*. Applied Physics Letters, 1996. **68**: p. 773-775.
58. Tomita, T., K. Kinoshita, and S. Matsuo, *Surface structures of femtosecond laser irradiated 4H-SiC crystal*, in *CLEO/Pacific Rim Conference on Lasers and Electro-Optics*. 2005. p. 1744.
59. Tomita, T., et al., *Effect of surface roughening on femtosecond laser-induced ripple structures*. Applied Physics Letters, 2007. **90**: p. 153115-1-153115-3.
60. Tian, Z., N.R. Quick, and A. Kar, *Laser-enhanced diffusion of nitrogen aluminum dopants in silicon carbide*. Acta Materialia, 2006. **54**: p. 4273-4283.

61. Tian, Z., *Laser Metallization and Doping for Silicon Carbide Diode Fabrication and Endotaxy*, in *Engineering and Computer Science*. 2006, University of Central Florida: Orlando Florida. p. 167.
62. García, B., et al., *Differences in the Laser Annealing of a-Si:H and a-SiC films*, in *Fifth IEEE International Caracas Conference on Devices, Circuits, and Systems*. 2004: Dominican Republic. p. 164-167.
63. Dutto, C., E. Foggarassy, and D. Mathiot, *Numerical and experimental analysis of pulsed excimer laser processing of silicon carbide*. *Applied Surface Science*, 2001. **184**: p. 362-366.
64. Salama, I.A., N.R. Quick, and A. Kar, *Laser direct write doping of wide-bandgap semiconductor materials*, in *International Symposium on Compound Semiconductors*. 2004: Orlando, FL, USA. p. 1-7.
65. Dijkkamp, D. and T. Venkatesan, *Preparation of Y-Ba-Cu oxide superconductor thin films using pulsed laser evaporation from high T<sub>c</sub> bulk material*. *Applied Physics Letters*, 1987. **51**: p. 619-621.
66. Pehrsson, P.E. and R. Kaplan, *Excimer laser cleaning, annealing, and ablation of  $\beta$ -SiC*. *Journal of Materials Research*, 1989. **4**(6): p. 1480-1490.
67. Muehlhoff, L., et al., *Comparitive electron spectroscopic studies of surface segregation on SiC(0001) and SiC(000 $\bar{1}$ )*. *Journal of Applied Physics*, 1986. **60**: p. 2842-2853.
68. Song, Y. and F.W. Smith, *Phase diagram for the interaction of oxygen with SiC*. *Applied Physics Letters*, 2002. **81**(16): p. 3061-3063.

69. Soe, W.-H. and K.-H. Rieder, *Surface phonon and valence band dispersions in graphite overlayers formed by solid-state graphitization of 6H-SiC(0001)*. Physical Review B, 2004. **70**: p. 115421-1-115421-6.
70. Adachi, S., M. Mohri, and T. Yamashina, *Surface Graphitization Process of SiC (0001) Single-Crystal at Elevated Temperatures*. Surface Science, 1985. **161**: p. 479-490.
71. Bellina, J.J.J., *Stoichiometric changes in the surface of (100) cubic SiC caused by ion bombardment and annealing*. Applied Surface Science, 19986. **380**: p. 380-390.
72. *Properties of Silicon Carbide*. EMIS Datareviews Series, ed. G.L. Harris. Vol. 13. 1995, London, UK: INSPEC, the Institution of Electrical Engineers.
73. Salama, I.A., N.R. Quick, and A. Kar, *Laser Direct-Metallization of Silicon Carbide without Metal Deposition*. Materials Research Society Proceedings, 2003. **764**.
74. Zhang, J., et al., *Direct photoetching of single crystal SiC by VUV-266 nm multiwavelength laser ablation* Applied Physics A: Materials Science & Processing, 1997. **64**: p. 367-371.
75. Kreutz, E.W., R. Weichenhain, and A. Horn. *Nd:YAG laser micromachining of SiC precision structures for MEMS*. in *MEMS design, fabrication, characterization, and packaging*. 2001.
76. *Process Technology for Silicon Carbide*. EMIS Processing, ed. C.-M. Zetterling. 2002, London, UK: INSPEC, The Institution of Electrical Engineers. 176.
77. Tabbal, M., et al., *Amorphous to crystalline phase transition in pulsed laser deposition silicon carbide*. Applied Surface Science, 2007. **253**: p. 7050-7059.

78. Bet, S., N. Quick, and A. Kar, *Laser-doping of silicon carbide for p-n junction and LED fabrication*. Physica Status Solidi (a), 2007. **204**(4): p. 1147-1157.
79. Tian, Z., N.R. Quick, and A. Kar, *Characterization of 6H-Silicon Carbide PIN Diodes Prototyping by Laser Doping*. Journal of Electronic Materials, 2005. **34**(4): p. 430-438.
80. Key, P.H., et al., *Infra-red reflectivity of ion-implanted and pulsed excimer laser irradiated 4H-SiC*. Thin Solid Films, 2000. **364**: p. 200-203.
81. Bae, I.-T., M. Ishimaru, and Y. Hirotsu, *Dose Dependence of Recrystallization Process in Amorphous SiC*. Japanese Journal of Applied Physics, 2005. **44**(8): p. 6196-6200.
82. Hobert, H., et al., *Laser-induced changes in silicon carbon films studied by vibrational spectroscopy*. Vibrational Spectroscopy, 2002. **29**: p. 177-182.
83. Nagasawa, H. and K. Yagi, *3C-SiC Single-Crystal Films Grown on 6-Inch Si Substrates*. Physica Status Solidi (a), 1997. **202**: p. 335-358.
84. Hatayama, T., et al., *Low-temperature heteroepitaxial growth of cubic SiC on Si using hydrocarbon radicals by gas source molecular beam epitaxy*. Journal of Crystal Growth, 1995. **150**: p. 934-938.
85. Toal, S.J., H.S. Reehal, and C. Jaynes, *Growth of microcrystalline  $\beta$ -SiC films on silicon by ECR plasma CVD*. Applied Surface Science, 1999. **138-139**: p. 424-428.
86. Balooch, M., et al., *Deposition of SiC films by pulsed excimer laser ablation*. Applied Physics Letters, 1990. **57**: p. 1540.
87. Ghica, C., et al., *Growth and characterization of  $\beta$ -SiC films obtained by fs laser ablation*. Applied Surface Science, 2006. **252**: p. 4672-4677.

88. Craciun, V., et al., *Growth of dense SiC films on Si at medium temperatures by pulsed laser deposition*. Journal of Vacuum Science Technology A, 2000. **19**: p. 2691-2694.
89. Katharria, Y.S., et al., *Characterization of pulsed laser deposited SiC thin films*. Journal of Non-Crystalline Solids, 2007. **353**: p. 4660-4665.
90. Huang, J., et al., *Effect of annealing on SiC thin films prepared by pulsed laser deposition*. Diamond & Related Materials, 1000. **8**: p. 2099-2102.
91. Soto, G., et al., *Growth of SiC and SiC<sub>x</sub>N<sub>y</sub> films by pulsed laser ablation of SiC in Ar and N<sub>2</sub> environments*. Journal of Vacuum Science Technology A 1998. **16**: p. 1311-1315.
92. Chauhan, A., et al., *Pulsed laser deposition of silicon carbide on heat resistant materials*. Scripta Matereritalia, 2005. **52**: p. 735-738.
93. Muto, H., S.-i. Kamiya, and T. Kusumori, *Growth mechanism of  $\alpha$ -SiC hetero-epitaxial films by PLD as studied on the laser photon, pulse-width and substrate dependence*. Optical Materials, 2003. **23**: p. 43-47.
94. Wang, Y., et al., *The preparation of single-crystal 4H-SiC film by pulsed XeCl laser deposition*. Thin Solid Films, 1999. **338**: p. 93-99.
95. Huang, J., et al., *Effect of annealing on SiC thin films prepared by pulsed laser deposition*. Diamond & Related Materials, 1999. **8**: p. 2099-2102.
96. Craciun, V., et al., *Growth of dense SiC films on Si at medium temperatures by pulsed laser deposition*. Journal of Vacuum Science Technology A, 2001. **19**: p. 2691-2694.
97. Tang, Y.H., et al., *Preparation and characterization of pulsed laser depostion (PLD) SiC films*. Applied Surface Science, 2006. **252**: p. 3386-3389.

98. Tabbal, M., S. Isber, and T.C. Christidis, *Effect of deposition temperature on the optical transmission and paramagnetic centers in pulsed laser deposited amorphous silicon carbide thin films*. Journal of Applied Physics, 2000. **88**(9): p. 5127-5133.
99. Katharria, Y.S., et al., *Characterizations of pulsed laser deposited SiC thin films*. Journal of Non-Crystalline Solids, 2007. **353**: p. 4460-4665.
100. Zhao, Q.Z., et al., *Enhancement of optical absorption and photocurrent of 6H-SiC by laser surface nanostructuring*. Applied Physics Letters, 2007. **91**: p. 121107-1-121107-3.
101. Birnbaum, M., *Semiconductor Surface Damage Produced by Ruby Lasers*. Journal of Applied Physics, 1965. **36**.
102. Yasumaru, N., K. Miyazaki, and J. Kiuchi, *Femtosecond-laser-induced nanostructure formed on hard thin films of TiN and DLC*. Applied Physics A, 2003. **76**: p. 983-985.
103. Shimotsuma, Y., et al., *Self-Organized Nanogratings in Glass Irradiated by Ultrashort Light Pulses*. Physical Review Letters, 2003. **91**(24): p. 247405-1-247405-4.
104. Ozkan, A.M., et al., *Femtosecond laser-induced periodic structure writing on diamond crystals and microclusters*. Applied Physics Letters, 1999. **75**(23): p. 3716-3718.
105. Wu, Q., et al., *Femtosecond laser-induced periodic surface structure on diamond film*. Applied Physics Letters, 2003. **82**(11): p. 1703-1705.
106. Reif, J., et al., *Ripples revisited: non-classical morphology at the bottom of femtosecond laser ablation craters in transparent dielectrics*. Applied Surface Science, 2002. **197-198**: p. 891-895.

107. Costache, F., M. Henyk, and J. Reif, *Modification of dielectric surfaces with ultra-short laser pulses*. Applied Surface Science, 2002. **186**: p. 352-357.
108. Hnatovsky, C., et al., *Pulse duration dependence of femtosecond-laser-fabricated nanogratings in fused silica*. Applied Physics Letters, 2005. **87**: p. 014104-1-014104-3.
109. Boroweic, A. and H.K. Haugen, *Subwavelength ripple formation on the surfaces of compound semiconductor irradiated with femtosecond laser pulses*. Applied Physics Letters, 2003. **82**(25): p. 4462-4464.
110. Jia, T.Q., et al., *Formation of nanogratings on the surface of a ZnSe crystal irradiated by femtosecond laser pulses*. Physical Review B, 2005. **72**: p. 125429-1-125429-4.
111. Jia, T.Q., et al., *Alignment of nanoparticles formed on the surface of 6H-SiC crystals irradiated by two collinear femtosecond laser beams*. Applied Physics Letters, 2006. **88**: p. 111117-1-111117-3.
112. Juodkazis, S., et al. *Three-dimensional laser microfabrication of metals, semiconductors, and dielectrics*. in *Laser-assisted micro- and nanotechnologies; International Conference on Lasers, Applications, and Technologies*. 2007. Minsk, Bela: Proceedings of SPIE.
113. *The MEMS Handbook*, ed. M. Gad-el-Hak. 2002, Boca Raton, FL, USA: CRC Press.
114. Shor, J.S. and A.D. Kurtz, *Dopant-selective etch stops in 6H and 3C-SiC*. Journal of Applied Physics, 1997. **81**: p. 1546-1551.
115. Kreutz, E.W., et al., *Microstructuring of SiC by laser ablation with pulse duration from ns to fs range (LAMP 2002)*. RIKEN Review, 2003(50): p. 83-86.

116. Desbiens, J.-P. and P. Masson, *ArF excimer laser micromachining of Pyrex, SiC and PZT for rapid prototyping of MEMS components*. Sensors and Actuators A, 2007. **136**: p. 554-563.
117. Medvid, A. *Dynamics of laser ablation in SiC*. in *Conference on Laser and Electro-Optics Europe, 2003, CLEO/Europe*. 2003: Material Science Forum.
118. Anderson, T., et al., *Laser ablation of via holes in GaN and AlGaIn/GaN high electron mobility transistor structures*. Journal of Vacuum Science Technology B, 2006. **24**(5): p. 2246-2249.
119. Anderson, T.J., et al., *Comparison of Laser-Wavelength Operation for Drilling of Via Holes in AlGaIn/GaN HEMTs on SiC Substrates*. Journal of Electronic Materials, 2006. **35**(4): p. 675-679.

## CHAPTER 4. ULTRAFAST LASER MICROMACHINING OF 3C-SiC THIN FILMS FOR MEMS DEVICE FABRICATION

(A paper published in International Journal of Advanced Manufacturing Technology Ben Pecholt, Monica Vendan, Yuanyuan Dong, Pal Molian)

### 4.1. Abstract

Femtosecond pulsed laser (800 nm, 120 fs) micromachining of thin films of 3C-SiC ( $\beta$ -SiC) semiconductor deposited on silicon substrate was investigated as a function of pulse energy (0.5  $\mu$ J to 750  $\mu$ J). The purpose is to establish suitable laser parametric regime for the fabrication of high accuracy, high spatial resolution and thin diaphragms for high-temperature MEMS pressure sensor applications. Etch rate, ablation threshold and quality of micromachined features were evaluated. The governing ablation mechanisms, such as thermal vaporization, phase explosion, Coulomb explosion and photomechanical fragmentation, were correlated with the effects of pulse energy. The results show that the etch rate is higher and the ablation threshold is lower than those obtained with nanosecond pulsed excimer laser ablation, suggesting femtosecond laser's potential for rapid manufacturing. In addition, the etch rates were substantially higher than those achievable in various reactive ion and electrochemical etching methods. Excellent quality of machined features with little collateral thermal damage was obtained in the pulse energy range (1–10  $\mu$ J). The leading material removal mechanisms under these conditions were photomechanical fragmentation, ultrafast melting and vaporization. At very low pulse energies (<1  $\mu$ J), nanoscale material removal has occurred with the formation of nanoparticles that is attributed

to Coulomb explosion mechanism. The effect of assist gas on the process performance at low and high energy fluences is also presented.

## 4.2. Introduction

Silicon is the current material dominating the microelectronics and MEMS industries today. Silicon carbide (SiC), however, has superior properties compared to silicon in terms of bandgap, high-temperature resistance, thermal conductivity, mechanical strength and stiffness, all of which strongly favor it for its utility as sensors, actuators and power devices. SiC exists in over 170 different polytypes and each type has its own distinct set of electronic properties. However, only three polytypes, namely 3C, 4H and 6H, are acceptable for use as semiconductors because they can be grown as single crystal wafers. 3C-SiC is preferred for its ability to provide the highest speed of electron and hole transport in the crystal while 6H-SiC and 4H-SiC are desired for their wide bandgaps. All polytypes are extremely hard, chemically inert and have high thermal conductivity. For MEMS devices, 3C-SiC serves as the best mechanical substrate due to its extreme hardness and stiffness. However, there are formidable challenges in the crystal growth of high quality, bulk wafers of 3C-SiC that prevents its commercial production. Hence thin films of 3C-SiC are widely used for fabricating MEMS devices. The 3C polytype, also known as  $\beta$ -SiC, exhibits cubic structure, crystallizes in ZnS-type structure and epitaxially grows as thin film on silicon substrate. It also requires much lower substrate temperature (1,500°C or less) than other polytypes in chemical vapor deposition (CVD). In contrast, the 6H-SiC (hexagonal) and 4H-SiC (tetragonal) would not grow as thin film on any substrate except on its own and also requires

very high temperature (2,000°C) for growth. CVD, sputtering, metal-organic CVD, atomic layer epitaxy, molecular beam epitaxy, and pulsed laser deposition are the current techniques used to grow amorphous, single and polycrystalline forms of 3C-SiC thin films [1, 2].

MEMS devices, such as pressure sensors, accelerometers, lateral resonators, gas sensors and micromotors for use in harsh environments, are fabricated by surface micromachining of 3C-SiC thin films [3-5]. Conventional surface micromachining of single crystalline SiC film on silicon is difficult to accomplish in contrast to polycrystalline and amorphous SiC layers.

Poly-SiC is generally grown on poly-Si layer or deposited on SiO<sub>2</sub> layer. The SiC is the structural layer while the poly-Si or SiO<sub>2</sub> is the sacrificial layer. KOH and HF are used to release the SiC microstructures from poly-Si and oxide layers, respectively. One critical microfabrication issue is that the traditional wet etching does not work well for SiC.

Patterning techniques based on photolithography and reactive-ion-etching (RIE) with SF<sub>6</sub>/O<sub>2</sub> plasma, SF<sub>6</sub>/O<sub>2</sub> inductively coupled plasma (ICP) and deep reactive ion etching (DRIE) processes were customarily used to etch SiC thin films, however, at the expense of very slow etch rates (few nm per second). Photo- and electro-chemical etching processes can also be used where SiC is first anodized to form a deep porous layer and subsequently removed through thermal oxidation followed by a dip in HF; however, these processes suffer from poor etch selectivity, low etch rates and cumbersome process steps [4]. In the micro-manufacturing industry, the laser is being established as an indispensable tool because of the benefits such as higher etch rates, easier automation and better quality features. Excimer lasers are extensively used for micromachining polymers and ceramics while Nd:YAG lasers are used for microdrilling and marking of semiconductors and metals. However, these lasers (nanosecond to millisecond pulses) are not well suited for precise microstructuring due to

thermal or mechanical damages (recast layers, burrs and cracks, etc.), limiting the achievable precision and quality. These shortcomings have spurred the development of ultrafast (pico- and femtosecond) lasers, which deliver enhanced precision and cleanliness of machined features by minimizing collateral damage, plasma effects and thermal diffusion [6-9].

Femtosecond (fs) pulsed lasers are emerging as tools for microfabrication of all types of materials that are used in biomedical, microelectronics, photonics and MEMS industries. The unique characteristics of ultrafast lasers over longer-pulsed lasers are multiphoton ionization and absence of energy transfer from electrons to the lattice, leading to deterministic and reproducible ablation; negligible thermal damage; and high etch rates (0.01 to 1  $\mu\text{m}/\text{pulse}$ ). These unique advantages make femtosecond lasers promising for the fabrication of a variety of materials, such as low melting point polymers, high thermal conductivity metals, wide bandgap dielectrics, and semiconductors that are otherwise difficult to perform by conventional tools. Applications of femtosecond laser micro-structuring of channels and trenches have been demonstrated in materials such as fused silica, silicon, and pyrex [10]. Microfluidic channels as deep as 50 microns were successfully machined in Si(100) at 395 nm with a fluence of 0.6 J/cm<sup>2</sup> [10]. Micro-structures on alumina ceramic, which is typically affected by tool wear, were machined up to 150  $\mu\text{m}$  deep using a scanned intensity in the range of 7–50 W/cm<sup>2</sup> and only a 2  $\mu\text{m}$  thick recast layer was observed at the bottom of the structure [11]. Femtosecond lasers with their minimal thermal effects have been successfully used to create microstructures in aluminum with quality side walls despite its high thermal conductivity and low melting point [12, 13]. Damaging fs-laser effects on metals were also shown to be mitigated with the use of helium as an assist gas [12-14]. The fs-laser has already been demonstrated to have a “nonthermal” ablation mechanism for micro-structuring

of 3C-SiC thin film [5]. Reported use of femtosecond pulses to successfully drill holes in 3C-SiC bulk wafers [15] and trenches up to 60  $\mu\text{m}$  deep in 6H-SiC [16] suggests that ultra-short pulses are well suited for machining bulk silicon carbide as well as 3C-SiC thin film [5]. In this paper, we present the results of a systematic study of the effects of pulse energy on etch depth, quality of machined features and material removal mechanisms in 3C-SiC thin films on Si(100) substrate using a Ti:sapphire femtosecond pulsed laser.

### 4.3. Experimental details

Atmospheric pressure chemical vapor deposition (APCVD) system was employed to grow 1- $\mu\text{m}$  thin films of 3C-SiC on 100-mm diameter, 500- $\mu\text{m}$  thick (100) silicon substrates in a cold-wall, vertical-geometry, RF inductionheated, atmospheric pressure CVD reactor. Prior to deposition, the reaction chamber was pumped down to a pressure of 200 mtorr and then backfilled with ultra-high purity argon to 760 torr to remove the oxide impurities. Ultra-high purity hydrogen (carrier gas), propane (15% hydrogen) and silane (5% hydrogen) were then introduced into the chamber. The chemical reaction took place at 1,360°C. A three-step deposition process was used, beginning with an in situ hydrogen etch of oxides and contaminants, followed by the formation of a carbonized layer on the substrate surface, and ending with the film growth. The film growth rate was about one  $\mu\text{m}$  per hour. Details of this technique are described elsewhere [17]. A Ti:sapphire laser (Spectra Physics, Hurricane X), based on the chirped pulse amplification (CPA) technique, was used to create microholes and microchannels in 3C-SiC thin films. The output beam has the specifications of wavelength of 800-nm, repetition rate of 1-kHz, and pulse width of 120-fs. The 6-mm diameter laser beam

with a Gaussian energy distribution was circularly polarized, expanded to twice the size using an up collimator, and steered by a 45° mirror. The beam was then transmitted through neutral density filter to reduce the pulse energy and then focused by a reflective objective lens to a spot size of  $4\pm 1 \mu\text{m}$ . In experiments with higher pulse energies ( $>100 \mu\text{J}$ ), a plano-convex lens (50 mm focal length) was used giving rise to a spot size of  $40\pm 5 \mu\text{m}$ . The pulse energy was varied from  $1 \mu\text{J}$  to  $750 \mu\text{J}$ . For ablation rate studies, single-shot mode was used with energy fluence in the range 0.1 to  $20 \text{ J/cm}^2$ . 3C-SiC thin film deposited samples were cleaned with trichloroethylene, acetone and deionized water consecutively and then mounted on a computer controlled x-y stage (Coherent Lab Motion Series), which has a resolution of  $1 \mu\text{m}$ . The movement of the stage was programmed in the lab motion software to produce the desired laser path. The beam was used in the direct-writing mode to follow the program. Helium was used as a shield/assist gas to eject vaporized material, produce clean cuts and protect the lens. In some experiments, air was also used as the assist gas to identify the effects of self-focusing. After laser micromachining, a few samples were etched in KOH solution for about 5–10 minutes to remove the recast layers. Scanning electron microscope, atomic force microscope and surface profilometer were then used to examine the ablated regions and measure the etch depths.

#### 4.4. Results and discussion

Etch rate and ablation threshold Etch rate is an overriding consideration in SiC micromachining because of its chemical inertness and extreme hardness. Figure 8 shows the etch depth per pulse as a function of energy fluence based on experiments using 50 mm focal

length lens (40  $\mu\text{m}$  spot size). The non-linear dependence of ablation rate with fluence is attributed to multiphoton ionization. These etch rates are much higher than those obtained with nanosecond-pulsed excimer (193 nm, 248 nm) lasers and comparable to 400-fs (1026 nm) laser in the ablation of 3C-SiC bulk wafers [15]. Similarly, the etch rates are greater than maximum achievable (7 nm/s) in RIE, electron cyclotron resonance and magnetron-enhanced RIE [18, 19].

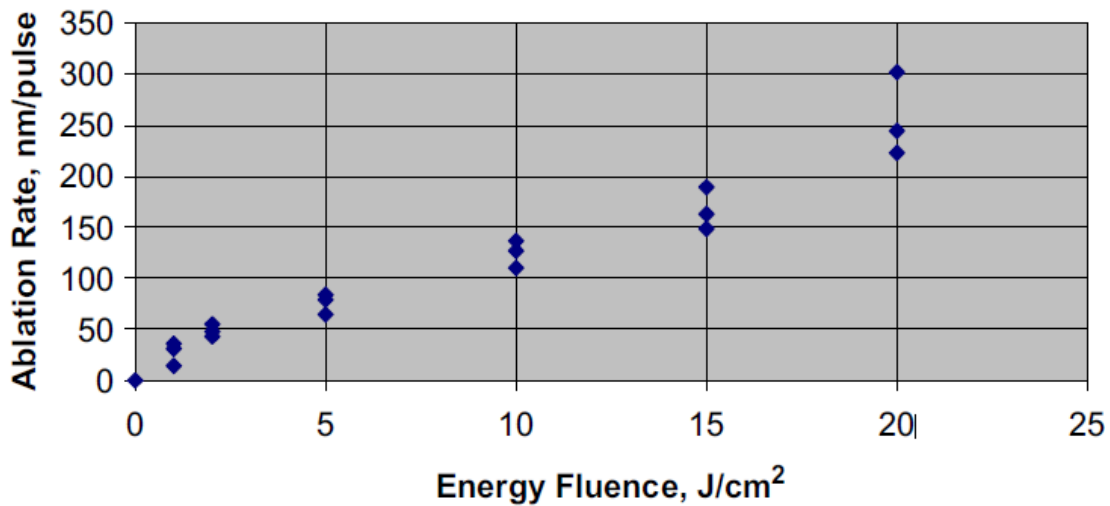


**Figure 8. Single-shot ablation rates of 3C-SiC thin films**

Higher etch rates observed in ultrafast laser ablation are attributed to multiphoton absorption and reduced thermal diffusion. In the ns-laser pulse regime, photon energy must exceed the summation of band gap (3 eV for SiC) and electron affinity (4.5 eV for SiC) to excite the electrons and cause bond scission. Although 800-nm photons cannot meet such energy requirements, the multiphoton absorption associated with extreme intensity of femtosecond pulse and the presence of lattice defects in 3CSiC thin films are responsible for bond breaking and subsequent emission of electrons and ions. Threshold ablation is a characteristic

dependent on the wavelength, pulse width and type of material. It is ideally defined as the energy fluence at which irreversible damage occurs in the material by removing a monolayer of material. It is actually determined by visual examination, ablation depth measurement, plasma radiation monitoring etc. However in this study the ablation threshold was estimated by recording the diameter (D) and the depth of single-shot ablated craters using atomic force microscope and then using the following linear relationship between the square of the crater diameter and the logarithm of the laser fluence [20] (Equation 4)

**Equation 4**

$$D^2 = 2w_o^2 \ln\left(\frac{F_o}{F_{th}}\right)$$

where  $F_{th}$  = ablation threshold and  $2w_o$  = spot size. A plot of the square of damage diameter,  $D^2$ , against the logarithm of energy fluence was made to obtain both the spot size (slope of line) and ablation threshold (the extrapolation of  $D^2$  to zero value). The spot size,  $2w_o$ , was  $40 \mu\text{m}$  and ablation threshold was  $0.7 \text{ J/cm}^2$ . For comparison, the ablation threshold of bulk 3C-SiC by 400-fs (1026 nm) and 34 ns (248 nm) lasers were  $0.55 \text{ J/cm}^2$  and  $1.5 \text{ J/cm}^2$  respectively. The lower threshold in ultrafast laser compared to 248 nm excimer laser is a consequence of multiphoton absorption effect. Effect of pulse width Figure 9 shows the scanning electron microscope (SEM) images of microchannels produced in 3C-SiC thin films using the 120-fs pulsed Ti:sapphire (800 nm) and 90-ns pulsed Nd:YAG (1064 nm) lasers. There were large amounts of debris and recast layer in the ns-pulsed laser micromachined region. The coating seems to have discolored and also delaminated away from the kerf. The laser beam has cut through the silicon substrate and made significant collateral thermal damages. In addition, a rough surface morphology, characterized by jagged protrusions, can

be seen. In contrast, the fs-laser machined region exhibits narrow kerf, relatively small amount of recast layer and almost no spatter. Thus, rapid energy deposition and its localization lead to fabrication of microstructures with high quality and reproducibility.

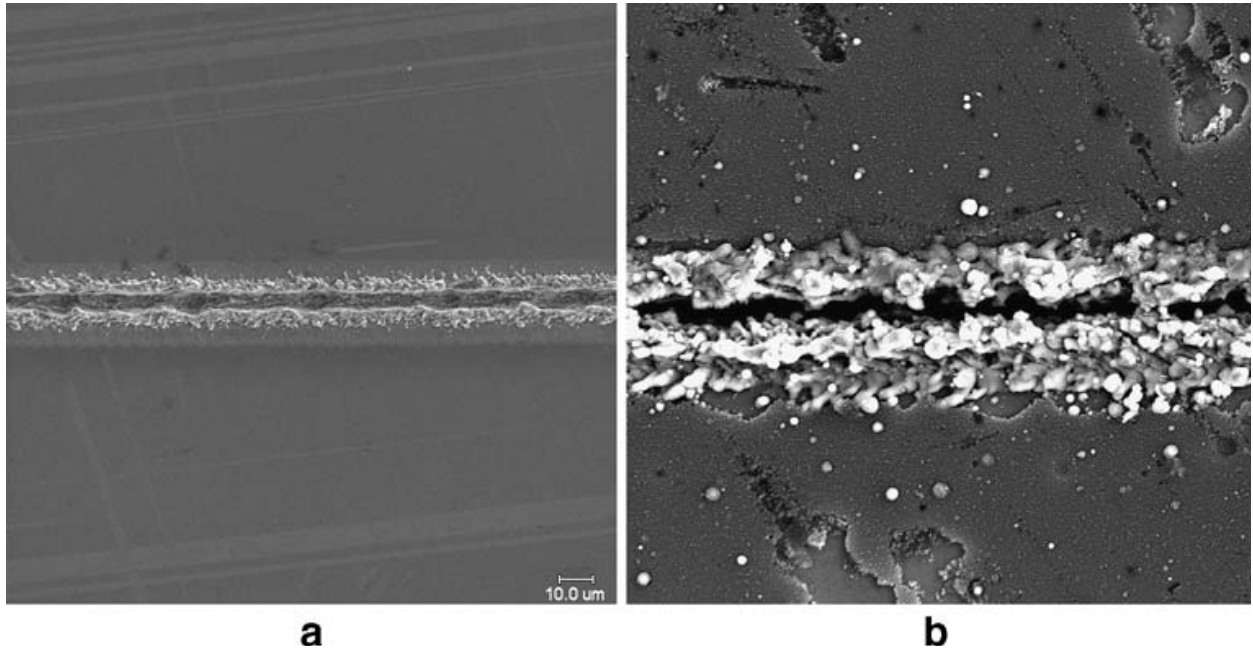


**Figure 9. Microchannels generated by (a) 120-fs laser (b) 90-ns laser under identical conditions: pulse energy 60  $\mu\text{J}$ , spot size 4  $\mu\text{m}$ , speed 1000  $\mu\text{m s}^{-1}$ .**

**Laser-material interactions** The physical mechanisms of femtosecond laser ablation of wide bandgap semiconductors such as SiC remains poorly understood. For example, the roles played by defects and impurities on the energy absorption and dissipation are not yet made clear. In general, at high intensities ( $>10^{13}$  W/cm<sup>2</sup>) of femtosecond lasers, multiphoton absorption becomes considerably strong and seed electrons are not required to begin ionization. Multiphoton ionization and free electron heating occur in SiC during the femtosecond pulse duration and hence the lattice temperature remains unchanged. Laser energy is deposited much faster than the ability of the material to dissipate energy, thus a

state of extreme non-equilibrium is reached and free electrons are generated ionizing the material into dense plasma. These plasmas have been shown to have highly reflective, metal-like properties [21]. Even plasmas formed on optically transparent materials have been shown to exhibit reflective properties [22]. Subsequent laser-plasma interaction causes phase change and material ejection (ablation). Additionally the free electrons associated with the ionization of the material are responsible for absorption of photons and defocusing of the beam [23]. Ionization of the gases used as a propagation medium in laser processing also result in a number of unfavorable consequences due competing phenomena, such as self-focusing and de-focusing [23]. Ionization-induced defocusing occurs when the gas medium results in plasma at the leading edge of the beam [24, 25]. A higher degree of ionization occurs at the center of the beam due to Gaussian beam energy distribution resulting in a larger index of refraction on the axial center [24, 26]. This type of ionization takes place when the beam energy is at the ionization potential of the gas. When the laser intensity is increased to higher values than the plasma threshold, the plasma becomes more uniform and the non-linear index of refraction generates self-focusing [26]. Gases with a high ionization potential such as helium have been used at ambient pressures in beam propagation [12] to avoid self focusing effects and as an assist gas to aid in plasma shielding resulting in a lower level of debris and diminished heat-affected-zone [12-14]. There are several mechanisms proposed for material removal in femtosecond laser ablation, which include normal melting [21], thermal vaporization [27], ultrafast laser melting [28-34], phase explosion [31-35], Coulomb explosion [36, 37] and photomechanical fragmentation [38-41] depending on laser intensity, pulse width, wavelength, number of pulses and material properties. Coulomb explosion, ultrafast melting and free electron heating arise in fast pace (femtosecond), while

thermal vaporization and fragmentation occur at slow pace (nanoseconds) [21]. Phase explosion, normal melting and electron-lattice relaxation take place in the intermediate picosecond scale. In the case of wide bandgap semiconductors such as SiC, one or more of these mechanisms could be operative depending on energy fluence. In this work, the observations of machined features are grouped in three regimes on the basis of pulse energy and then used to identify the underpinning physical mechanisms of micromachining of 3C-SiC thin films.

High energy ablation Figure 10 and Figure 11 show the microchannels and microholes produced by the femtosecond laser at much higher pulse energies (50  $\mu\text{J}$  to 750  $\mu\text{J}$ ). The presence of large amounts of recast layer and spatter as well as sub- $\mu\text{m}$ /pulse etch depth and rough surface suggests that thermal effects caused by phase explosion and vaporization mechanisms control the ablation. Phase explosion (PE), also known as explosive boiling or homogeneous nucleation of gas bubbles, precedes thermal vaporization. PE is a mechanism where the laser-irradiated matter enters the metastable region of the phase diagram (binodal or spinodal) by reaching the limit of thermodynamic stability and approaching the critical temperatures [42, 43]. When the temperature of the liquid approaches the critical point, the superheated liquid transforms into a mixture of liquid and vapor and undergoes evaporation at an excessive rate [44, 45]. Violent ejection of the mixture of vapor and liquid droplets occur from the sample surface due to the recoil force created by the momentum transfer. Evidence for the phase explosion mechanism in Figure 11 is the presence of splashed material around the holes and high density of redeposited particulates. PE, accompanied by

melt expulsion and collateral thermal damage, has been validated in femtosecond pulsed laser ablation of semiconductors [36].

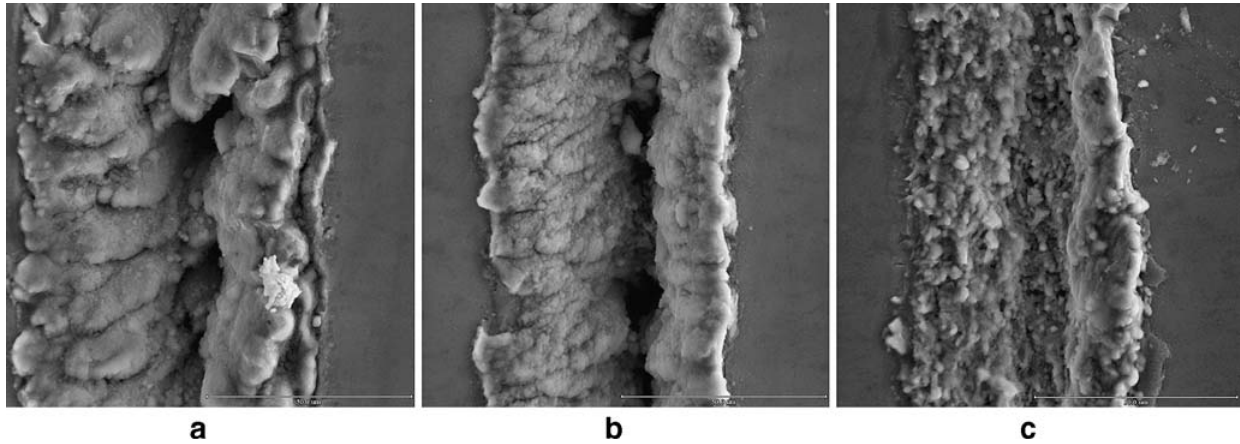


**Figure 10. Femtosecond micromachined holes in 3C-SiC thin film deposited on silicon at a speed of  $1000 \mu\text{m s}^{-1}$ ; (a)  $750 \mu\text{J}$  (b)  $500 \mu\text{J}$  (c)  $250 \mu\text{J}$**

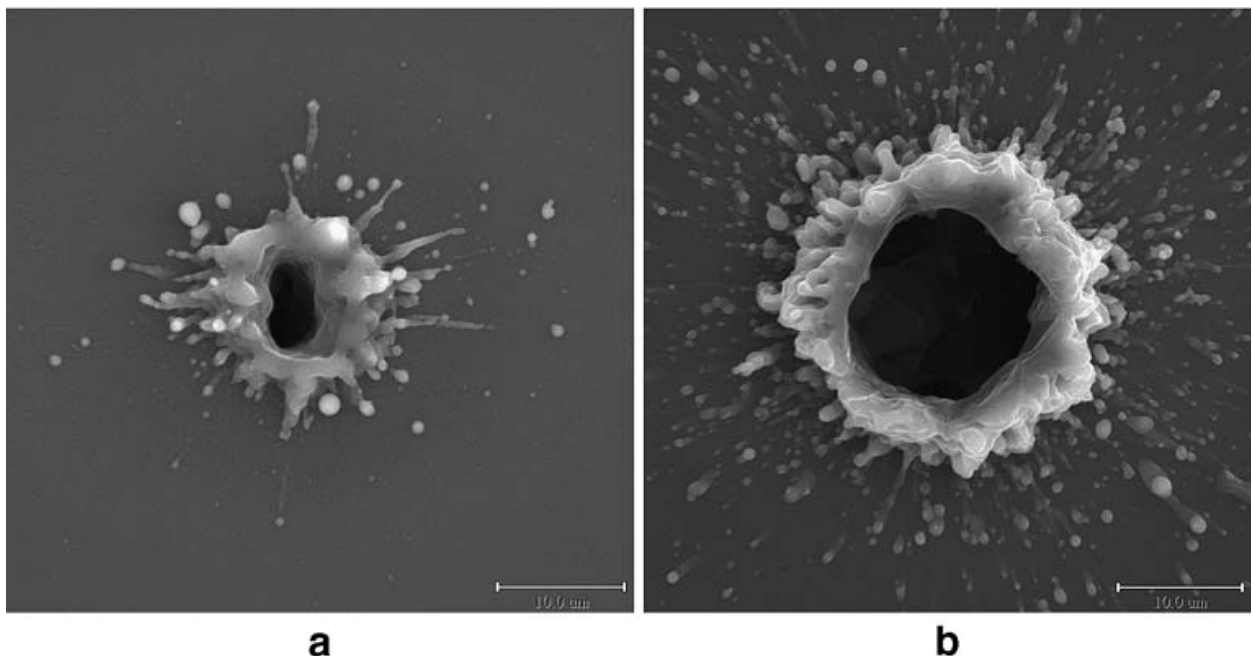


**Figure 11. Femtosecond laser micromachined holes in 3C-SiC thin films deposited on silicon with 30 pulses (a)  $50 \mu\text{J}$  (b)  $200 \mu\text{J}$**

PE generally removes small amount of material by vaporization. Thermal vaporization continues after phase explosion, causing large amount of material removal and forming the kerf. Although ultrafast lasers are expected to minimize such thermal effects, it appears that explosive vaporization accompanied by substantial melt formation does occur at high pulse energies, leading to poor quality cuts. Low energy ablation Figure 12 a to c show the channels micromachined in 3C-SiC using low pulse energies (2–10  $\mu\text{J}$ ). There are material fragments indicative of mechanical fracture and kerf pinpointing material loss through vaporization. In this regime, the mechanisms of material removal are believed to be a combination of ultrafast laser melting, vaporization, photomechanical fragmentation and Coulomb explosion (CE). Ultrafast melting of semiconductors at fluences above the damage threshold is theoretically proven as a non-thermal phase transition on a sub-ps time scale for semiconductors [21].

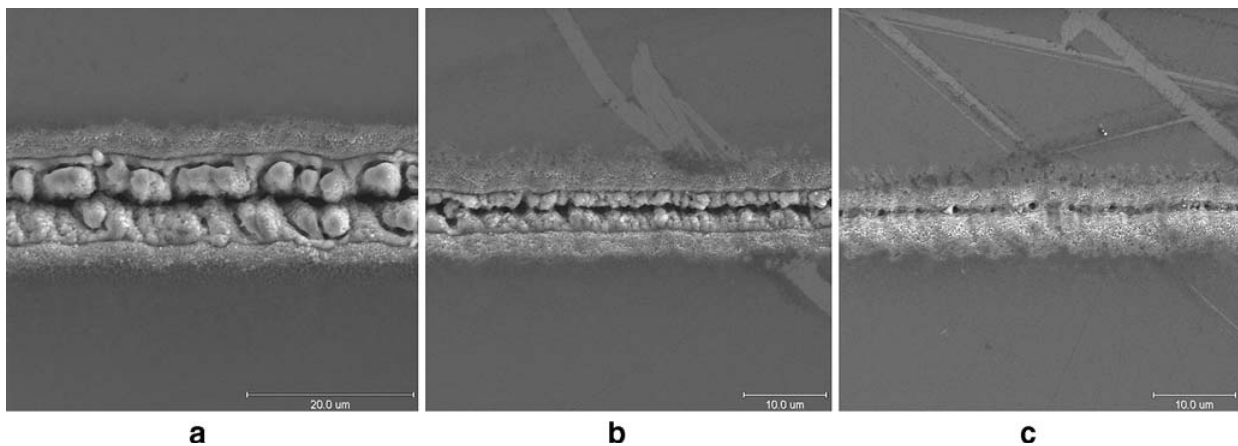


**Figure 12. Femtosecond laser micromachined channels in 3C-SiC thin films deposited on silicon at a speed of 20 (a) 5  $\mu\text{J}$ ; (b) 2.5  $\mu\text{J}$ ; (c) 1.5  $\mu\text{J}$**

It begins with the development of metal-like phase due to the dense electron-hole plasma followed by bond softening and lattice destabilization due to a significant fraction of electrons jumping from valence band to conduction band. For example, steep gradients of the

free electron density account for the depth of the non-thermally melted layer as 20–40 nm in Si [21]. Thermal melting, which takes place after ultrafast melting, produces much thicker melt layers. Thus ultrafast melting followed by normal melting and vaporization seems to be responsible for the formation of small kerf in Figure 12. However the most dominant mechanism appears to be photomechanical fragmentation where the material disintegrates into large clusters as a result of mechanical stress imposed by the rapid thermal expansion of the surface. In this mechanism, thermoelastic stresses are developed by the rapid thermal expansion of the surface layers due to constant-volume heating; the relaxation of these stresses cause large values of non-uniform strain rates, leading to a strong increase in elastic energy that breaks the material into an ensemble of clusters [27]. This strain-induced fragmentation does neither require any phase change nor the crossing of metastability limits as in phase explosion. It differs from other photomechanical mechanisms, such as spallation and cavitation because it does not involve tensile stresses. Another intriguing feature in Figure 12 is the presence of significant amounts of nanoscale/sub- $\mu\text{m}$  particles near the lateral edges of the microchannels that are attributed to CE mechanism (see the next section for complete discussion). Figure 13 shows the scanning electron microscope (SEM) images of 120  $\mu\text{m}$  size micromotor-rotors processed at two pulse energies. The hole at the center is meant for assembling 25  $\mu\text{m}$  diameter shafts. It may be noted that higher pulse energy ablation ruined the rotor structure by thermal damage, while the lower pulse energy ablation produced a reasonably well-defined profile with improved resolution, little contamination and minimal thermal damage.

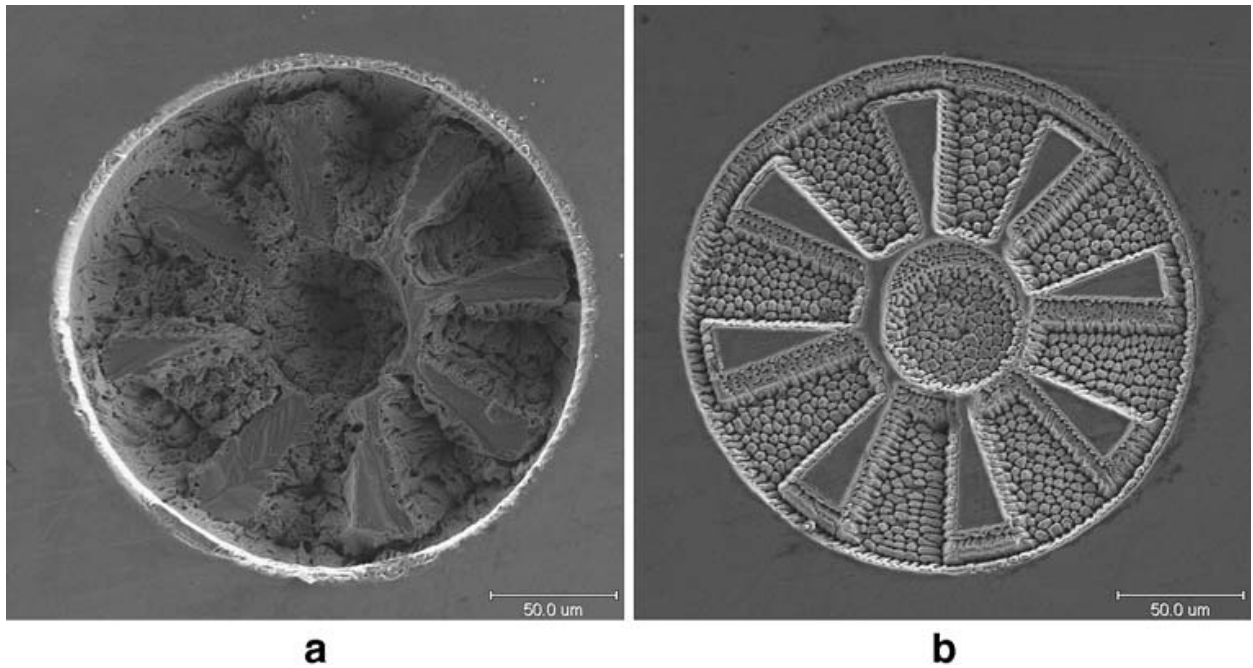


**Figure 13. Femtosecond laser micromachined rotor in 3C-SiC thin films deposited on silicon (a) 60  $\mu\text{J}$ ; (b) 8  $\mu\text{J}$**

There is no evidence of typical thermal damages, such as recast layer, ripple, column and crack. Instead, a large number of loose fragments and tiny holes were noted in the center section of rotor (Figure 14) probably caused by photomechanical fragmentation and vaporization respectively.

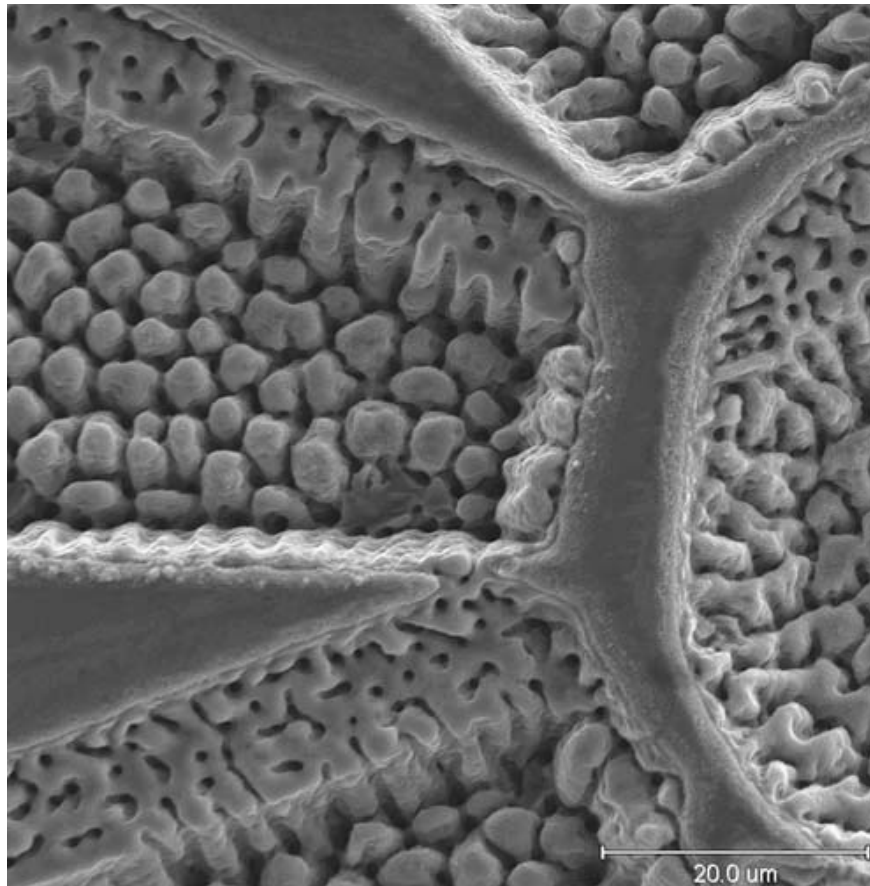


**Figure 14. High-magnification views of the center section of rotor displayed on Figure 6 (b)**

Figure 15 shows an SEM micrograph of a salient-pole micromotor with stator and rotor having a gap of  $2\ \mu\text{m}$  between them. KOH etchant was used to remove the loose fragments and release the rotor part. Caution must be exercised during the etching process because the central portion (shaft) may also be etched out as it is much smaller in area than each arm of the rotor. Very low energy ablation When the pulse energy was further reduced to less than  $1.5\ \mu\text{J}$ , the ablation mechanisms appears to be exclusively of Coulomb explosion and photomechanical fragmentation. Figure 16 and Figure 17 are the SEM images showing the effects of very low energy on the channel profiles. There is also evidence of the formation of nanoparticles on the sidewalls of etched profile. Figure 18 is a rotor fabricated using  $1.2\ \mu\text{J}$

that shows much improved resolution and accuracy over the one fabricated at  $8 \mu\text{J}$  (Figure 13 (b)).

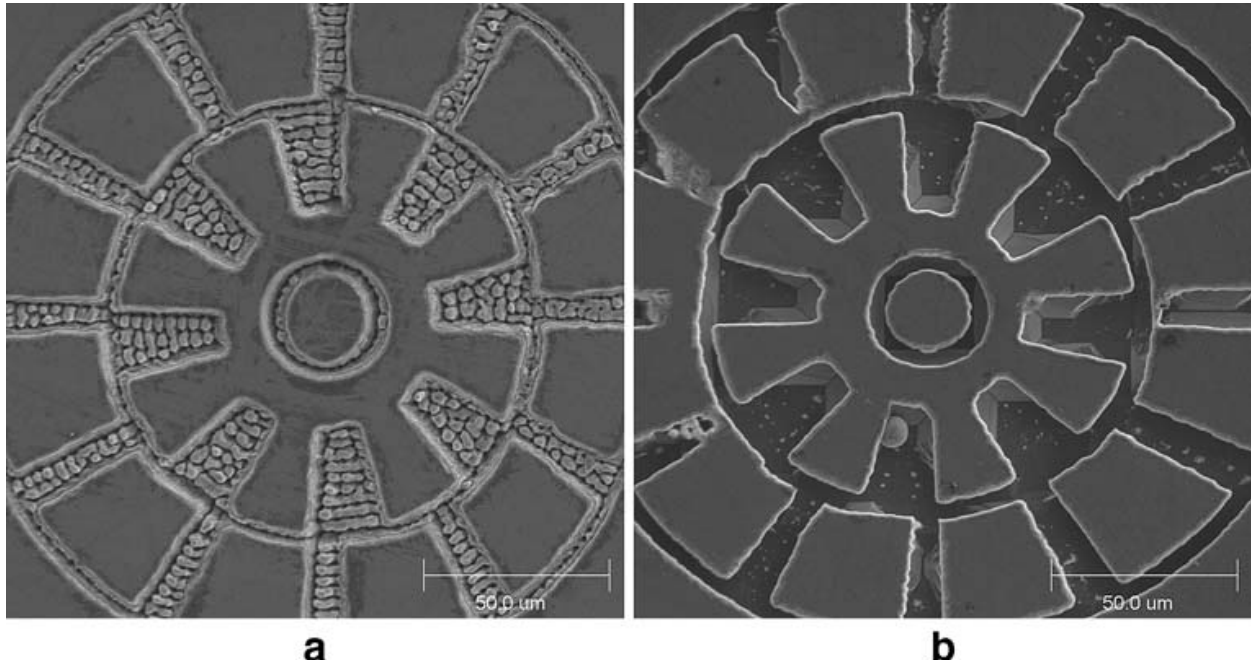


**Figure 15. Femtosecond laser micromachined microrotor in 3C-SiC thin films deposited on silicon (a) after laser ablation (b) after subsequent etching in Koh**

Actually the size of this rotor is even smaller than the one shown in Figure 13 (b), inferring that low-energy processing is appropriate for fine structures with high resolution. We contemplate Coulomb explosion (CE) as a possible mechanism for material removal in this regime because of the following characteristics: 1) time-of-flight analysis showed that the ions move at faster rate than in thermal vaporization; 2) etch rate is on the order of nanometer per pulse; 3) ablated surface contains a high density of nanoparticles. CE involves charge localization unlike phase explosion. Due to the capability of femtosecond laser in dumping large amounts of energy in short time, the laser pulse will excite the electrons through multiphoton and impact ionizations and emit the electrons from the surface and underlying regions, inducing strong ionization and leaving a high concentration of uncompensated ions.

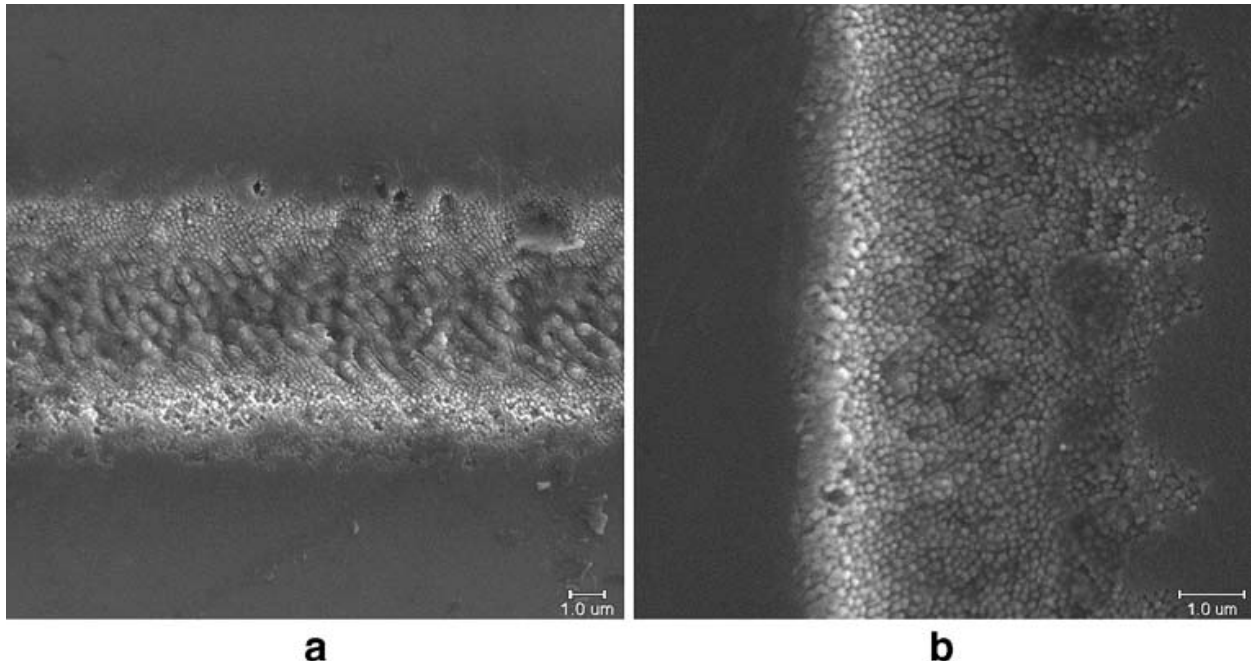


**Figure 16. Femtosecond laser micromachined channel at pulse energy of 1.2. Note the formation of 50-100 nm diameter nanoparticles at the edge (a) microchannel (b) edge of microchannel**

Essentially, the femtosecond laser creates a track of electron-hole pair excitations with a charge imbalance (because the mobility of holes is much smaller than that of the electrons). Hence the surface becomes electrostatically unstable and electric field is generated. If the electric field strength exceeds that of the binding energy of atoms in the target, CE takes place. Inherently a nonthermal process, CE dominates at low pulse energy and usually removes a small fraction of the mass.

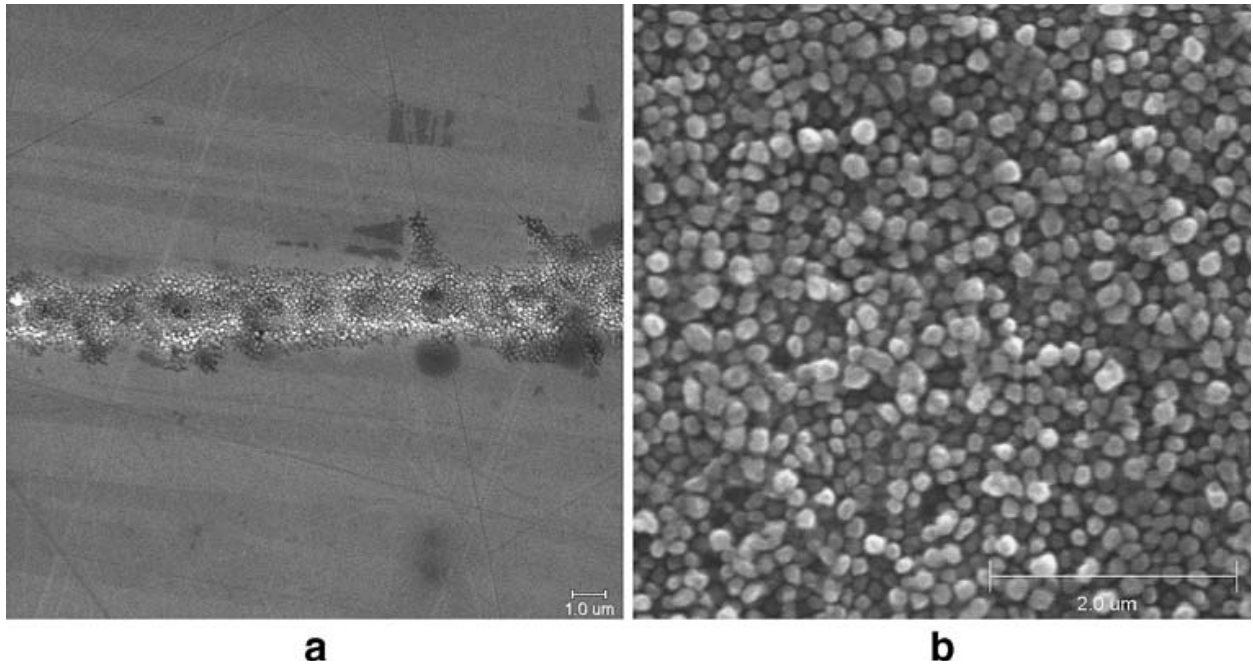


**Figure 17. Femtosecond laser micromachined channel at a pulse energy of 0.06 (a) microchannel (b) structures within the microchannel**

CE has been experimentally proven to occur in aluminum oxide dielectrics under femtosecond laser irradiation with 800-nm laser wavelength at laser fluences only slightly above the ablation threshold [21, 46, 47]. However, the applicability of CE in ultrafast laser ablation of semiconductors remains controversial. For example, the electron dynamics calculations of surface charging profiles of dielectric  $\text{Al}_2\text{O}_3$  (induced by 100-fs laser) provided a net surface charge (ni-ne) density of  $7 \times 10^{21} / \text{cm}^3$  in contrast to silicon where the net accumulated positive charges during the 100-fs laser pulse is 200 times lower [48].

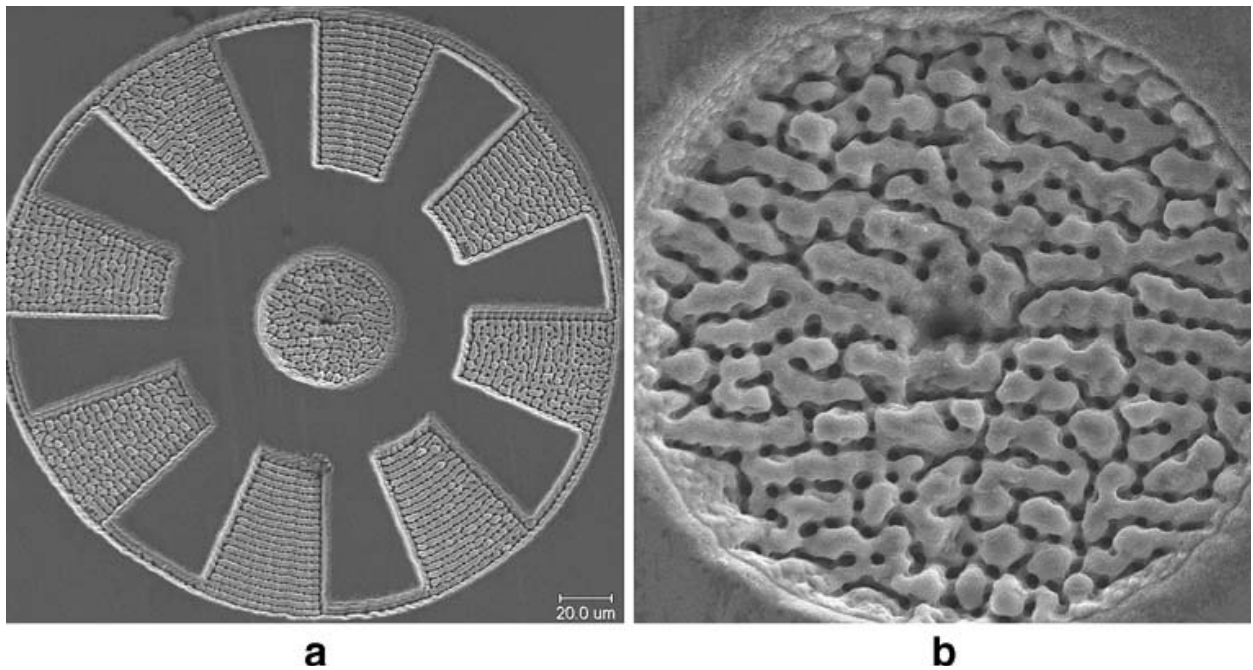


**Figure 18. Femtosecond laser micromachined rotor in 3C-SiC thin films deposited on silicon using a pulse energy of 1.2  $\mu\text{J}$  (a) Rotor; (b) Magnified view of central portion**

This difference was attributed to the higher electron mobility and higher density of available free electrons for semiconductors, causing effective screening. Stoian et al. [48] hypothesized that effective quenching of surface charging by bulk electrons do not permit CE to occur in semiconductors. However, recent experimental evidence suggests the occurrence of CE for Si (111) after 800-nm, fs-laser ablation at a higher energy fluence of 1.2 J/cm<sup>2</sup> because at lower fluences efficient electronic transport from the bulk counteracts the laser-induced charges [49]. Nanoparticle formation Figure 19 is a single-shot laser irradiated zone at very low pulse energy of 0.5  $\mu\text{J}$  showing the formation of nanoparticles. X-ray diffraction was used to characterize the crystalline structure and orientation while and Auger electron spectroscopy was used to identify the composition of nanoparticles. Figure 20 shows XRD patterns of both CVD and laser nanostructured 3C-SiC films exhibiting cubic (zinc-blende) structure. The (111), (200) and (400) reflection peaks are identified in the CVD deposited

3C-SiC thin films (Figure 20 a). However after laser nanostructuring, the ratio of intensity of (111) to (200) peaks was sharply reduced while the

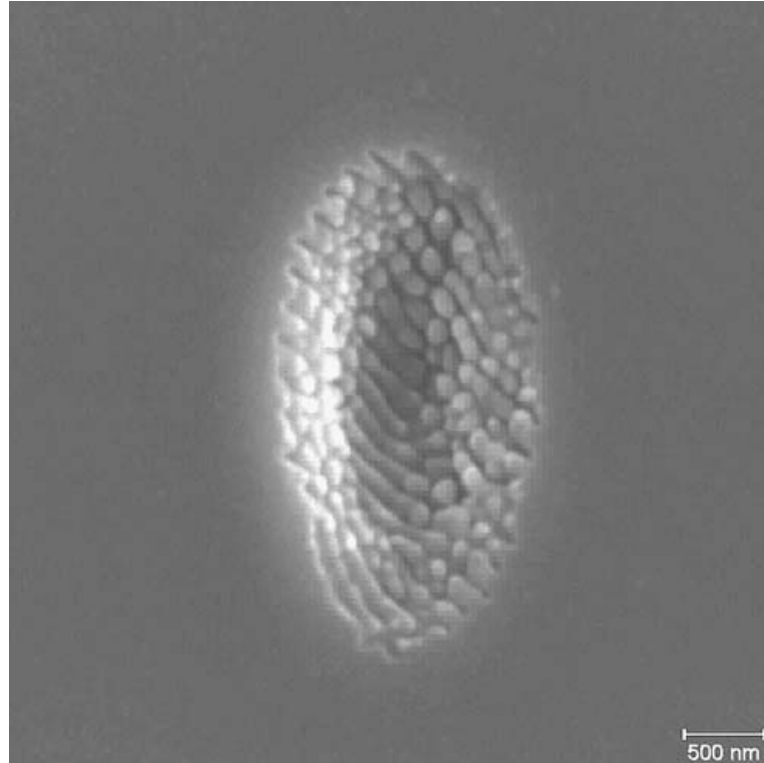


**Figure 19. Single-shot, femtosecond laser micromachined region in 3C-SiC thin films deposited on silicon (pulse energy = 0.5  $\mu$ J)**

FWHM of (200) became narrower. A strong preferred orientation along the  $\langle 100 \rangle$  direction was observed, indicating the more stable structure. The modification of crystalline orientation in nanoparticles is attributed to lattice arrangement resulted from increased lattice vibration due to lattice heating accompanying Coulomb explosion. Auger electron spectrometry (AES) was utilized to determine the CVD (un-irradiated) and nanoparticle (laser-irradiated) SiC films. Figure 21 shows the results. For the laser-irradiated film, an oxygen contamination was present, but it was rapidly reduced to trace amounts after 35 seconds of Ar ion etching. The CVD and post Ar-ion etched films were comparable in binding energy and intensity implying that the composition was unchanged. Nanostructuring

presented in this work has also been observed in ion sputtering of materials with highly charged ions at low impact energies [50, 51].

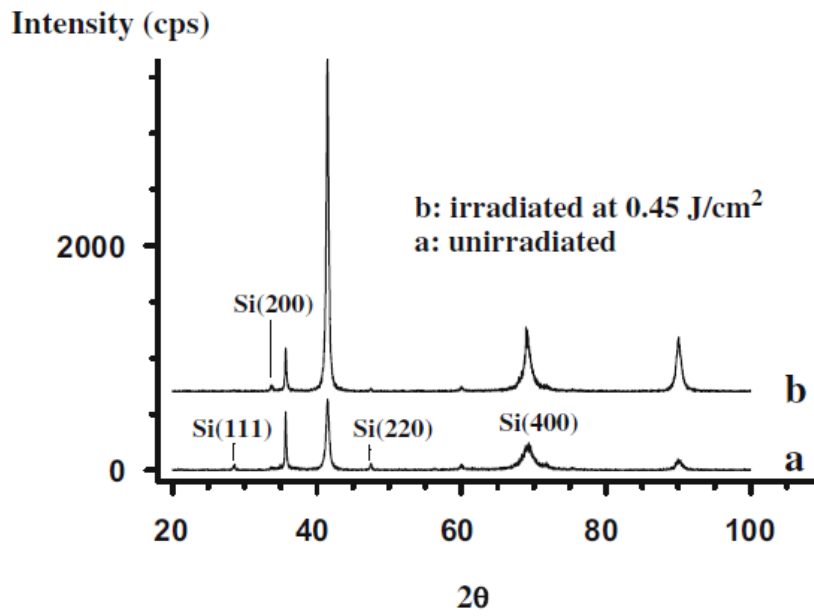


**Figure 20. X-ray diffraction spectra of 3C-SiC films of (a) CVD thin film and (b) Laser nanostructured thin film**

Molecular dynamics simulations of highly-charged-ion collisions on silicon surfaces have shown that CE accounts for the production of nanoscale structures and is in agreement with experimental findings [47]. Molecular simulations of ultrafast laser ablation of silicon at low fluences exhibit many similarities to the ion beam bombardment [52, 53]. The time scale for Coulomb explosion is found to be  $<1$  ps. For laser pulse durations longer than 1 ps, ion emission can still occur but thermal excitation of the lattice will cause a phase explosion mechanism, leading to large amount of material removal and nanoscale structuring will be destroyed.

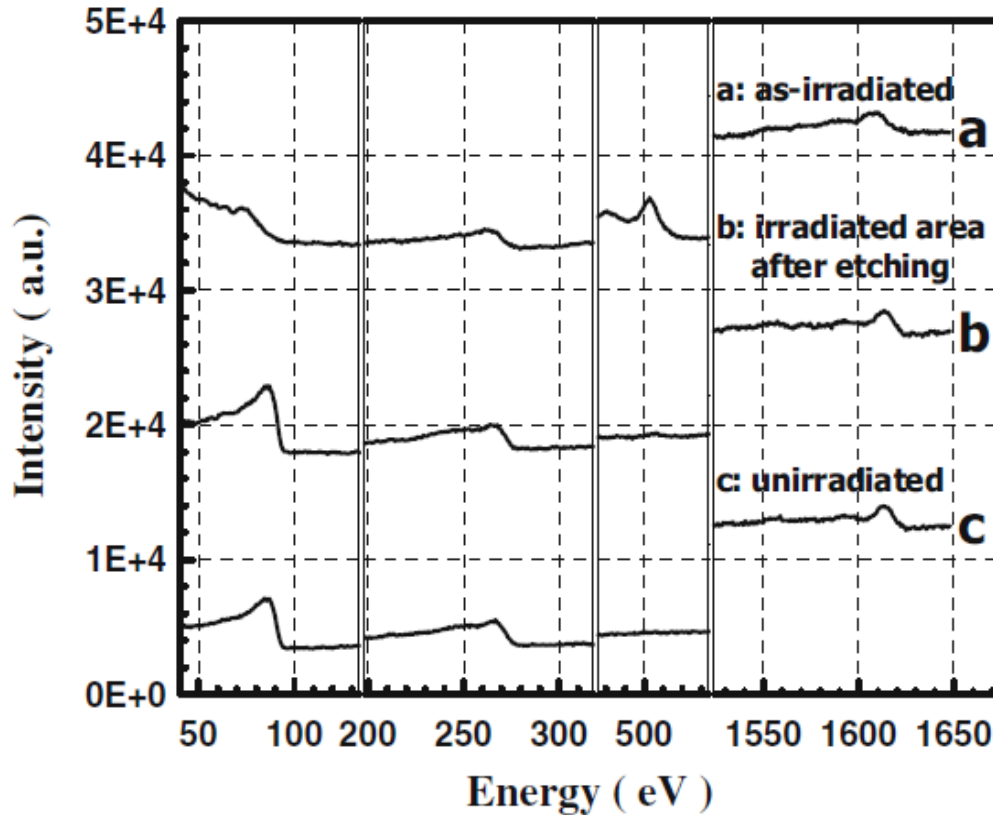


**Figure 21. Auger electron spectra of 3C-SiC films: (a) Laser-irradiated at 0.45 J cm<sup>2</sup>; (b) Laser irradiated and then Ar-ion etched; (c) Un-irradiated**

In contrast to the nanosecond laser pulses, ultrafast pulses have an advantage of not interacting with the plume of ablated material since the pulse has ceased prior to the laser damage. Consequently, plume heating and shock-wave mechanisms do not account for nanoparticle formation. Another possible mechanism of nanoparticle formation on the solid surfaces subjected to laser ablation is the interference phenomenon leading to spatial periodic structures, known as ripples (also known as laser-induced periodic surface structure, LIPSS); this is believed to produce nanoparticles and nanopatterns on the surfaces [54-57]. Ripples emanate when incident or reflected or refracted laser light interferes with the scattered light from defects, roughness, or some sort of surface disturbance. Laser polarization plays a key role in the formation of ripple structure. Although the spacing between fringes is equal to the

wavelength, recent experiments proved that the periods are substantially shorter than the wavelengths, leading to development of nanostructures in materials like TiN, InP, GaP and GaAs. The process begins with production of surface relief with shallow depressions and elevations and then continues with the formation of periodic nanochannels if linear polarization were used and the formation of self-organized array of nanoparticles if circular polarization were applied. Recent work showed the nanosecond pulsed 248-nm laser irradiation of Si at  $<1 \text{ J/cm}^2$  using a background of ultra-high pure helium generated the formation of nanoparticles in the form of linear arrays or strings depending on the type of polarization [57]. It is interesting to note the formation of such nanoparticles despite the use of high-energy fluence and long pulse, both of which tend to produce plasma and suppress the interference effects. Since these nanoparticles were created with a background of ultra-high pure helium, it could be an effect ascribed to gas phase condensation. Effect of assist gases Experimental works that involve laser beam interaction with its propagation medium have shown the defocusing effects when the propagation medium (gas) is ionized by the leading edge of the beam [24, 25]. Researchers investigating femtosecond laser micromachining have emphasized the use of an inert gas to prevent the harmful effects of defocusing [12-14]. Micromachining of holes in copper showed that helium was a better gas medium for beam propagation than air, neon, and nitrogen. Use of helium as an assist gas resulted in improved sidewall quality, lower debris redeposition, and minimal thermal damage [14]. Similar studies on the effects of laser micro-structuring of trenches in aluminum revealed that helium markedly improved the quality as compared to ambient atmosphere [12], argon and nitrogen [13]. The exact mechanism by which helium prevents the redeposition of debris is not fully understood; however, it has been suggested that the

recoil pressure caused by the hot plasma prevents debris from leaving the ablated area [14]. For nearinfrared femtosecond pulses, use of helium as an assist gas for aluminum is more effective at lower fluences [12]. When the energy fluence was reduced to near threshold, nanometer-sized aluminum single crystal spheres were formed and carried away by the assist gas [12]. In the present work, ultrafast laser interactions with 3CSiC were evaluated with the aid of helium as an assist gas and compared to those of ambient atmosphere. At low pulse energy of 0.2  $\mu\text{J}$  the formation of nanoparticles within the irradiated area has occurred; this was independent of the type of assist gas being ambient or helium assist gas. The implication is that the formation of nanoparticles at low fluence is not caused by oxidation. In low pulse energy regime that corresponds to a fluence much lower than the ionization fluence of air, the assist gases did not play a significant role. This was in agreement with the previous work [14]. However it was found at higher pulse energies, where thermal effects were significant, that the use of helium showed significant improvement in quality such as minimal recast layer over ambient atmospheric conditions.

#### 4.5. Conclusions

Ultrafast laser micromachining of CVD-deposited single crystalline 3C-SiC thin film on silicon substrate was investigated as a function of pulse energy for the purpose of determining the optimum pulse energy for the fabrication of MEMS devices. The results were correlated with the underlying physical mechanisms. Higher pulse energies generated significant amount of recast layer and damaged fragments while lower pulse energies ( $<0.5 \mu\text{J}$ ) are not sufficient to ablate the material to the desired depth. High resolution, damage-free features were produced at low pulse energy (1–10  $\mu\text{J}$ ). This study demonstrates that the

femtosecond pulsed laser ablation has excellent potential for SiC micromachining and has a superior edge over traditional reactive ion etching and electrochemical etching methods.

## Acknowledgements

The authors would like to acknowledge the National Science Foundation (NSF) for supporting this research work under the grant DMI-0619115. Thanks are also due to Dr. Chris Zorman of Case Western Reserve University for providing CVD deposited thin film wafers.

## References

1. *Silicon carbide electronic materials and devices*. Materials Research Society Bulletin, 1997. **23**(3): p. 19-56.
2. Müller, G. and Krötz, *SiC for sensors and high-temperature electronics*. Sensors and Actuators A, 1994. **43**(1-3): p. 259-268.
3. Okojie, R.S., et al., *Characteristics of a hermetic 6H-SiC Pressure Sensor at 600°C*, in *AIAA Space 2001 Conference and Exposition*. 2001: Albuquerque, NM, USA. p. 1-8.
4. Mehregany, M. and C.A. Zorman, *SiC MEMS: opportunities and challenges for applications in harsh environments*. Thin Solid Films, 1999. **355-356**: p. 518-524.
5. Dong, Y., C.A. Zorman, and P. Molian, *Femtosecond pulsed laser micromachining of single crystalline 3C-SiC structures based on a laser-induced defect-activation process*. Journal of Micromechanical Microengineering, 2003. **13**: p. 680-685.

6. Chichkov, B.N., et al., *Femtosecond, picosecond and nanosecond laser ablation of solids*. Applied Physics A, 1996. **63**(2): p. 109-115.
7. Ozono, K., et al., *High-speed ablation etching of GaN semiconductor using femtosecond laser*. Optica, 2001. **189**(1-3): p. 103-106.
8. Bonse, J., et al., *Femtosecond pulse laser processing of TiN on silicon*. Applied Surface Science, 2000. **154-155**: p. 659-663.
9. Liu, X., D. Du, and G. Mourou, *Laser Ablation and Micromachining with Ultrashort Laser Pulses*. IEEE Journal of Quantum Electronics, 1997. **33**(10): p. 1706-1716.
10. Ameer-Beg, S., et al., *Femtosecond laser microstructuring of materials*. Applied Surface Science, 1998. **127-129**: p. 875-880.
11. Perrie, W., et al., *Femtosecond laser micro-structuring of alumina ceramic*. Applied Surface Science, 2005. **248**(1-4): p. 213-217.
12. Perrie, W., et al., *Femtosecond laser micro-structuring of aluminum under helium*. Applied Surface Science, 2004. **230**(1-4): p. 50-59.
13. Robinson, G.M. and M.J. Jackson, *Femtosecond laser micromachining of aluminum surfaces under controlled gas atmospheres*. Journal of Materials Engineering and Performance, 2005. **15**(2): p. 155-159.
14. Sun, J. and J.P. Longtin, *Inert gas beam delivery for ultrafast laser micromachining at ambient pressure*. Journal of Applied Physics, 2001. **89**(12): p. 8219-8224.
15. Zoppel, S., et al., *Laser micro machining of 3C-SiC single crystals*. Microelectronic Engineering, 2006. **83**: p. 1400-1402.
16. Aoki, N., et al. *Micromachining of SiC by Femtosecond Ablation*. in *Conference on Lasers and Electro-Optics, 2001, CLEO/Pacific Rim*. 2001.

17. Zorman, C.A., et al., *Deposition of 3C-SiC films on 100 mm diameter Si(100) wafers in large-volume LPCVD furnaces*. *Electrochemical and solid-state letters*, 2002. **5**(10): p. G99-G101.
18. Zhang, J., et al., *Direct photoetching of single crystal SiC by VUV-266 nm multiwavelength laser ablation* *Applied Physics A: Materials Science & Processing*, 1997. **64**: p. 367-371.
19. Pearton, S.J., *Wet and dry etching of SiC*, in *Process technology for silicon carbide devices*  
C.-M. Zetterling, Editor. 2002, INSPEC: London, UK.
20. Gudde, J. and J. Hohlfeld, *Damage threshold dependence on electron-phonon coupling in Au and Ni films*. *Applied Surface Science*, 1998. **127-129**: p. 40-45.
21. Bulgakova, N.M., et al., *Theoretical Models and Qualitative Interpretations of Fs Laser Material Processing*. *JLMN-Journal of Laser Micro/Nanoengineering*, 2007. **2**(1): p. 76-86.
22. von der Linde, D. and H. Schüler, *Breakdown threshold and plasma formation in femtosecond laser-solid interaction*. *Journal of the Optical Society of America B: Optical Physics*, 1996. **13**(1): p. 216-222.
23. Wu, A.W., I.H. Chowdhury, and X. Xianfan, *Plasma formation in fused silica induced by loosely focused femtosecond laser pulse*. *Applied Physics Letters*, 2006. **88**(11): p. 111502.
24. Auguste, T., et al., *Defocusing effects of a picosecond terawatt laser pulse in an underdense plasma*. *Optics Communications*, 1992. **89**(2-4): p. 145-148.

25. Rae, S.C., *Ionization-induced defocusing of intense laser pulses in high-pressure gases*. Optics Communications, 1993. **97**(1-2): p. 25-28.
26. Gibbon, P., *Short Pulse Laser Interactions with Matter: An Introduction*. 2005, London, UK: Imperial College Press. 328.
27. Perez, D. and L.J. Lewis, *Ablation of Solids under Femtosecond Laser Pulses*. Physical Review Letters, 2002. **89**(25): p. 111502-111506.
28. Shank, C.V., R. Yen, and C. Hirilimann, *Femtosecond-Time-Resolved Surface Structural Dynamics of Optically Excited Silicon*. Physical Review Letters, 1983. **51**(10): p. 900-902.
29. Rouse, A., et al., *Non-thermal melting in semiconductors measured at femtosecond resolution*. Nature, 2000. **410**: p. 65-68.
30. Stampfli, P. and K.H. Bennemann, *Time dependence of the laser-induced femtosecond lattice instability of Si and GaAs: Role of longitudinal optical distortions*. Physical Review B, 1994. **49**(11): p. 7299 - 7305.
31. Kelly, R. and A. Miotello, *On the mechanisms of target modification by ion beams and laser pulses*. Nuclear Instruments and Methods in Physics Research Section B, 1997. **122**: p. 374-400.
32. Bulgakova, N.M. and I.M. Bourakov, *Phase explosion under ultrashort pulsed laser ablation: modeling with analysis of metastable state of melt*. Applied Surface Science, 2002. **197-198**: p. 40-45.
33. Sokolowskie-Tinten, K., et al., *Transient States of Matter during Short Pulse Laser Ablation*. Physical Review Letters, 1998. **81**: p. 224-227.

34. Loranzo, P., L.J. Lewis, and M. Meunier, *Thermodynamic pathways to melting, ablation, and solidification in absorbing solids under pulsed laser irradiation*. Physical Review B, 2006. **73**: p. 134108-134130.
35. Miotello, A. and R. Kelly, *Laser-induced phase explosion: new physical problems when a condensed phase approaches the thermodynamically critical temperature*. Applied Physics A, 1999. **69**(7): p. 67-73.
36. Stoian, R., D. Ashkenasi, and E. Campbell, *Coulomb explosion in ultrashort pulsed laser ablation of Al<sub>2</sub>O<sub>3</sub>*. Physical Review B, 2000. **62**(19): p. 13167-13172.
37. Henyk, M., F. Costache, and J. Reif, *Femtosecond laser ablation from sodium chloride and barium fluoride*. Applied Surface Science, 2002. **186**(1-4): p. 381-384.
38. Tamura, H., et al., *Femtosecond laser-induced spallation in aluminum*. Journal of Applied Physics, 2001. **89**(6): p. 3520-3522.
39. Nakata, Y., T. Okada, and M. Maeda, *Nano-Sized Hollow Bump Array Generated by Single Femtosecond Laser Pulse*. Japanese Journal of Applied Physics, 2003. **42**: p. L1452-L1454.
40. Korte, F., J. Koch, and B.N. Chichkov, *Formation of microbumps and nanojets on gold targets by femtosecond pulses*. Applied Physics A, 2004. **79**(4-6): p. 879-881.
41. Meshcheryakov, Y.P. and N.M. Bulgakova, *Thermoelastic modeling of microbump and nanojet formation on nanosize gold films under femtosecond laser irradiation*. Applied Physics A, 2006. **82**(2): p. 363-368.
42. Eliezer, S., et al., *Synthesis of nanoparticles with femtosecond pulses*. Physical Review B, 2004. **69**(14): p. 144119.

43. Bulgakova, N.M. and A.V. Bulgakova, *Pulsed laser ablation of solids: transition from normal vaporization to phase explosion*. Applied Physics A, 2001. **73**(2): p. 199-208.
44. Von der Linde, D. and K. Sokolowski-Tinten, *The physical mechanisms of short-pulse laser ablation*. Applied Surface Science, 2000. **154-155**(1-4): p. 1-10.
45. Song, K.H. and X. Xianfan, *Explosive phase transformation in excimer laser ablation*. Applied Surface Science, 1998. **127-129**: p. 111-116.
46. Henyk, M., D. Wolframm, and J. Reif, *Ultra short laser pulse induced charged particle emission from wide bandgap crystals*. Applied Surface Science, 2000. **168**(1-4): p. 263-266.
47. Cheng, H. and J. Grillaspy, *Nanoscale modification of silicon surfaces via Coulomb explosion*. Physical Review B, 1997. **55**(4): p. 2628-2636.
48. Stoian, R., et al., *Surface charging and impulsive ion ejection during ultrashort pulsed laser ablation*. Physical Review Letters, 2002. **88**(9): p. 097603.1-097603.4.
49. Roeterdink, W., et al., *Coulomb explosion in femtosecond laser ablation of Si(111)*. Applied Physics Letters, 2003. **82**(23): p. 4190-4192.
50. Schneider, D. and M. Briere, *Investigations of interactions of highest charge state ions with surfaces*. Physica Scripta, 1996. **53**: p. 228-242.
51. Itabashi, N., et al., *Desorption of Ga and As atoms from GaAs surface induced by slow multiply charged Ar ions*. Japanese Journal of Applied Physics, 1995. **34**(12B): p. 6861.
52. Herrmann, R.F.W., J. Gerlach, and E. Campbell, *Ultrashort laser ablation of silicon: an MD simulation study*. Applied Physics A, 1998. **66**(1): p. 35-42.

53. Herrmann, R.F.W., J. Gerlach, and E.E.B. Campbell, *Molecular dynamics simulation of laser ablation of silicon*. Nuclear Instruments and Methods in Physics Research Section B, 1997. **122**(3): p. 401-404.
54. Ozkan, A.M., et al., *Femtosecond laser-induced periodic structure writing on diamond crystals and microclusters*. Applied Physics Letters, 1999. **75**(23): p. 3716-3718.
55. Boroweic, A. and H.K. Haugen, *Subwavelength ripple formation on the surfaces of compound semiconductor irradiated with femtosecond laser pulses*. Applied Physics Letters, 2003. **82**(25): p. 4462-4464.
56. Yasumaru, N., K. Miyazaki, and J. Kiuchi, *Femtosecond-laser-induced nanostructure formed on hard thin films of TiN and DLC*. Applied Physics A, 2003. **76**: p. 983-985.
57. Pedraza, A., J. Fowlkes, and Y. Guan, *Surface nanostructuring of silicon*. Applied Physics A, 2003. **77**(2): p. 277-284.

## CHAPTER 5. RAPID PROTOTYPING OF BULK 6H-SiC MEMS STRUCTURES USING A Q-SWITCHED Nd:YAG LASER

A Paper Published in the North American Manufacturing Research Conference 37  
(NAMRC-37)  
Ben Pecholt and Pal Molian

### 5.1. Abstract

MEMS pressure diaphragm structures in square configuration (1 mm x 1 mm) were laser micromachined on 6H-SiC wafer using a 1064 nm wavelength, <100 ns FWHM Q-switched Nd:YAG laser operating with a 3 kHz repetition rate and an average power of less than 2 W. Structures were machined by scanning the beam at a rate of 1 mm s<sup>-1</sup> while varying the amount of overlap between 70 and 90%. The depth of material removal was experimentally determined and the laser parameters of average power (0.35 W) and beam overlap (85.8%) were optimized to produce high quality diaphragms suitable for MEMS pressure sensor application. Results were compared with an ultra-short pulsed laser in terms of material removal rate and feature quality. Machining rates of 17-860 μm min<sup>-1</sup> were achieved using the Nd:YAG laser. Additionally tiered structures were fabricated on the difficult-to-machine 6H-SiC, implying that Nd:YAG laser micromachining is capable of generating much more complex profiles than possible with conventional methods.

### 5.2. Introduction

Micro-Electro-Mechanical Systems (MEMS) have emerged from the microelectronics industry in 1980s, rapidly developed in 1990s and widely used in 2000s. Conventional microfabrication techniques initially led to silicon-based MEMS devices;

however, MEMS technology is now maturing to new areas of development that are well beyond the capabilities of silicon. Silicon carbide (SiC) is one such material that is highly desirable for high-temperature and harsh environments due to its excellent mechanical, thermal, chemical and electrical properties. SiC has become a favorable material among similar hard materials such as diamond and silicon nitride due to its attractive electronic properties and success in thin film deposition technology. Today silicon carbide is commercially available in bulk, single crystalline wafer forms as 4H-SiC, 6H-SiC.

Unlike silicon, crystalline SiC is inert to chemical attack and suffers from slow etch rates, less than  $2 \mu\text{m min}^{-1}$  [1], even in Deep Reactive Ion Etching (DRIE). Pulsed Nd:YAG lasers have been shown to be capable of removing thin layers from  $\text{Si}_3\text{N}_4$  using a galvo scanner [2]. IR lasers have already been demonstrated to machine 4H-SiC at higher etch rates on the order of hundreds of  $\mu\text{m min}^{-1}$  in drilling applications [3]. However, a trade off exists between the parallel nature of plasma etching operations and the serial method of direct-write laser machining.

Table 1 lists the optical characteristics of crystalline SiC for different lasers. The high optical absorptivity for UV wavelength lasers results in the majority of photons being absorbed within the first few nanometers of the surface. In the case of the  $1\omega$  and  $2\omega$  Nd:YAG lasers, light can transmit into the material for millimeters. Consequently UV lasers exhibit a relatively low ablation rate, which has been reported in the range of 10-60 nm/pulse [4-6]. In contrast, 1060 nm IR lasers can generate much higher ablation rates, on the order of 470-1800 nm/pulse [3]. Compounding the difference between the UV and IR lasers is the fact that the typical excimer laser has a maximum repetition rate on the order of hundreds of

pulses per second while Q-switched solid state lasers such as the Nd:YAG can achieve tens of thousands of pulses per second, dramatically reducing the processing time.

Using laser as a tool for structuring MEMS devices has recently gained momentum due to the availability of ultra-short pulses (picoseconds and femtoseconds) that resulted in minimal thermal damages and offered the ability to machine most materials irrespective of their optical properties. Ultra-short pulse systems, however, are expensive and can be difficult to operate and maintain whereas solid state Nd:YAG lasers are well established and industrially proven with a status as a mature technology.

Only few studies have been reported on the direct laser patterning of SiC with nanosecond pulses and that too are limited to amorphous [7] and polycrystalline [8] forms. Desbiens and Massons were able to machine a diaphragm structure 400 x 400  $\mu\text{m}$  wide approximately 200  $\mu\text{m}$  deep on amorphous SiC by scanning a pulsed excimer beam over the sample surface [7]. Kreutz *et al.* were able to machine complex 3D structures including a semi-spherical depression on polycrystalline SiC using a Q-switched Nd:YAG laser [8] system with a metrology tool of autofocus vision system for *in situ* depth measurement. To the authors' knowledge, there has been no demonstration todate of a nanosecond Q-switched Nd:YAG micromachining (excluding via hole formation) of bulk single crystalline silicon carbide.

The absence of reliable data on optical absorption of single crystalline SiC polytypes has led to the emergence of discrepancies in the literature. For example Tian and Salama reported that 1064 nm wavelength laser pulses went through a bulk 6H-SiC without damage [9] while Anderson and co-workers were able to machine deep via hole structures in 4H-SiC using similar wavelengths [10, 11]. These conflicting reports may be resolved by considering the

differences in the surface composition of these samples. Tian and Salama used mostly pure wafers which were cleaned and stripped of native oxides prior to laser ablation, while Anderson was machining the substrate of High Electron Mobility Transistor (HEMT) structures which had an AlGaIn/GaN/SiC surface [10, 11]. The AlGaIn/GaN surface might have increased the optical absorption of the initial laser irradiation, improving the ability to machine the material.

**Table 10. Optical properties of silicon carbide with common lasers**

Laser Source	Wavelength, $\lambda$ (nm)	Photon Energy (eV)	Reflectivity, R		Absorption, $a^{-1}$ ( $\text{cm}^{-1}$ )		
ArF	193	6.42	0.4	Poly-Crystalline [12]	$1.65 \times 10^6$ <1000K	Poly-Crystalline [13]	
KrF	248	5.00	0.286	Poly-Crystalline [12]	$1.7 \times 10^6$ <1000K	Poly-Crystalline [13]	
XeCl	308	4.03	0.243	Poly-Crystalline [12]	$1.44 \times 10^6 \times$ $\exp(2.1 \times 10^{-4}T)$ <1000K	Poly-Crystalline [13]	
$2\omega$ Nd:YAG	532	2.33	0.21	6H-SiC [14]	< 10	6H-SiC [15]	
$1\omega$ Nd:YAG	1064	1.17	0.20	*	< 20	6H-SiC [15]	

\* Data not available

### 5.3. Experimental Details

The laser system used was a Q-switched < 100 ns FWHM Nd:YAG laser operating at 1064 nm and a repetition rate of 3 kHz. The laser system is capable of a repetition rate of 1-50 kHz and delivers up to 8 watts of power. A plano-convex lens with an effective focal length 65 mm was used to focus the 1.2 mm diameter beam to a spot size to 70  $\mu\text{m}$  (using estimate from [16]) on the surface of the wafer with the rough surface exposed to the laser beam. Research grade 6H-SiC wafers (250  $\mu\text{m}$  thick, 50 mm diameter) were obtained from Cree, Inc. with a Si-face surface on the polished side and a rough backside. The samples were cleaned with methanol prior to processing, but native oxides were not attempted to be

removed. The samples were mounted on a computer controlled XY table by LabMotion with an accuracy of 1  $\mu\text{m}$  and repeatability of 0.5  $\mu\text{m}$ . Experiments were carried out under laboratory atmospheric conditions with an Ar gas stream at a rate of 7 L s<sup>-1</sup>. Diaphragm structures were machined by direct writing a series of overlapping concentric square passes. Roughness measurements were made using a Dektak II surface profilometer system. Depth measurements for samples with a depth greater than 40  $\mu\text{m}$  were made using microminiature Differential Variable Reluctance Transducer (DVRT) from Microstrain, Inc. with a minimum resolution of 3  $\mu\text{m}$ . The sample was moved relative to the DVRT (shown in Figure 22) by using an XYZ table by Newmark Systems Inc. with a minimum resolution of 0.02  $\mu\text{m}$  and repeatability of 5  $\mu\text{m}$ . A probe with a 100  $\mu\text{m}$  radius tip was coupled to the DVRT to scan the sample surface. Measurements were made every 50  $\mu\text{m}$  to evaluate the topographical nature of the samples. Measurements of the ablation depth width were obtained using an optical microscope with a 40x magnification and a minimum scale resolution of 1.5  $\mu\text{m}$ .

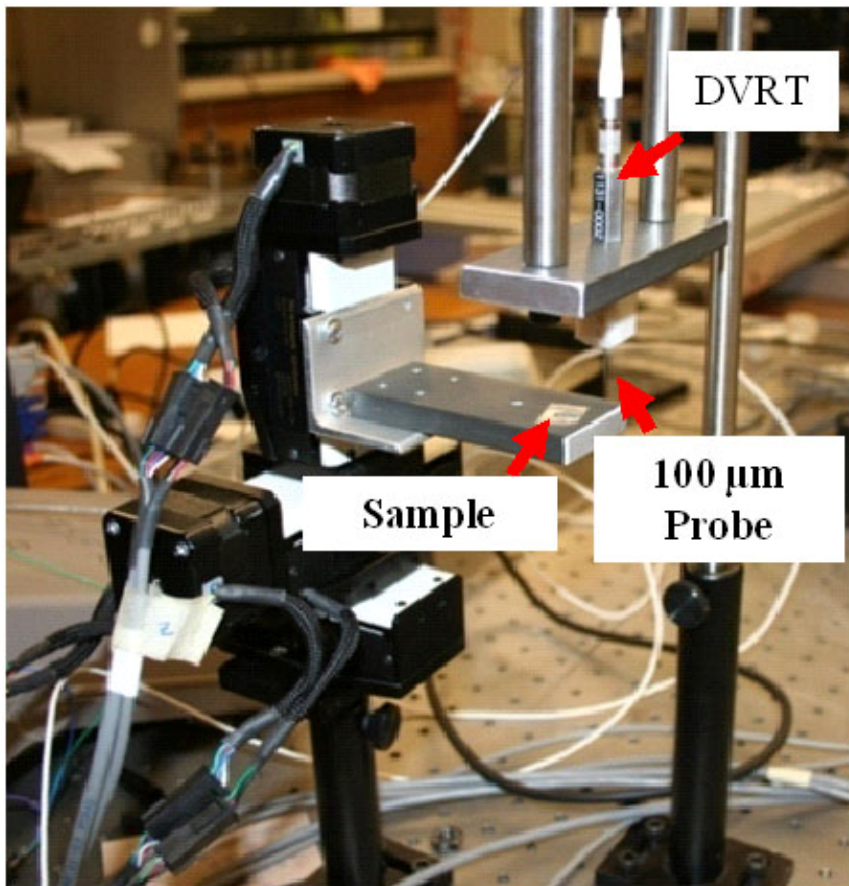


**Figure 22. XYZ microstepper and microminiature DVRT setup used to measure the profile depth of the machined regions**

#### **5.4. Results and Discussion**

In this study, laser ablation was conducted on the wafer's rough side (SiC face) with an Ra measured at approximately 500 nm. The results of this study where the laser ablated the irradiated surface contrast with the results of Salama, Tian and coworkers [9, 17, 18]. In their study the laser light was impinged on the smooth surface of the wafer, transmitted through the bulk and absorbed by the backside. Figure 2a is a schematic illustration of the finding that tracks did not appear on the polished side for an energy fluence of  $2.76 \text{ Jcm}^{-2}$

while scanning the beam over the rough side. However for the same energy fluence, when machining on the polished side, the beam intermittently transmitted through the wafer leaving a track on the backside as well as a track on the polished side.

A preliminary study of the ablation depth was performed as a function of energy density ranging from  $2.52 - 10.10 \text{ J cm}^{-2}$  at a scan rate of  $1 \text{ mm/s}$ . The results of these measurements can be seen in Figure 3. A low scan speed was selected for this study to minimize the effect of backlash in XY table when machining structures. The wafer was diced using a diamond-tipped scribing tool prior to laser machining and the depth of the zone damaged by the laser ablation was examined and measured using an optical microscope. It can be seen that the ablation depths are substantially higher than that achievable by the excimer laser which have an ablation rate of  $10\text{-}60 \text{ nm pulse}^{-1}$  [4-6].

The effects of machining parameters, degree of overlap and laser power density, were examined by machining a series of  $1 \times 1 \text{ mm}$  square diaphragms as indicated in Table 2. The rationale for square geometry over circular and rectangular geometries for the diaphragm is based on three reasons: ease of wafer dicing, symmetry of the geometry and wide usage in the pressure sensor industry. Diaphragms were machined using a sequential patterning technique whereby the laser beam spiraled inwards forming a series of concentric squares (Figure 4). It was experimentally found that this minimized the effects of backlash on our system and did not produce regions of excessive material removal forming through holes. Such holes occurred in regions where the XY stage had to stop and reverse direction as was found for a raster-scan technique. The beam was initiated at the periphery of the diaphragm and allowed to run without interruption by the shutter until reaching the center of the structure. This was determined to be the most effective method to minimize the harsh effects

of the giant pulse syndrome (GPS) sometimes found in Q-switched Nd:YAG systems due to instability in the oscillator when the attenuator is first turned off.

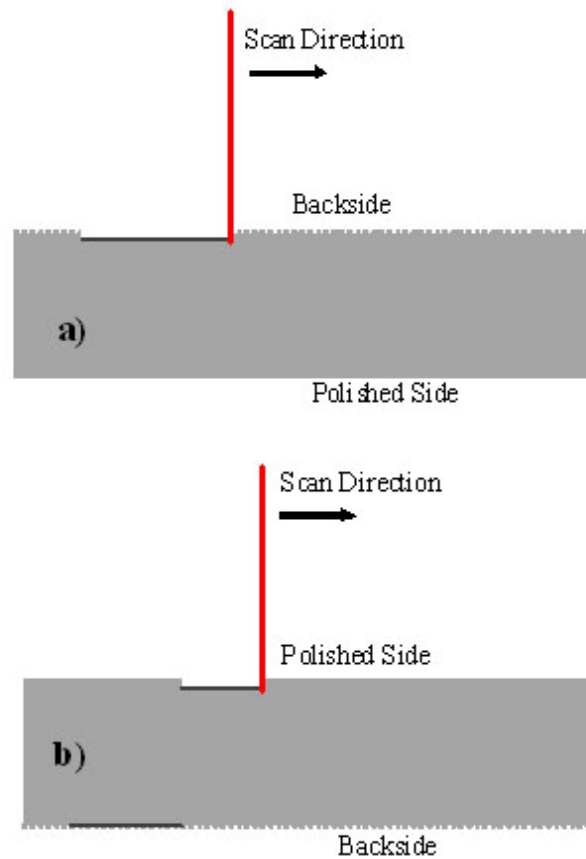


**Figure 23. Schematic of the laser processing a) laser micromachining of the rough side of the wafer b) laser micomachining of the polished side indicated intermittent transmittence.**

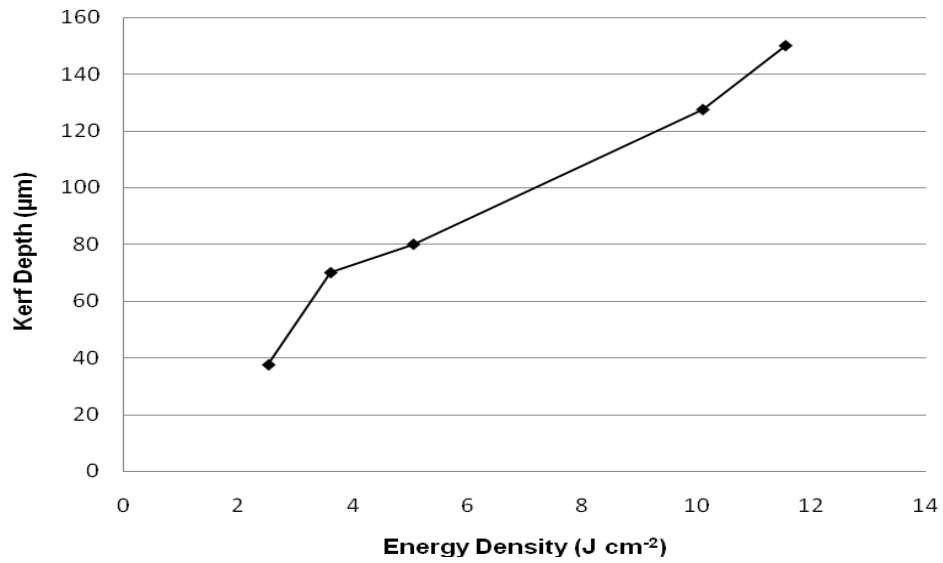


**Figure 24.** Ablation depth as a function of energy density for a single laser trace during scribing at a scan speed of  $1 \text{ mm s}^{-1}$ , 3 kHz machining on the backside

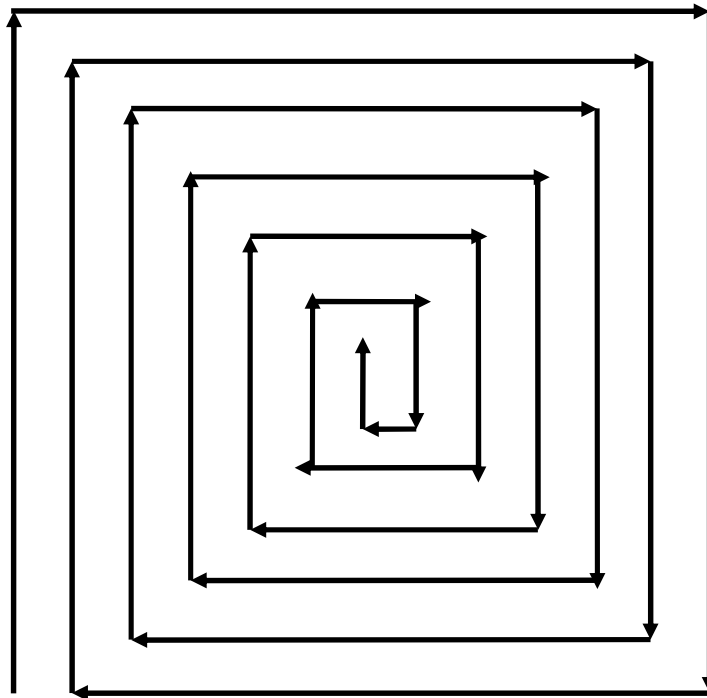


**Figure 25.** A pictorial representation of a single 'pass' made while laser machining with the XY table

Furthermore, the laser was initiated in different locations along the periphery when performing multiple passes to minimize these effects. Ninety degree turns were utilized to minimize the deceleration and acceleration of the XY table which otherwise contributes to the effects of deeper machining and damage to the localized area. The effect of the deceleration and acceleration around the 90 degree turns can be seen in Figure 5 represented by a diagonal pattern where the laser beam changed direction. The energy and number of passes (beyond two passes) did not significantly increase the machined depth of the sample. It was observed that after the machining a black surface layer covered the affected region and was not easily removable. Subjecting the samples to a five minute dip in HCl:H<sub>2</sub>O<sub>2</sub>:H<sub>2</sub>O (5:3:3) for five minutes followed by HF:HNO<sub>3</sub> for > 24 hours did not significantly reduce the black surface region.

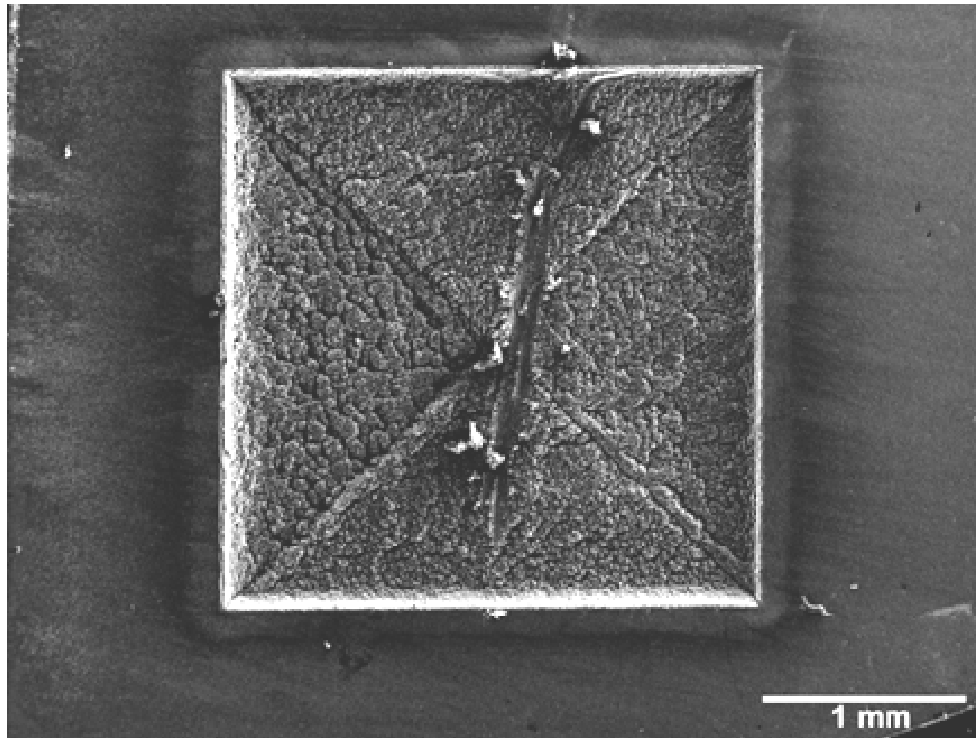


**Figure 26. Diaphragm structure immediately after laser micromachining with an intentional plough mark of the surface material**

However, the black material was easily ploughed by scraping a stainless steel tool over the surface as indicated in Figure 5. EDAX analysis of the black region showed silicon, oxygen and carbon, indicating the presence of oxides and carbides.

It was found that after 5 or more passes at a laser fluence of  $2.52 \text{ J cm}^{-2}$  with an overlap of 85.8%, the laser beam had partially machined through the sample rendering the diaphragm useless for pressure transducer applications.

Measurements using the surface profilometer indicated that the  $R_a$  roughness of the virgin surface of the rough side was approximately 500 nm and laser machining resulted in a smoother surface with the exception of the sample machined with multiple passes at an energy density above  $10.10 \text{ J cm}^{-2}$  and the sample with 71.6% overlap at  $2.52 \text{ J cm}^{-2}$  (see

Table 2). A tiered structure (Figure 6) was machined using  $3.61 \text{ J cm}^{-2}$  and 85.8% overlap. The profilometer data indicates that the roughness should be less than 250 nm.

**Table 11. Laser micromachining parameters and the resulting roughness and depth of removed material for a scan rate of  $1 \text{ mm s}^{-1}$ .**

Average Power (W)	$\text{W cm}^{-2}$	Energy/Pulse ( $\text{J pulse}^{-1}$ )	$\text{J cm}^{-2}$	Overlap ( $\mu\text{m}$ )	Overlap (%)	No. of Passes	Roughness Ra (nm)	Average Machined Depth ( $\mu\text{m}$ )	Depth Standard Deviation	Depth Removed Per Pass
0.35	9.01E+03	1.17E-04	2.52	10	85.8%	4	274	161	16	40
0.35	9.01E+03	1.17E-04	2.52	10	85.8%	4	-	160	19	40
0.35	9.01E+03	1.17E-04	2.52	10	85.8%	5	-	*	-	-
0.35	9.01E+03	1.17E-04	2.52	20	71.6%	4	7536	100	11	25
0.35	9.01E+03	1.17E-04	2.52	2	97.2%	1	12	35	-	35
0.35	9.01E+03	1.17E-04	2.52	4	94.3%	1	30	27	-	27
0.35	9.01E+03	1.17E-04	2.52	6	91.5%	1	34	20	-	20
0.35	9.01E+03	1.17E-04	2.52	8	88.6%	1	35	25	-	25
0.5	1.29E+04	1.67E-04	3.61	10	85.8%	3	226	†142	40	47
0.7	1.80E+04	2.33E-04	5.05	20	71.6%	2	253	81	16	41
0.7	1.80E+04	2.33E-04	5.05	10	85.8%	3	-	114	86	38
1.4	3.61E+04	4.67E-04	10.10	10	85.8%	1	1615	-	-	-
1.4	3.61E+04	4.67E-04	10.10	10	85.8%	2	578	86	17	43

† Error in program when machining

\* indicates that the laser machining partially broke through

- not measured

At this point is unclear whether or not the dark regions of the laser machined samples represent damage to the crystal structure and compromise the mechanical integrity of the MEMS diaphragm. Cleaning the samples in  $\text{HCl:H}_2\text{O}_2:\text{H}_2\text{O}$  for 5 minutes helped reduce debris immediately surrounding the affected area which is in agreement with other sources [19]. Edmond et al. reported that  $\text{HF:HNO}_3$  (1:1) was capable of etching ion implanted amorphous silicon carbide at a rate of  $100 \text{ nm min}^{-1}$  [20]. However there did not appear to be a substantial removal of material in this study nor was there a reduction in the black surface layer that covered the affected region.

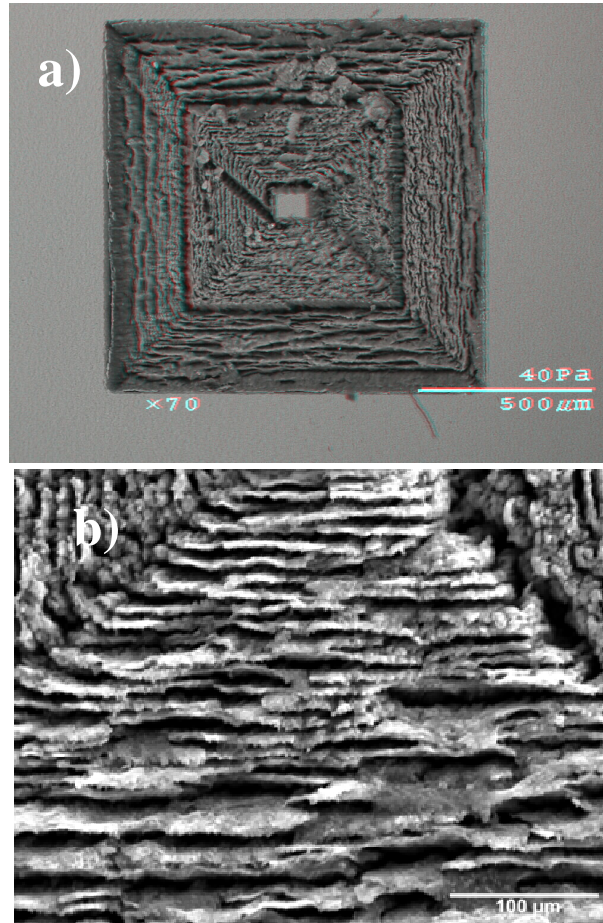


**Figure 27. Laser micromachined structure with three tier levels after chemical etching a) stereoscopic view b) closeup of the bottom structure**

The time required to fabricate a diaphragm is strongly influenced by the parameters of the degree of overlap, speed, and the overall size of the diaphragm. Figure 7 shows the effects of overlap and diaphragm size on the overall time required to complete a single ‘pass’ (Figure 4). For multiple passes, the estimate should be multiplied by quantity of passes to get the total time required to machine the diaphragm. The typical MEMS diaphragm is  $<1000 \mu\text{m}$  in size putting the machining time in the non-linear portion of Figure 28. The effect of overlap has a significant impact on machine time due to the increased overall distance traveled by the laser to complete a pass. The amount of area covered per second ( $\mu\text{m}^2 \text{s}^{-1}$ ) is

indicated in Figure 8 where it can be seen that there is little effect for any specific overlap for diaphragms greater than 500  $\mu\text{m}$  square. However, the time required to machine a diaphragm in this manner continues to increase as the area of the diaphragm increases; this suggests that the serial nature of this process is viable for small production and prototyping applications. Laser machining may remain inferior to the parallel processes for high volume production that can produce hundreds of devices at a time. Table 3 indicates the theoretical DRIE time based upon a maximum etch rate of 2  $\mu\text{m min}^{-1}$  compared the laser fabrication times for 0.5 x 0.5 mm and 1 x 1 mm diaphragms under various processing conditions.

Since ultra-short pulsed lasers are emerging as tools of future, a comparison of the results of this study was made with 1 W, 130-fs pulsed Ti:sapphire laser system (Quantronix, Integra C 150). Specifically material removal rate and feature quality were compared. For this purpose, circular diaphragms of 550  $\mu\text{m}$  diameter and 200  $\mu\text{m}$  depth were machined in 6H-SiC.

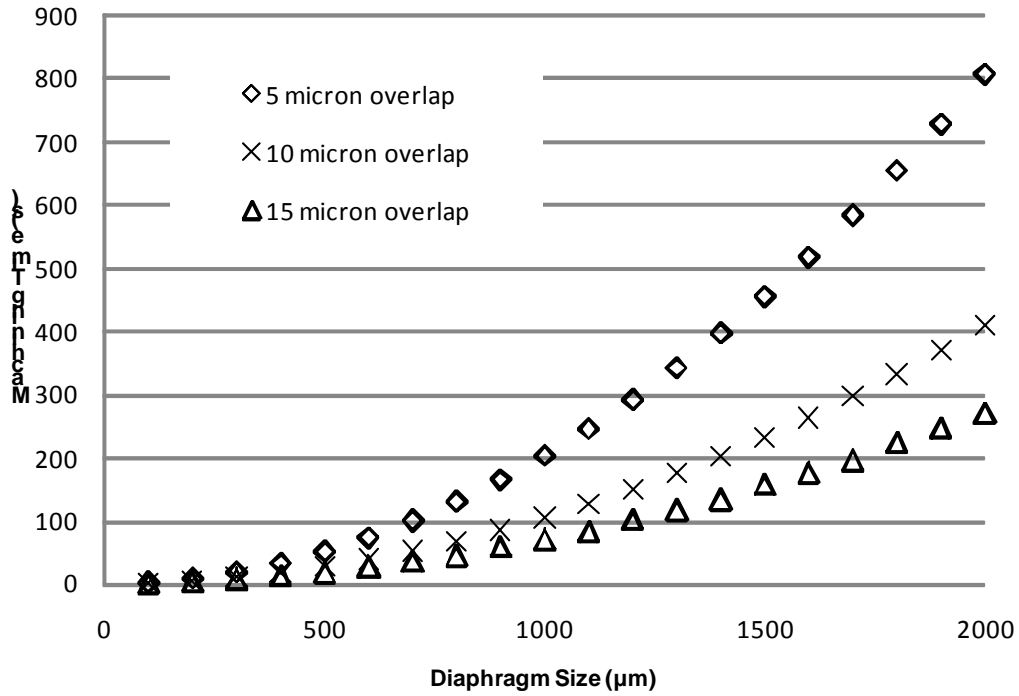


Figure 28. Effect of diaphragm size on the machining time

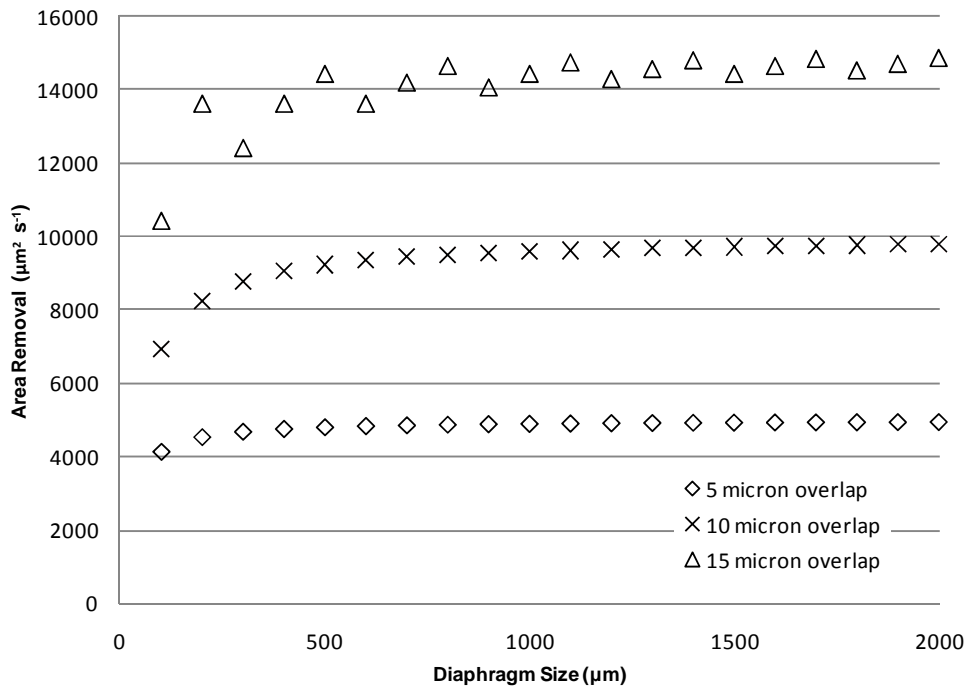


Figure 29. Effect of diaphragm size on the unit area covered per second

The material removal rate was  $3.27 \times 10^5 \mu\text{m}^3 \text{s}^{-1}$  which is much lower than that achieved with the Nd:YAG laser with an 85.8% overlap at  $2.52 \text{ J cm}^{-2}$ . Figure 9 shows the fs-laser machined profile where there is clean ablation of the material near the top surface. However the bottom of the machined region contains debris and exhibits a rough surface appearance. Ultra-short pulse ablation of silicon carbide near the ablation threshold is known to involve a non-thermal ablation process that removes material via Coulomb Explosion (CE) mechanism which allows for higher quality machining with little to no thermal damage, higher precision in material removal, however, it has lower material removal rates.

**Table 12. Laser micromachining parameters and the theoretical material removal rate for 0.5 x 0.5 mm and 1 x 1 mm square diaphragms**

Average Power (W)	$\text{J cm}^{-2}$	Overlap ( $\mu\text{m}$ )	Overlap (%)	No. of Passes	DRIE Etch Time (s) (assumed $2 \mu\text{m min}^{-1}$ etch rate)	0.5 x 0.5 mm			1 mm x 1mm		
						Time to Machine (s)	Etch Rate ( $\mu\text{m min}^{-1}$ )	Volumetric MRR ( $\mu\text{m}^3 \text{s}^{-1}$ )	Time to Machine (s)	Etch Rate ( $\mu\text{m min}^{-1}$ )	Volumetric MRR ( $\mu\text{m}^3 \text{s}^{-1}$ )
0.35	2.52	10	85.8	4	4816	108	89	3.71E+05	416	23	3.86E+05
0.35	2.52	10	85.8	4	4796	108	89	3.70E+05	416	23	3.84E+05
0.35	2.52	10	85.8	5	-	135	-	-	520	-	-
0.35	2.52	20	71.6	4	3007	54	111	4.63E+05	216	28	4.63E+05
0.35	2.52	2	97.2	1	1050	127	17	6.89E+04	504	4	6.94E+04
0.35	2.52	4	94.3	1	810	64	26	1.06E+05	254	6	1.06E+05
0.35	2.52	6	91.5	1	600	42	28	1.18E+05	169	7	1.18E+05
0.35	2.52	8	88.6	1	750	33	46	1.91E+05	127	12	1.97E+05
0.5	3.61	10	85.8	3	-	81	-	-	312	-	-
0.7	5.05	20	71.6	2	2431	27	180	7.49E+05	108	45	7.49E+05
0.7	5.05	10	85.8	3	3417	81	84	3.51E+05	312	22	3.65E+05
1.4	10.10	10	85.8	1	-	27	-	-	104	-	-
1.4	10.10	10	85.8	2	2586	54	96	3.98E+05	208	25	4.14E+05

Nanosecond pulse width lasers such as Nd:YAG and exhibit strong thermal ablation allowing for higher material removal rates. Femtosecond pulsed laser micromachining of 4H-SiC, 6H-SiC, and 3C-SiC [21] thin films have already been investigated for fabricating micromotors, resonators, microgrippers, etc, however the demands of industrial manufacturing for fast,

precise micromachining are better met by the robust, reliable, high repetition rate and high power nanosecond lasers.

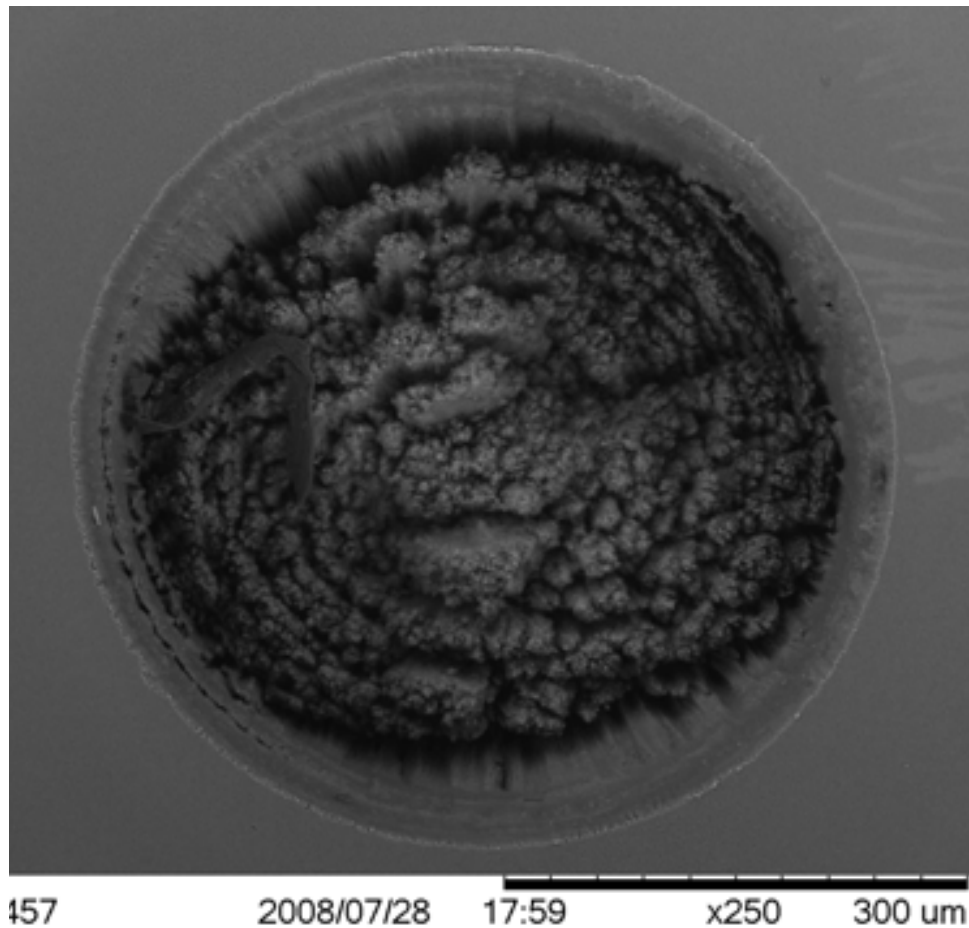


**Figure 30. Ultra-short pulse laser micromachined circular diaphragm with 500 μm diameter and 200 μm depth**

## 5.5. Conclusions

Nd:YAG laser micromachining is a viable method for removing bulk amounts of material from 6H-SiC and is superior than to conventional 6H-SiC machining methods for creating stepped geometry for prototyping and small batch production. Laser micromachining by itself is inferior to DRIE for parallel production, and machined surface

quality. Etch rates of  $17\text{-}860\ \mu\text{m min}^{-1}$  were achieved with overall machining time on the order of 10-50 times faster than that of DRIE were achieved. Nd:YAG lasers suffer from a poor surface quality, require lots of forethought in patterning, and the beam quality can suffer from thermal lens effects.

The deepest structure machined was  $160\ \mu\text{m}$  depth using an overlap of 85.8% and 4 passes resulting in a diaphragm thickness of  $100\ \mu\text{m}$ . The process produced 3D diaphragm structures with smooth surfaces. This comparison with ultra-short pulsed lasers showed similar quality but higher material removal rates. Others have indicated that operating ultra-short laser at lower fluence can result in higher quality surfaces at the expense of a lower etch rate. Alternatively the use of a more reliable laser system such as a fiber laser (which is known to have a better beam profile and stability [22]) could lead to better surface finish compared to the Nd:YAG with comparable machining times.

## Acknowledgements

This material is based in part upon work supported by the National Science Foundation under Grant Number CMMI-0619115. The authors would like to thank Quantronix for experiments on ultra-short pulse micromachining. Any opinions, findings, and conclusions or recommendations expressed in this material are those of the authors and do not necessarily reflect the views of the National Science Foundation.

## References

1. *The MEMS Handbook*, ed. M. Gad-el-Hak. 2002, Boca Raton, FL, USA: CRC Press.

2. Spera, A.R. *Pulsed Nd:YAG Laser Processing of Si<sub>3</sub>N<sub>4</sub>*. in *Using Advanced Ceramics in Manufacturing Applications*. 1991. Cincinnati, Ohio: Society of Manufacturing Engineers.
3. Kim, S., et al., *SiC via holes by laser drilling*. Journal of Electronic Materials, 2004. **33**(5): p. 477-480.
4. Reitano, R., P. Baeri, and N. Marino, *Excimer laser induced thermal evaporation and ablation of silicon carbide*. Applied Surface Science, 1996. **96-98**: p. 302-308.
5. Zhang, J., et al., *Direct photoetching of single crystal SiC by VUV-266 nm multiwavelength laser ablation* Applied Physics A: Materials Science & Processing, 1997. **64**: p. 367-371.
6. Sugioka, K.M., Katsumi. *Novel technology for laser precision microfabrication of hard materials*. in *First International Symposium on Laser Precision Microfabrication*. 2000: SPIE.
7. Desbiens, J.-P. and P. Masson, *ArF excimer laser micromachining of Pyrex, SiC and PZT for rapid prototyping of MEMS components*. Sensors and Actuators A, 2007. **136**: p. 554-563.
8. Kreutz, E.W., R. Weichenhain, and A. Horn. *Nd:YAG laser micromachining of SiC precision structures for MEMS*. in *MEMS design, fabrication, characterization, and packaging*. 2001.
9. Tian, Z., *Laser Metallization and Doping for Silicon Carbide Diode Fabrication and Endotaxy*, in *Engineering and Computer Science*. 2006, University of Central Florida: Orlando Florida. p. 167.

10. Anderson, T., et al., *Laser ablation of via holes in GaN and AlGaN/GaN high electron mobility transistor structures*. Journal of Vacuum Science Technology B, 2006. **24**(5): p. 2246-2249.
11. Anderson, T.J., et al., *Comparison of Laser-Wavelength Operation for Drilling of Via Holes in AlGaN/GaN HEMTs on SiC Substrates*. Journal of Electronic Materials, 2006. **35**(4): p. 675-679.
12. Dutto, C., E. Foggarassy, and D. Mathiot, *Numerical and experimental analysis of pulsed excimer laser processing of silicon carbide*. Applied Surface Science, 2001. **184**: p. 362-366.
13. De Unamuno, S. and E. Fogarassy, *A Thermal Description of the Melting of c- and a-Silicon Under Pulsed Excimer Lasers*. Applied Surface Science, 1989. **36**: p. 1-11.
14. Logothetidis, S. and J. Petalas, *Dielectric function and reflectivity of 3C-silicon carbide and the component perpendicular of the c axis of 6H-silicon carbide in the energy region 1.5-9.5 eV*. Journal of Applied Physics, 1996. **80**(3): p. 1768-1772.
15. Dubrovskii, G.B., A.A. Lepneva, and E.I. Radovanova, *Optical absorption associated with superlattice in silicon carbide crystals*. Physica Status Solidi (b), 1973. **57**(1): p. 423-431.
16. Metev, S.M. and V.P. Veiko, *Laser-Assisted Micro-Technology*. Second ed, ed. R.M.J. Osgood. 1998, New York, NY: Springer. 270.
17. Tian, Z., N.R. Quick, and A. Kar, *Characterization of 6H-Silicon Carbide PIN Diodes Prototyping by Laser Doping*. Journal of Electronic Materials, 2005. **34**(4): p. 430-438.

18. Tian, Z., N.R. Quick, and A. Kar, *Laser-enhanced diffusion of nitrogen aluminum dopants in silicon carbide*. Acta Materialia, 2006. **54**: p. 4273-4283.
19. Zhang, J., et al., *Direct photoetching of single crystal SiC by VUV-266 nm multiwavelength laser ablation* Applied Physics A: Materials Science & Processing, 1997. **64**: p. 367-371.
20. Edmond, J.A., J.W. Palmour, and R.F. Davis, *Chemical Etching of Ion Implanted Amorphous Silicon Carbide*. Journal of Electrochemical Society: Solid-State Science and Technology, 1986. **133**(3): p. 650-652.
21. Dong, Y., in *Mechanical Engineering*. 2003, Iowa State University: Ames, IA, USA.
22. Gu, B., *Laser Micro-Machining in Semiconductor and Electronics Industries*. Society of Manufacturing Engineers, 2005: p. 1-10.

## CHAPTER 6. MECHANICAL BEHAVIOR OF LASER MICROMACHINED 6H-SiC DIAPHRAGMS

Monolithic diaphragms were laser micromachined from bulk 6H-SiC using a Q-switched Nd:YAG laser operating at 1064 nm, 3 kHz, and pulse width  $< 100$  ns. Square diaphragms of size 1.5 x 1.5 mm and 2.5 x 2.5 mm to an approximate thickness of 130  $\mu\text{m}$  were fabricated and successfully tested under gas pressure conditions and with a micro indentation tester. The results indicate that the diaphragms remained hermetically sealed under loading as high as 435 psi and the deflection curves indicates substantial variation in the thickness of the machined diaphragms.

### 6.1. Introduction

Laser micromachining of silicon carbide has previously been demonstrated for via hole formation [1, 2] and fabrication of amorphous and 4H-SiC diaphragms [3][4]. The diaphragms in this report were fabricating using a 1064 nm Q-switched Nd:YAG laser with FWHM pulse width  $< 100$  ns laser operating at an average power of approximately 0.35 W (see Chapter 5 for more information). To the author's knowledge there has been no prior studies where the laser micromachined diaphragms have been experimentally tested and verified for: i) mechanical and ii) hermetically sealed integrity. The material removal rate within the beam is much higher than other etch methods, on the order of  $50 \mu\text{m s}^{-1}$  for similar IR lasers [1] and that there is poor consistency from pulse to pulse using lamp pumping [5]. The high etch rate and the possibility for variation in the power density from pulse to pulse suggests that large variations in the depth of the diaphragm are possible. This raises doubts

over the use of the Q-switched Nd:YAG laser in its ability to achieve thin diaphragms for pressure sensor applications.

## 6.2. Experimental Details

Three diaphragms were prepared using the process parameters described in Chapter 5 using a 1064 nm Q-switched Nd:YAG laser with FWHM pulse width <100 ns. The diaphragms were machined in a square configuration using an average power of 0.35 w, scan speed of 1 mm s<sup>-1</sup> and overlap of 10 μm (~86%). The samples were machined at two different sizes (1.5 x 1.5 mm and 2.5 and 2.5 mm) and treated with chemicals post-laser processing (as shown in Table 13) and subjected to one of two tests i) pressurized N<sub>2</sub> gas environment where the deflection was measured with a micro miniature DVRT and ii) a micro indentation tester with both sides of the diaphragm are open to ambient. The combinations of sample preparation and characterization are shown in Table 13.

**Table 13. Diaphragm process parameters**

	<b>Diaphragm 1</b>	<b>Diaphragm 2</b>	<b>Diaphragm 3</b>
<b>Diaphragm Size</b>	2500 x 2500 μm	1500 x 1500 μm	1500 x 1500 μm
	HCl:H <sub>2</sub> O <sub>2</sub> :H <sub>2</sub> O (5:3:3)	HCl:H <sub>2</sub> O <sub>2</sub> :H <sub>2</sub> O (5:3:3)	HCl:H <sub>2</sub> O <sub>2</sub> :H <sub>2</sub> O (5:3:3)
<b>Chemical Post-Processing</b>	5 minutes HF:HNO <sub>3</sub> (1:1) >24 hours	5 minutes -	5 minutes HF:HNO <sub>3</sub> (1:1) >24 hours
<b>Testing Method</b>	Pressurized N <sub>2</sub> Gas	Pressurized N <sub>2</sub> Gas	Micro Indentation Tester

Measurements of the depth profile using a MicroMiniature DVRT from MicroStrain, Inc. indicated a deviation from the 100 μm thick as described in chapter 5 with the samples being 123, 120, and 128 μm thick, respectively. However the bottom surface of the diaphragm region was covered with a black layer and cross sectional inspection of the

diaphragms after laser processing suggests a large heat affected zone that could affect the overall performance of the diaphragms. The samples studied in chapter 5 were measured using hundreds of data points which revealed a standard deviation of the depth after 4 passes was recorded at 19  $\mu\text{m}$ . The normal quantile plot in Figure 1 indicates that the depth profile does not exhibit ideal normal conditions and is skewed. This does not eliminate the potential for a ‘rogue’ pulse to pierce the diaphragm rendering it useless for pressure sensing applications.

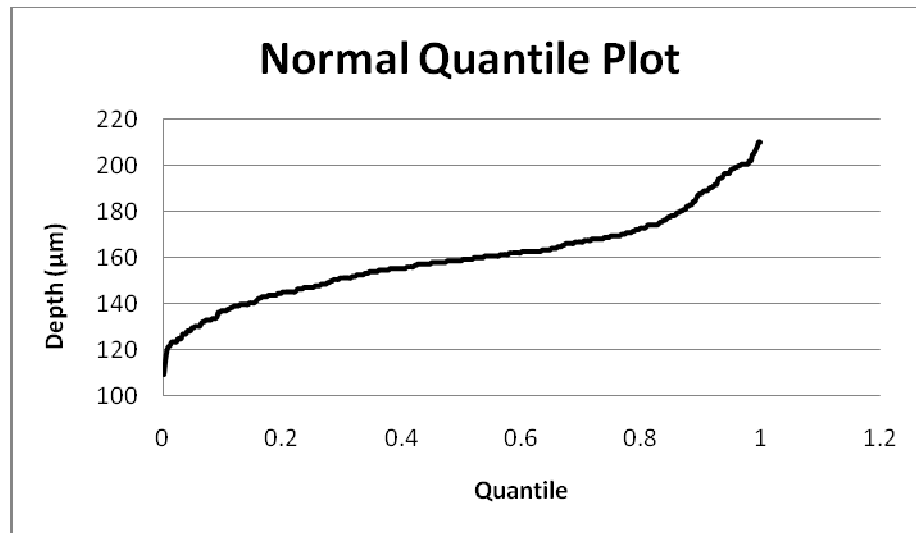


**Figure 31. Normal quantile plot for the depth of a diaphragm machined at 0.35 W average power, overlap 10  $\mu\text{m}$ , 1mm/s scan speed, and 4 passes**

The diaphragm samples were adhered to silicon substrate using a combination of silver paste between the substrate and wafer die and epoxy around the exterior of the wafer die. The samples were then tested under an applied gas pressure in a compressed  $\text{N}_2$  environment using an autoclave pressure vessel (Snap-Tite, Inc.). The deflection of the samples was measured using the DVRT probe with a 100  $\mu\text{m}$  radius that rests on the center of the diaphragm surface. The entire apparatus was placed in the pressure vessel for testing.

The DVRT probe is spring loaded with a spring stiffness of 0.1 N/mm. The diaphragm sample can be precisely adjusted using the fine adjustment screw (100 threads per inch). The sample is held in place with double-stick tape on the aluminum sample holding chuck. A schematic of the pressure testing apparatus can be seen in Figure 32.

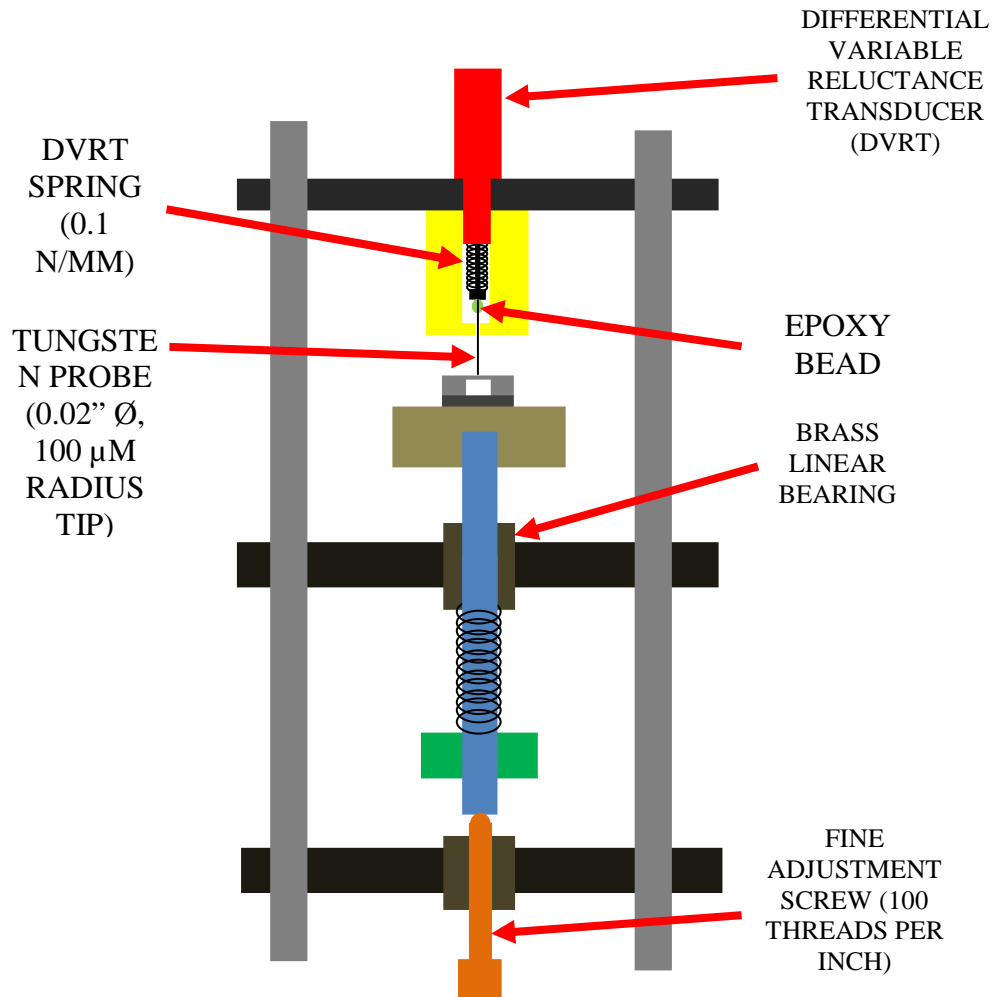


**Figure 32. Schematic of the DVRT pressure testing apparatus**

The DVRT measures the deflection of the diaphragm when a pressure is applied to the entire system which induces a deflection as shown in Figure 33. The DVRT has a minimum resolution of 3  $\mu\text{m}$  allowing for detection of the diaphragm deflection.

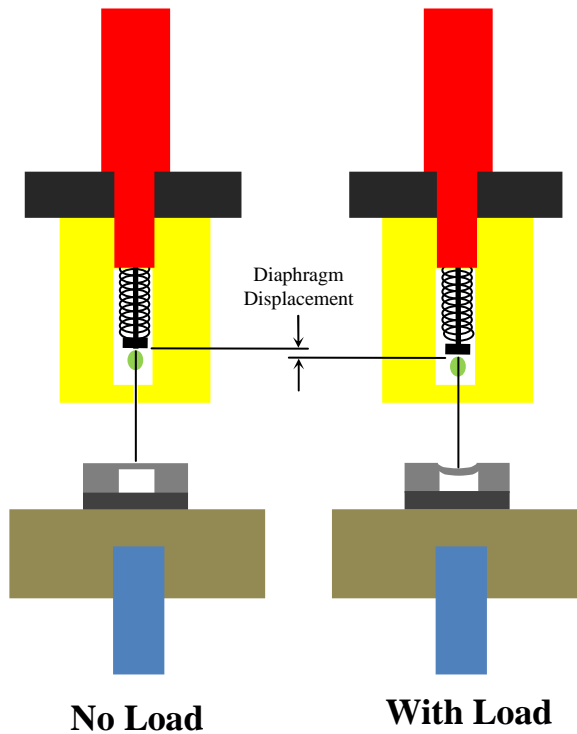


**Figure 33. Schematic of the DVRT measuring the location of the diaphragm under left) no load right) with a pressurized load**

The thinnest possible diaphragm obtained using these machining parameters was estimated to be at a thickness of  $100\ \mu\text{m}$ , however the heat affected zone below the laser machined region may have caused an overall decrease in the strength of the diaphragm such that it behaves as if it were thinner than the measured  $100\ \mu\text{m}$ . The overall stiffness of the diaphragm was calculated assuming a worst case scenario of the diaphragm thickness to be approximately 3 standard deviations deeper than the mean ( $45\ \mu\text{m}$ ). For a  $2500 \times 2500\ \mu\text{m}$  diaphragm, the overall diaphragm stiffness was calculated to be 65 times greater than the DVRT spring stiffness and the overall effect of the DVRT spring from the pre-loading at  $1.5\ \text{mm}$  of spring compression was estimated to be  $< 8\ \mu\text{m}$ . Refer to Appendix B for more information on the stiffness calculations. The sample is held in place on the DVRT apparatus

with a piece of double stick tape. When the pressure is applied, the sample did not shift in position, allowing for measurement of the diaphragm deflection. Actual pressure measurements were conducted using a conventional pressure gauge from Omega, Inc. The voltage output from the DVRT and pressure transducer was measured simultaneously on a BenchLink Data Logger.

### 6.3. Numerical Models for Diaphragm Deflection

The diaphragms were purposely built oversized in comparison to a conventional MEMS pressure sensor diaphragm to achieve an exaggerated deflection for testing purposes. The diaphragms are assumed to be isotropic materials modeled by the Navier elastic body equation (Equation 5)

#### Equation 5

$$\rho h \frac{\partial^2 w}{\partial t^2} - \mu h \nabla^2 w + D \nabla^4 w = f(x, y, z)$$

Where the equation can be simplified by neglecting the stretching term (2<sup>nd</sup> term) and converting it to Cartesian coordinate as shown in Equation 6.

#### Equation 6

$$\frac{\partial^4 w}{\partial x^4} + 2 \frac{\partial^4 w}{\partial x^2 \partial y^2} + \frac{\partial^4 w}{\partial y^4} = \frac{p_z(x, y)}{D}$$

Where the flexural rigidity (D) is given by:

#### Equation 7. Flexural rigidity

$$D = \frac{Eh^3}{12(1-\nu^2)}$$

Where:

E: Young's modulus

h: plate thickness

$\nu$ : Poisson's ratio

Previous studies involving mechanical modeling of silicon carbide used the Young's modulus:  $E = 448 \text{ GPa}$  [6] and poisson's ratio:  $\nu = 0.16$  [7]

Two possible boundary conditions to the equation involve assuming the diaphragm exhibits either hinged edges or clamped edges. Despite the fact that the edges are in fact built into the bulk material, MEMS diaphragms are conventionally are more accurately modeled using a hinged boundary condition [8]. Equation 8 is a solution to [9] the hinged boundary condition for a uniformly loaded plate.

**Equation 8. Maximum deflection for a uniformly loaded plate with hinged boundary conditions**

$$w_{\max} = 0.00406 \frac{pa^4}{D}$$

In all of the cases the maximum deflection of the diaphragms is highly sensitive to changes in the diaphragm thickness (h) due to its presence in the flexural rigidity, D (Equation 7). This sensitivity proves to be a challenge when assessing the characteristics of the diaphragms by dimensional tolerance alone. It can be seen in Figure 37 that the uncertainty attributed to the actual diaphragm thickness has a strong effect in the range 40 and 50  $\mu\text{m}$  (the results are reported for 2.5 x 2.5 mm diaphragm) which results in a doubling in pressure for a 40  $\mu\text{m}$  diaphragm compared to a 50  $\mu\text{m}$  diaphragm for each respective pressure.

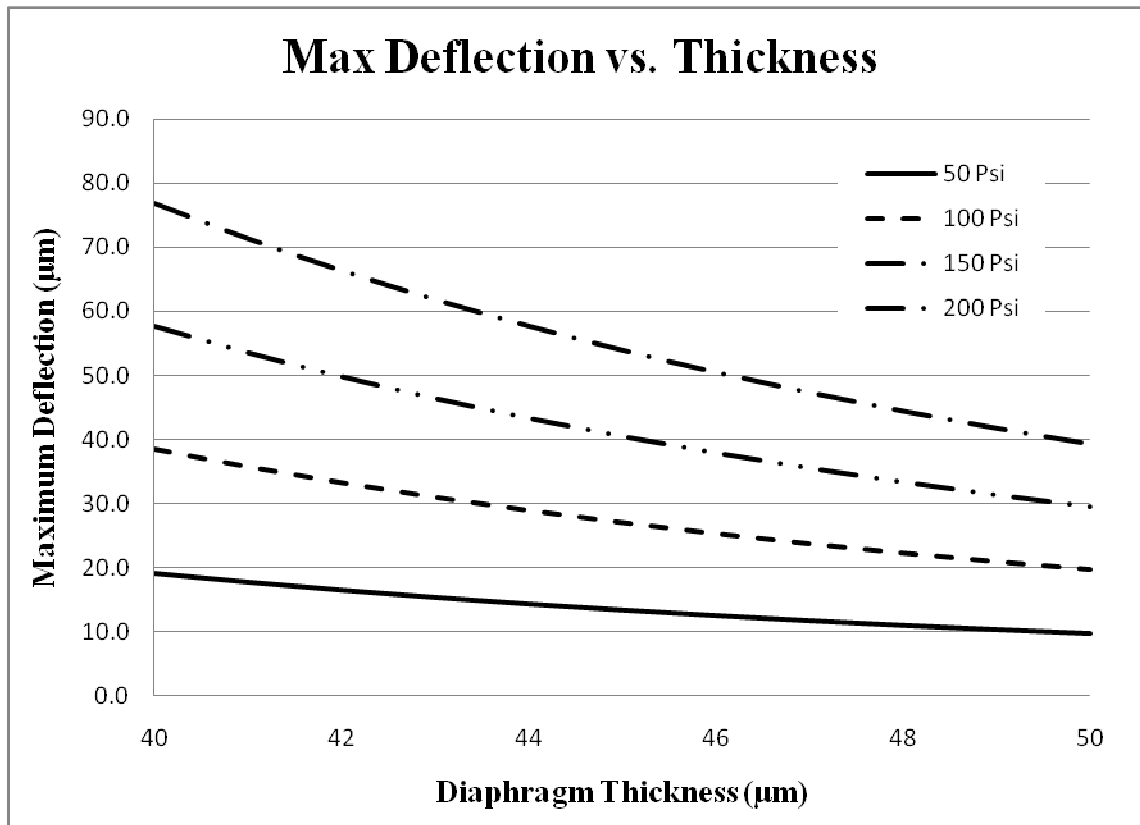


**Figure 34. Deflection versus thickness for a 2.5 x 2.5 mm diaphragm under a distributed load.**

For a concentrated loading case there are no recommended guidelines for use of either hinged or clamped boundary conditions [10]. The maximum deflection for a point loaded diaphragm with hinged and clamped boundary conditions are shown in Equation 9 and Equation 10 respectively.

**Equation 9. Point loading with hinged boundary conditions**

$$w_{max} = \frac{Pa^2}{D\pi^3}(3.087)$$

**Equation 10. Point loading with clamped boundary conditions**

$$w_{max} = \frac{(0.00560)Pa^2}{D}$$

Similarly the effect of deflection for the concentrated loading case is also highly sensitive to changes in the diaphragm thickness. The deflection as a function of diaphragm thickness for hinged and clamped boundary conditions can be seen in Figure 35 and Figure 36.

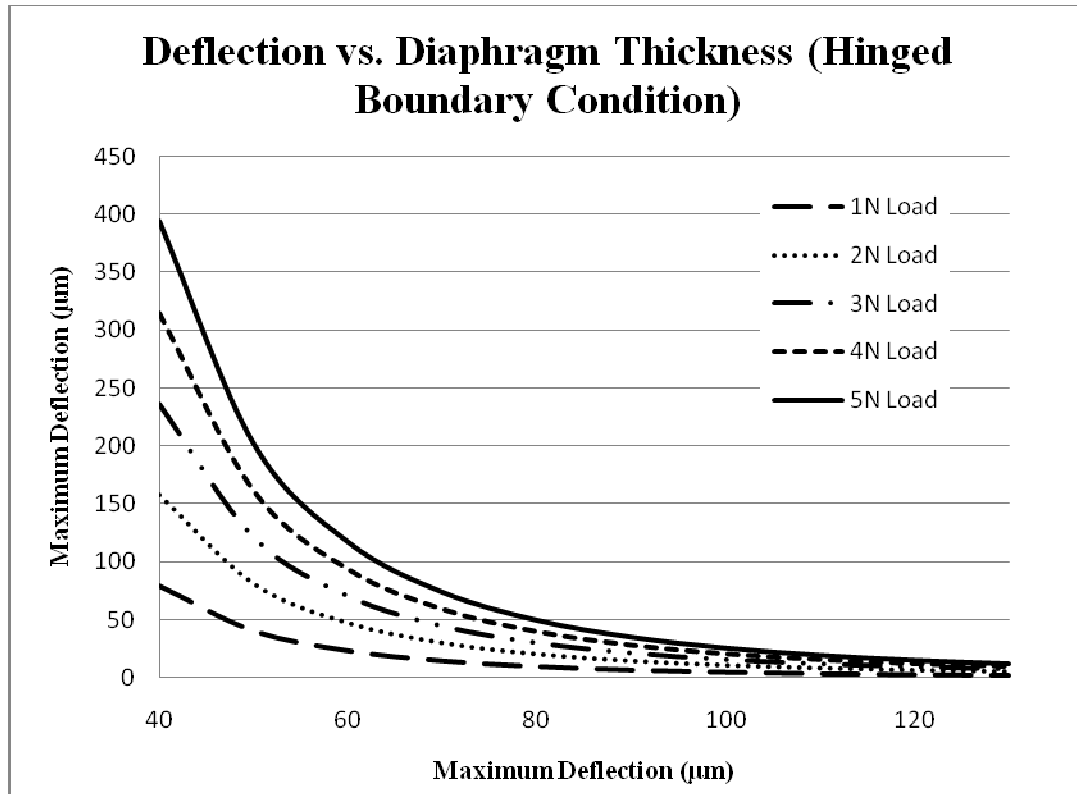


**Figure 35. Deflection versus diaphragm thickness for a 1.5 x 1.5 mm diaphragm with a hinged boundary condition**

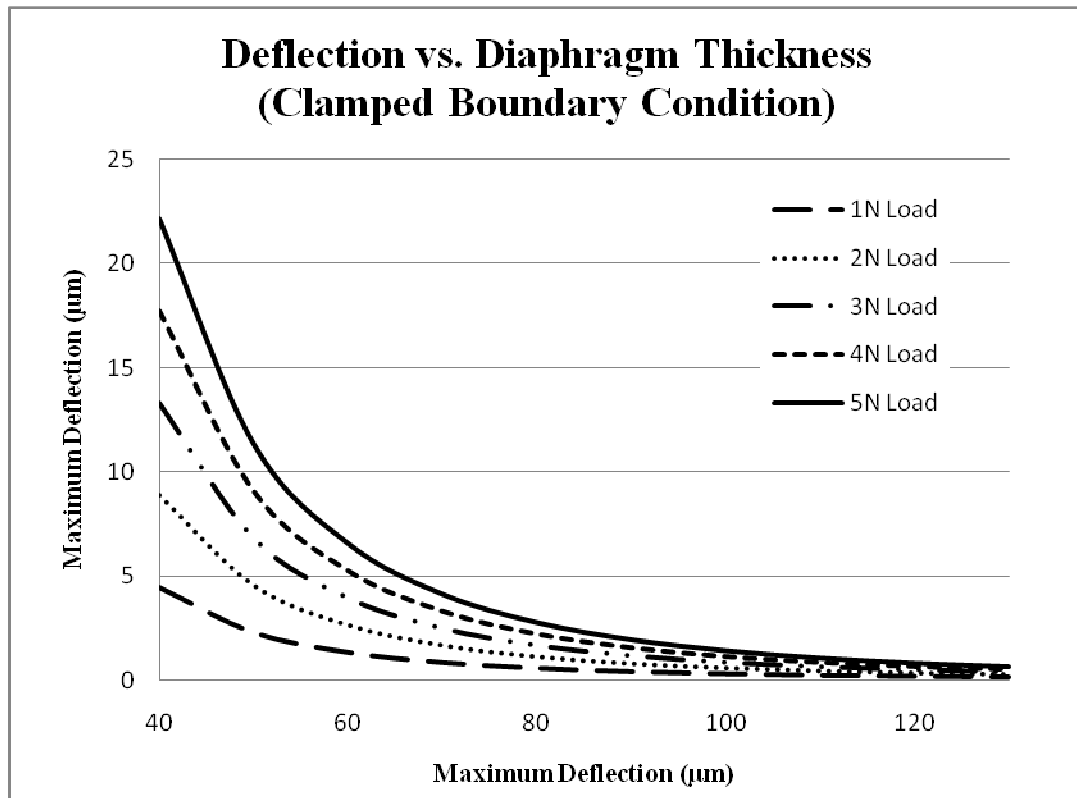


**Figure 36. Deflection versus diaphragm thickness for a 1.5 x 1.5 mm diaphragm with a clamped boundary condition**

#### 6.4. Pressure Testing Results

Pressure testing was carried out for diaphragm 1 up to a pressure of 135 psig and diaphragm 2 up to a maximum pressure of 435 psig. Sample 1 was tested two different times as indicated by the solid line for test 1 and the dashed line for test 2. The testing apparatus is highly sensitive to rapid changes in pressure. It can be seen (Figure 37) that the discontinuities in data were attributed to errors in testing whereby a valve was opened suddenly therein disturbing the system. The dashed line indicates a significant error during the depressurization, however, the tests indicate similar behavior of the diaphragm. The readings from the sensor were skewed from zero depending upon the adjust screw set point and the values were adjusted to zero in Figure 37 and Figure 38.

### Deflection vs. Pressure (2.5 x 2.5 mm)

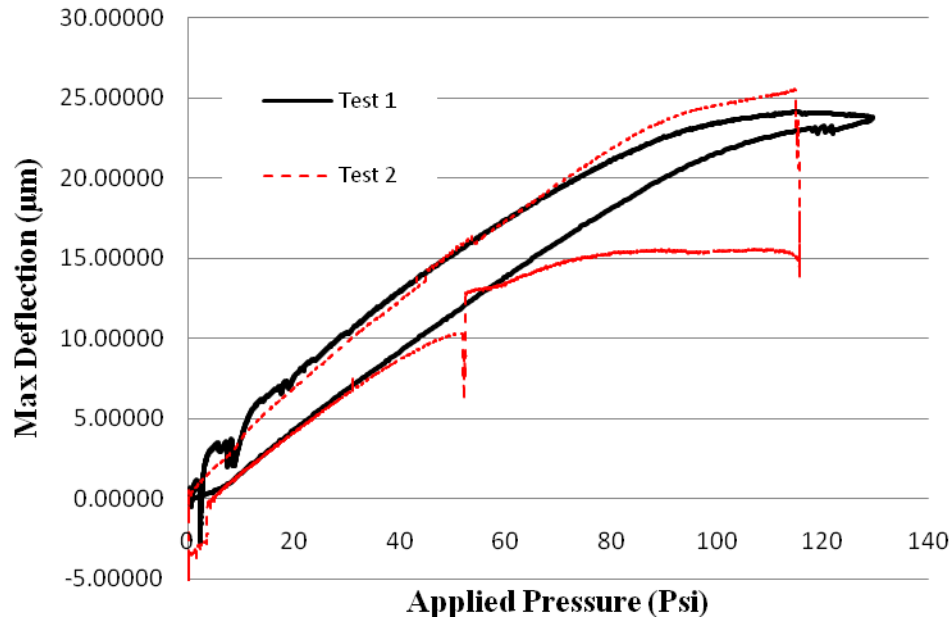


**Figure 37. Pressure Testing Data for Sample 1 (2.5 x 2.5 mm diaphragm)**

A linear curve fit for test 1 of diaphragm 1 indicates a slope of  $m = 0.2345$  with an  $R^2 = 0.9178$ . Diaphragm 2 was tested at a much higher pressure with results indicating a substantially lower deflection with a maximum deflection less than  $8 \mu\text{m}$  (Figure 38). The results of the diaphragm 2 test were less conclusive than the tests for Sample 1. The Slope for diaphragm 2 ( $m = 0.0154$ ,  $R^2 = 0.8564$ ) indicates that the sample behaves as if it is much thicker than diaphragm 1, but this does not agree with the measured results which suggests the samples are very similar in thickness. It is not clear what caused diaphragm 2 to exhibit the unusual hysteresis at the high pressure end of the test, or why it declined to a negative value after returning to ambient pressure. It is possible that the result of Sample 2 has less smoothness because the maximum deflection was only twice the minimum resolution of the DVRT sensor.

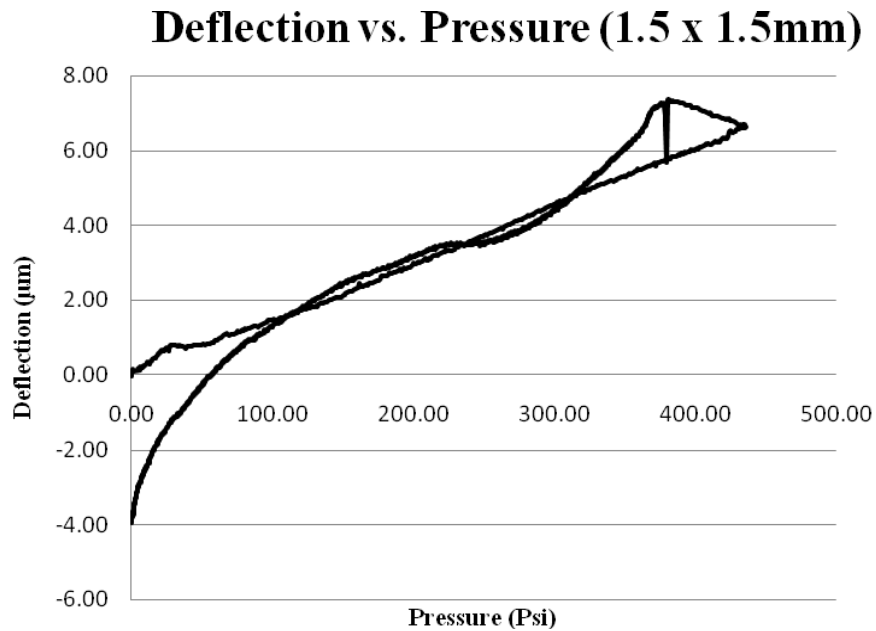


**Figure 38. Pressure Testing Data for Sample 2 (1.5 x 1.5 mm diaphragm)**

The measured thickness of the diaphragms is estimated at 120-130  $\mu\text{m}$ , however the result of the pressurized testing and the assumption that the hinged boundary testing indicates that the actual diaphragm thickness for diaphragm 1 is approximately 50  $\mu\text{m}$  and diaphragm 2 is 62  $\mu\text{m}$ . A summary of the linear fits and the approximated thickness is shown in Table 14.

**Table 14. Pressure Testing fit data and estimated diaphragm thickness**

	<b>Diaphragm 1</b>	<b>Diaphragm 2</b>
<b>Diaphragm Size</b>	2500 x 2500 $\mu\text{m}$	1500 x 1500 $\mu\text{m}$
<b>Slope</b>	0.2345	0.0154
<b>R<sup>2</sup></b>	0.9178	0.8564
<b>Thickness (<math>\mu\text{m}</math>)</b>		
<b>Estimated from Equation 8</b>	48.1	60.3
<b>Thickness (<math>\mu\text{m}</math>)</b>		
<b>Estimated from Measurements</b>	123	120

It is unclear what factors lead to the variation on the diaphragm behavior. A possible cause is the potential for variations in the laser power output and variations in the thickness of the heat affected zone. At this point further testing and characterization should be conducted.

### 6.5. Micro Indentation Testing Results

The micro hardness testing was conducted using a 200  $\mu\text{m}$  radius probe tip and 5 different maximum loads and loading rates were tested on Sample 3. Test 5 resulted in the failure of the diaphragm near the maximum load of 5 N. The testing parameters are summarized in Table 15.

**Table 15. Micro indentation tests conducted on Sample 3**

Test	Maximum Force (N)	Loading/Unloading Rate ( $\text{N min}^{-1}$ )
1	0.5	1.0
2	2.0	4.0
3	3.0	6.0
4	4.0	8.0
5*	5.0	10.0

\* Test 5 resulted in fracture near 5 N load

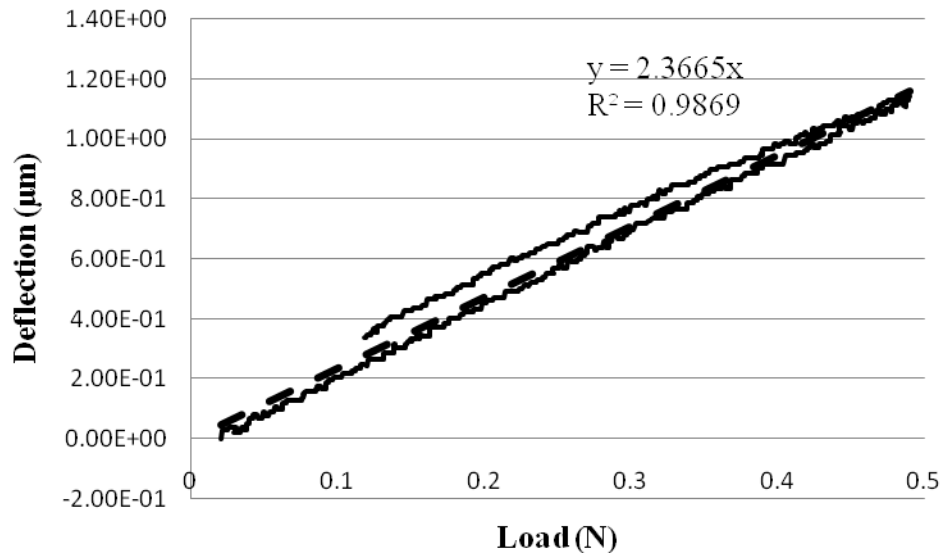


Figure 39. Test 1 of Sample 3 (maximum load 0.5 N)

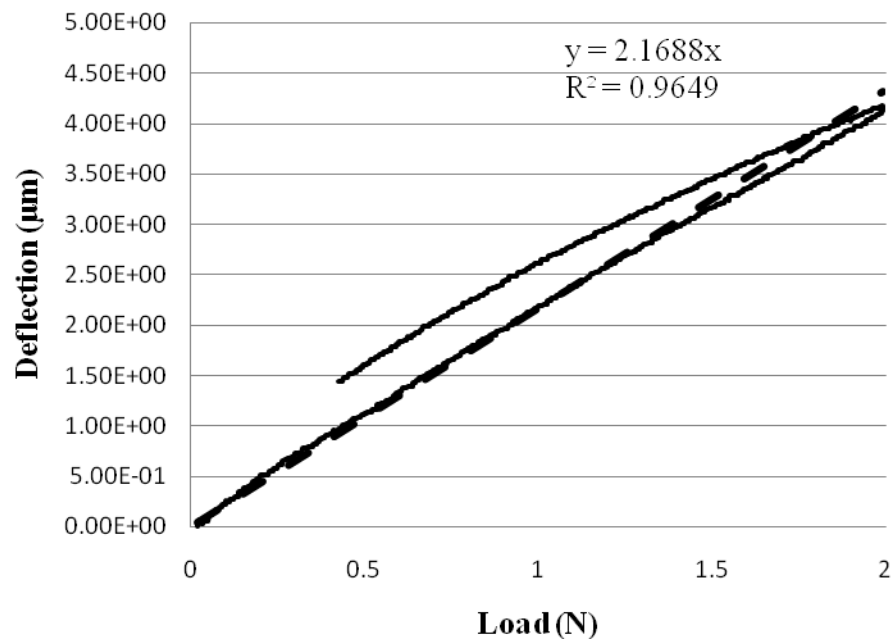


Figure 40. Test 2 of Sample 3 (maximum load of 2.0 N)

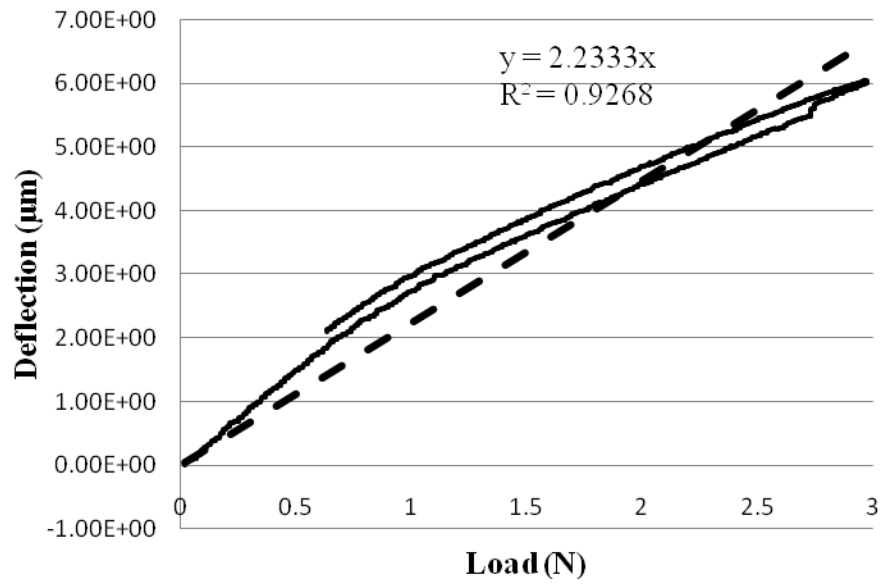


Figure 41. Test 3 of Sample 3 (maximum load of 3.0 N)

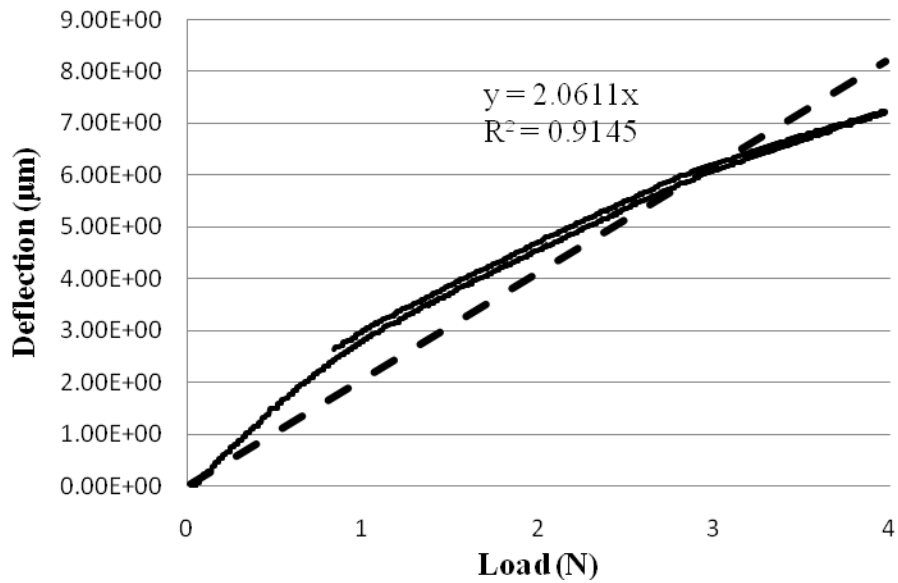
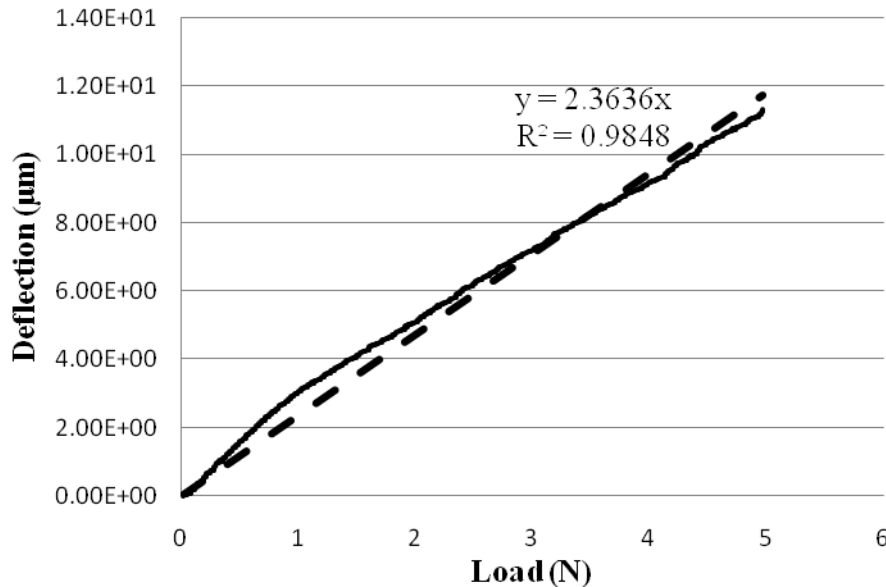


Figure 42. Test 4 of Sample 3 (maximum load of 4.0 N)



**Figure 43. Test 5 of Sample 3 which resulted in fracture of the diaphragm structure (maximum load of 5.0 N)**

The displacement versus load for tests up to 2 N exhibits a strongly linear correlation; however by Test 3 the curve appears to exhibit some non-linear behavior for 3N loading and this same behavior is also seen for Tests 4 and 5. For the micro hardness test the use of the hinged boundary condition for the concentrated loading (Equation 9) resulted in diaphragm thickness between 128 and 134  $\mu\text{m}$ , whereas when assuming a clamped periphery the result was similar to the pressure testing results with a thickness estimated between 49 and 52  $\mu\text{m}$ . The later results are similar to the estimated thickness for diaphragm 1. However, the hinged boundary condition was closer to the estimate made using the DVRT as a measuring device (128  $\mu\text{m}$ ). The results of the models for the hinged and clamped boundary conditions are found in Table 16.

**Table 16. Diaphragm thickness calculated from the slope from Tests 1-5 with clamped and hinged boundary conditions**

Test	m	Diaphragm Thickness ( $\mu\text{m}$ )	
		Clamped	Hinged
1	2.3665	49.30	128.66
2	2.1688	50.75	132.46
3	2.2333	50.26	131.17
4	2.0611	51.62	134.73
5	2.3636	49.32	128.71

## 6.6. Conclusions

The results of the pressure testing and the fitted model data suggests that the diaphragms remained sealed under applied gas pressure. The pressure tested diaphragms were measured to be as thick as 123 and 120  $\mu\text{m}$  thick for diaphragms 1 and 2, respectively. However, the fitted model suggests these diaphragms behave as if they are 48.1 and 60.3  $\mu\text{m}$  thick. Further modeling is required for the concentrated loading case to determine the validity of the clamped versus hinged boundary conditions. In the case of the hinged boundary conditions the model fits the measured estimate of the diaphragm thickness, however it is unlikely that the region within the heat affected zone would contribute the same mechanical strength to the diaphragm as the virgin 6H-SiC material. The black region produced by the laser processing is not easily removed by chemical processing means and further work is required to determine its composition, mechanical properties, and its overall effect on the ability to fabricate 6H-SiC MEMS diaphragms.

The Pressure testing apparatus developed in this work is adequate for detecting the deflection of oversized diaphragms (i.e. Sample 1), however it lacks the resolution to obtain

conclusive results for smaller diaphragm sizes (i.e. Sample 2). Additionally a large hysteresis is present in the pressure testing curves due to possible changes in the contact angle as the diaphragm deflects. Concentrated loading tests conducted with the micro indentation tester have a greater resolution and control over the application of the forces, however the use of a concentrated load still requires the use of mechanical models to estimate the behavior of a diaphragm under a distributed loading situation.

## References

1. Anderson, T., et al., *Laser ablation of via holes in GaN and AlGaIn/GaN high electron mobility transistor structures*. Journal of Vacuum Science Technology B, 2006. 24(5): p. 2246-2249.
2. Anderson, T.J., et al., *Comparison of Laser-Wavelength Operation for Drilling of Via Holes in AlGaIn/GaN HEMTs on SiC Substrates*. Journal of Electronic Materials, 2006. 35(4): p. 675-679.
3. Desbiens, J.-P. and P. Masson, *ArF excimer laser micromachining of Pyrex, SiC and PZT for rapid prototyping of MEMS components*. Sensors and Actuators A, 2007. 136: p. 554-563.
4. Dong, Y., in *Mechanical Engineering*. 2003, Iowa State University: Ames, IA, USA.
5. Gu, B., *Laser Micro-Machining in Semiconductor and Electronics Industries*. Society of Manufacturing Engineers, 2005: p. 1-10.
6. Atwell, A.R., et al., *Simulation, fabrication and testing of bulk micromachined 6H-SiC high-g piezoresistive accelerometers*. Sensors and Actuators A, 2003. 104: p. 11-18.

7. Strunk, H.P., W. Dorsch, and J. Heindl, *The Nature of Micropipes in 6H-SiC Single Crystals*. *Advanced Engineering Materials*, 2000. 2(6): p. 386-389.
8. Park, J.-S., C. Wilson, and Y.B. Gianchandani, *Micromachined Pressure Sensors*, in *The MEMS handbook*, M. Gad-el-Hak, Editor. 2002, CRC Press: Boca Raton, FL, USA.
9. Timoshenko, S. and S. Woinowsky-Krieger, *Theory of Plates and Shells*. 2nd ed. 1959, New York: McGRAW-HILL BOOK COMPANY.

## CHAPTER 7. CONCLUSIONS AND RECOMMENDATIONS FOR FUTURE WORK

### 7.1. Summary

Laser micromachining is a viable method for machining both 3C-SiC thin films and bulk 6H-SiC material. This report has presented the analysis of laser micromachining as an alternative method to plasma and electrochemical etching for fabricating bulk silicon carbide MEMS pressure sensor diaphragms. A comprehensive review of laser microscale fabrication of silicon carbide MEMS and micro electronics was conducted to show that lasers are well established tools for microelectronics applications and specifically that laser micromachining can be conducted with various lasers. Chapter 5 describes the laser micromachining procedure to produce deep features on the order of 130-160  $\mu\text{m}$  in depth. The most successful parameters for machining an appropriately thin diaphragm was conducted using an Nd:YAG laser with a spot size of approximately 70  $\mu\text{m}$  with an overlap of 10  $\mu\text{m}$ . The average power of the beam was 0.35 W and the average energy density was 2.52  $\text{J cm}^{-2}$  using the beam and fluence calculations found in Appendix A. Laser micromachined diaphragms were hermetically sealed to a silicon substrate and tested in a pressure vessel. Their deflection was measured using a microminature DVRT probe and it was conclusively determined that the diaphragms are appropriately sealed for these conditions and exhibit characteristics suggesting viability as a MEMS diaphragm. However, at this point is unknown what causes of the variation is between the MEMS diaphragms. This report has served as the framework for the continued development of a functional laser micromachined

diaphragm, however future work is required for its successful implementation as a MEMS device.

## 7.2. Uncertainties of Laser Micromachining of MEMS components

The use of lasers for micromachining a diaphragm should be carefully considered. There are a number of factors that remain uncertain in laser micromachining. Previous work using a nearly identical Nd:YAG laser was conducted by [11] resulted in the successful doping of junctions  $<2\ \mu\text{m}$  in depth. The stark contrast between the work presented in this report and their work is that they reported the majority of the beam going through the wafer at higher fluence with little attenuation ( $6.1\ \text{J cm}^{-2}$ ) while it is claimed here that a lower fluence ( $2.52\ \text{J cm}^{-2}$ ) resulted in the strong ablation of the material. It is uncertain what has lead to this difference but there are a few possible reasons for this difference. In the doping experiments, the Nd:YAG laser irradiated the polished Si-face of the wafer while in our experiments it was conducted on the rough C-face. The reflectivity from the rough face may be higher than that of the polished face resulting in a high concentration of optical absorption on the incident surface. The other factor that may explain the differences is the fact that the lens used in our experiments focused the beam to a much smaller size ( $\sim 70\ \mu\text{m}$ ) compared to that used by Tian et al. ( $\sim 270\ \mu\text{m}$ ). Both used beams with Gaussian profiles, this means that in the case reported here, the power averaged across the beam profile may have been lower, but the actual peak fluence exhibited at the center of the beam may have been higher than that reported by Tian et al.

While this has been discussed in chapter 5, it is still relevant here because as the beam is being strongly absorbed it becomes very difficult to predict the heating profiles of the

material cross section during laser ablation. By the simple Beer-Lambert law it is apparent that a large amount of the laser intensity is transmitted to the backside of the wafer (Equation 11).

**Equation 11**

$$I(z, t) = I_o(t)(1 - R)\exp(-\alpha z)$$

Where:

$t$ : Time

$I_o$ : Laser Intensity at the Surface

$R$ : Surface Reflectivity

$\alpha$ : Optical Absorption

$z$ : Depth below Surface

$I(z, t)$ : Laser intensity at a depth  $z$  below the surface

Assuming an initial intensity of  $\sim 9.1 \times 10^3 \text{ W cm}^{-2}$  as used for the successful fabrication of the diaphragms in this report (Chapter 5) and a reflectivity of 0.2 and absorption coefficient of  $20 \text{ cm}^{-1}$  and wafer thickness of  $260 \mu\text{m}$  (0.026 cm) the laser intensity at the backside of the wafer would be  $4.3 \times 10^3 \text{ W cm}^{-2}$  by the Beer-Lambert law alone.

However the ablation process is far more complicated; during the ablation process a plasma forms at the beam-material interface attenuating the beam. Additional complication arises when a black carbon rich surface appears in the irradiated zone which further alters the optical characteristics of the material on subsequent pulses. These factors combined result in a great difficulty in modeling the heating and make thermal budgeting based on theory out of the scope of this work. Thermal budgets describe the amount of heat that can be added a microelectronics device before the diffusion becomes too great and the device no longer

functions as it was designed. This is of particular importance in the case of the MEMS pressure sensor using piezoresistive elements to sense the deflection because a high flux of heat to the diaphragm surface could result in unintended damage to the epitaxial layer and uncontrolled diffusion of dopants from this layer to the diaphragm. However, it should be noted that the greatest depth of dopant incorporation using the Nd:YAG laser by Tian et al. was determined to be to a junction depth  $<2 \mu\text{m}$  from the surface [11]. Additionally Anderson et al. were able to drill holes in 4H-SiC microelectronics structures and found there to be very little lateral damage to the device and performance characteristics were not affected [1, 2]. This seems to imply that micromachining with conventional Nd:YAG lasers is a viable method, however their use and applications should be carefully due to the thermal nature of their ablation.

### 7.3. Mechanical Consistency of Diaphragms

The variation in the MEMS diaphragms at this point remains unacceptable for large scale production and commercialization. Additional work is required to verify the uniformity of the diaphragm profiles and their consistency. Ideally more work in providing statistical evidence for the consistency of diaphragm quality should be explored. Now that it is understood that the diaphragms machined under the optimized parameters are gas tight, additional nano indentation -type testing would be more appropriate for establishing the characteristics of the diaphragms with greater resolution and accuracy.

It is clear that laser micromachining using Nd:YAG lasers results in a heat affected zone on the bottom surface of the machined region. Additionally the diaphragms exhibit an extremely large standard deviation in the depth of the profile. It is known that the dependence

of the diaphragm deflection has a relationship to the cube of the diaphragm thickness which results in a large changes in the mechanical characteristics when the diaphragm thickness changes. To ensure a higher quality diaphragm the effects of ion milling or other alternatives should be considered for mechanically removing the heat affected zone.

#### **7.4. Laser System Considerations for Faster Production**

In this report the use of femtosecond and nanosecond pulses in the IR regime were considered. The Q-switched Nd:YAG laser was given a special emphasis in this report as a means of a mature technology that exhibits excellent reliability. The Q-switched Nd:YAG laser, however, exhibits variation in the pulse energy caused by fluctuations in the lamp output. Alternative lasers that are becoming an industrial success are the fiber lasers that exhibit better beam quality and greater uniformity from pulse to pulse. Laser beams conventionally exhibit a Gaussian distribution and it should be considered that by increasing the beam size and increasing the beam energy it may be possible to obtain a larger effective beam area whereby the machining time can be improved. However, it seems that increasing the beam may require a much greater increase in the energy density of the beam. Refer to section 7.2. Uncertainties of Laser Micromachining of MEMS components for more detail about the difference between the work reported here and the work done by Tian et al. that used a larger beam size higher fluence and did not result in ablation [11].

#### **7.5. Sensor Design and Implementation**

These investigations in this report only include the laser micromachining and laser parameters necessary for fabricating Silicon Carbide MEMS diaphragms. SiC MEMS

pressure sensors have previously been developed by Okojie et al [12] and includes piezoresistor fabrication and packaging. Future work in the area of laser micromachining of a MEMS pressure sensor requires further evidence that laser is compatible with the piezoresistor style of sensor or development of a capacitance type sensor. Additional work is also required in the area of MEMS packaging to the extent that it would aid the future of the testing process as outlined in the next section.

## 7.6. High Temperature Pressure Testing

The pressure testing apparatus used in this report is fully capable of heating the contents of the pressure vessel to upwards of 500°C and does not require any additional development. However, the DVRT used in this study is limited to a temperature of 175°C. This means that the pressure vessel is fully adequate for testing a completed and packaged sensor with components able to obtain 500°C. This means that more resources can be directed towards the design and fabrication of a sensor in the future.

1. Anderson, T., et al., *Laser ablation of via holes in GaN and AlGaIn/GaN high electron mobility transistor structures*. Journal of Vacuum Science Technology B, 2006. **24**(5): p. 2246-2249.
2. Anderson, T.J., et al., *Comparison of Laser-Wavelength Operation for Drilling of Via Holes in AlGaIn/GaN HEMTs on SiC Substrates*. Journal of Electronic Materials, 2006. **35**(4): p. 675-679.

3. Desbiens, J.-P. and P. Masson, *ArF excimer laser micromachining of Pyrex, SiC and PZT for rapid prototyping of MEMS components*. Sensors and Actuators A, 2007. **136**: p. 554-563.
4. Dong, Y., in *Mechanical Engineering*. 2003, Iowa State University: Ames, IA, USA.
5. Gu, B., *Laser Micro-Machining in Semiconductor and Electronics Industries*. Society of Manufacturing Engineers, 2005: p. 1-10.
6. Atwell, A.R., et al., *Simulation, fabrication and testing of bulk micromachined 6H-SiC high-g piezoresistive accelerometers*. Sensors and Actuators A, 2003. **104**: p. 11-18.
7. Strunk, H.P., W. Dorsch, and J. Heindl, *The Nature of Micropipes in 6H-SiC Single Crystals*. Advanced Engineering Materials, 2000. **2**(6): p. 386-389.
8. Park, J.-S., C. Wilson, and Y.B. Gianchandani, *Micromachined Pressure Sensors*, in *The MEMS handbook*, M. Gad-el-Hak, Editor. 2002, CRC Press: Boca Raton, FL, USA.
9. Timoshenko, S. and S. Woinowsky-Krieger, *Theory of Plates and Shells*. 2nd ed. 1959, New York: McGRAW-HILL BOOK COMPANY.
10. Szilard, R., *Theory and Analysis of Plates*. 1974, Englewood Cliffs, NJ, USA: Prentice-Hall, INC.
11. Tian, Z., *Laser Metallization and Doping for Silicon Carbide Diode Fabrication and Endotaxy*, in *Engineering and Computer Science*. 2006, University of Central Florida: Orlando Florida. p. 167.

12. Okojie, R.S., et al., *Characteristics of a hermetic 6H-SiC Pressure Sensor at 600°C*, in *AIAA Space 2001 Conference and Exposition*. 2001: Albuquerque, NM, USA. p. 1-8.

## APPENDIX A. LASER BEAM CALCULATIONS

Two important parameters to consider when conducting a laser machining process are the spot size on the sample surface and the depth of focus. The depth of focus is the total distance over which the spot size will be within a specified size range such as within 5% of the minimum spot size.

### A.1. Spot Size

$$d_o = 1.22 \frac{\lambda f}{D}$$

where:

$d_o$  : minimum spot size

$\lambda$  : laser wavelength (1064 nm)

$f$  : lens focus length (65 mm)

$D$  : input beam diameter (1.2 mm)

$$d_o = \frac{1.22(1064nm)(65mm)}{(1.2)} \left| \frac{1\mu m}{1000nm} \right| = 70.3\mu m$$

### A.2. Depth of Focus

$$DOF = \frac{8\lambda M^2}{\pi} \sqrt{\rho^2 - 1} \left( \frac{f}{D} \right)^2$$

$\rho$  : tolerance factor (i.e. varies less than 5% from the focal point means  $\rho = 1.05$ )

$M$  : beam mode parameter (assumed to be TEM 00  $\rightarrow M = 1$ )

Let:

$$\rho = 1.01$$

$$DOF = \frac{8(1064nm)^2}{\pi} \sqrt{1.02^2 - 1} \left( \frac{65mm}{1.2mm} \right)^2 \left| \frac{1mm}{1 \times 10^6 nm} \right| = 1.127mm$$

Therefore if the beam is focused on the sample surface it remains in focus (within 1%) for a distance of:

$$\frac{DOF}{2} = \frac{1.127mm}{2} = 0.563mm$$

This is more than adequate for the purpose of drilling a hole < 0.2 mm deep.

## APPENDIX B. DIAPHRAGM DEFLECTION EQUATIONS

The diaphragm structure is central to the pressure sensor. Known material properties and mechanical behavior correlated with a pressure input is what allows the device to be used as a sensor. The deformation of an elastic body under a load can modeled by the Navier equation:

$$\rho h \frac{\partial^2 w}{\partial t^2} - \mu h \nabla^2 w + D \nabla^4 w = f(x, y, z)$$

Diaphragms as elastic bodies can be broken down into two different sub categories: membranes and plates. A membrane is a body which is sufficiently small such that the stretching term (2<sup>nd</sup> term) in the Navier equation dominates. Plates however are rigid bodies with mechanical deformation dominated by bending. Plates are modeled by neglecting the 2<sup>nd</sup> term of the equation and Plates are modeled by neglecting the 3<sup>rd</sup> term of the equation. The Navier elastic body equation for rigid body with can be simplified by removing the stretching term from the equation. The governing equation for a plate subject to lateral loads is given by:

$$\frac{\partial^4 w}{\partial x^4} + 2 \frac{\partial^4 w}{\partial x^2 \partial y^2} + \frac{\partial^4 w}{\partial y^4} = \frac{p_z(x, y)}{D}$$

Where:

$$D = \frac{Eh^3}{12(1-\nu^2)}$$

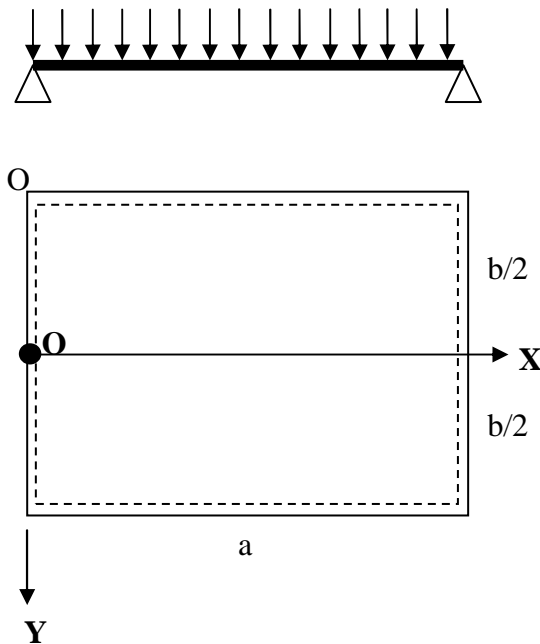
Assumptions:

- 1) Isotropic material
- 2) The DVRT spring has a constant stiffness of (0.1 N/mm)

Parameters:

- 1) The diaphragm has square geometry  $a = b = 2500 \mu\text{m}$
- 2) Diaphragm thickness  $h = 45 \mu\text{m}$
- 3)  $E = 448 \text{ GPa}$
- 4)  $\nu = 0.16$

### B.1. Diaphragm Deflection under Uniform Loading (Hinged Boundary Condition)



$$w = \frac{4pa^4}{\pi^5 D} \sum_{m=1,3,5}^{\infty} \frac{1}{m^5} \left( 1 - \frac{\alpha_m \tanh \alpha_m + 2}{2 \cosh \alpha_m} \cosh \frac{2\alpha_m y}{b} + \frac{\alpha_m}{2 \cosh \alpha_m} \frac{2y}{b} \sinh \frac{2\alpha_m y}{b} \right) \sin \left( \frac{m\pi x}{a} \right)$$

For a square membrane:

$$w_{\max} = 0.00406 \frac{Pa^4}{D}$$

## B.2. Diaphragm Stiffness under Concentrated Loading (Hinged Boundary Condition)

The stiffness calculations are greatly simplified using the Szilzard solution the the Navier bending equation:

$$w = \frac{Pa^2}{D\pi^3} \sum_{m=1}^{\infty} \left( \left( 1 + \beta_m \coth(\beta_m) \right) - \frac{\beta_m y_1}{b} \coth\left(\frac{\beta_m y_1}{b}\right) - \frac{\beta_m \eta}{b} \coth\left(\frac{\beta_m \eta}{b}\right) \right) \times \frac{\sinh\left(\frac{\beta_m \eta}{b}\right) \sinh\left(\frac{\beta_m y_1}{b}\right) \sinh\left(\frac{\beta_m \xi}{a}\right) \sinh\left(\frac{\beta_m x}{a}\right)}{m^3 \sinh(\beta_m)}$$

$w$  : Deflection

$P$  : Concentrated load

$$\beta_m = \frac{m\pi b}{a}$$

$x$  : X-location on the diaphragm surface

$y$  : Y-location on the diaphragm surface

Let:

$$a = b$$

and

$$y_1 = \eta = x = \xi$$

$$w = \frac{Pa^2}{D\pi^3} \sum_{m=1}^{\infty} \left( 1 + \beta_m \coth(\beta_m) \right) \times \frac{\sinh^4\left(\frac{\beta_m}{2}\right)}{m^3 \sinh(\beta_m)}$$

$$w = \frac{Pa^2}{D\pi^3}(3.087)$$

$$P = \frac{wD\pi^3}{(3.087)a^2}$$

$$\frac{dP}{dw} = \frac{D\pi^3}{(3.087)a^2}$$

Stiffness:

$$\frac{dP}{dw} = 8.45 \times 10^4 \text{ N/m}$$

The stiffness of a relatively large diaphragm has high stiffness relative to the DVRT spring thus we can assume that the deflection caused by the DVRT is minimal and has little to no effect on the measurements of the diaphragm deflection in the case of a diaphragm that is 100  $\mu\text{m}$  thick and has side length < 2500  $\mu\text{m}$  square.

## APPENDIX C. DIAPHRAGM DEFLECTION EQUATIONS

The diaphragm structure is central to the pressure sensor. Known material properties and mechanical behavior correlated with a pressure input is what allows the device to be used as a sensor. The deformation of an elastic body under a load can modeled by the Navier equation:

$$\rho h \frac{\partial^2 w}{\partial t^2} - \mu h \nabla^2 w + D \nabla^4 w = f(x, y, z)$$

Diaphragms as elastic bodies can be broken down into two different sub categories: membranes and plates. A membrane is a body which is sufficiently small such that the stretching term (2<sup>nd</sup> term) in the Navier equation dominates. Plates however are rigid bodies with mechanical deformation dominated by bending. Plates are modeled by neglecting the 2<sup>nd</sup> term of the equation and Plates are modeled by neglecting the 3<sup>rd</sup> term of the equation. The Navier elastic body equation for rigid body with can be simplified by removing the stretching term from the equation. The governing equation for a plate subject to lateral loads is given by:

$$\frac{\partial^4 w}{\partial x^4} + 2 \frac{\partial^4 w}{\partial x^2 \partial y^2} + \frac{\partial^4 w}{\partial y^4} = \frac{p_z(x, y)}{D}$$

Where:

$$D = \frac{Eh^3}{12(1-\nu^2)}$$

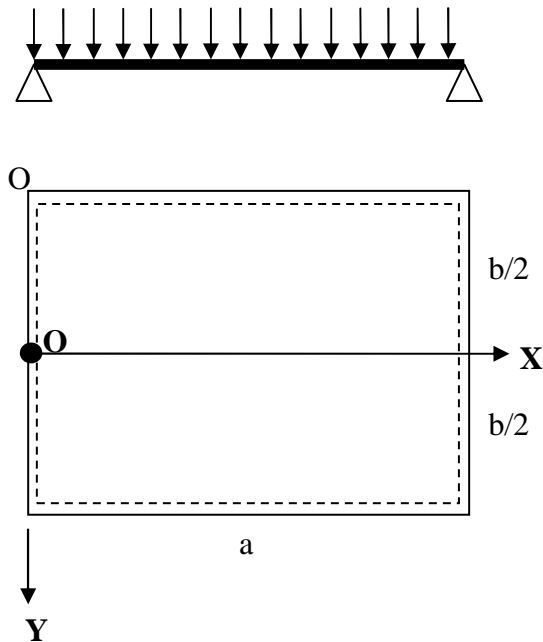
Assumptions:

- 3) Isotropic material
- 4) The DVRT spring has a constant stiffness of (0.1 N/mm)

Parameters:

- 5) The diaphragm has square geometry  $a = b = 2500 \mu\text{m}$
- 6) Diaphragm thickness  $h = 45 \mu\text{m}$
- 7)  $E = 448 \text{ GPa}$
- 8)  $\nu = 0.16$

### C.1. Diaphragm Deflection under uniform Loading (Hinged Boundary Condition)



$$w = \frac{4pa^4}{\pi^5 D} \sum_{m=1,3,5}^{\infty} \frac{1}{m^5} \left( 1 - \frac{\alpha_m \tanh \alpha_m + 2}{2 \cosh \alpha_m} \cosh \frac{2\alpha_m y}{b} + \frac{\alpha_m}{2 \cosh \alpha_m} \frac{2y}{b} \sinh \frac{2\alpha_m y}{b} \right) \sin \left( \frac{m\pi x}{a} \right)$$

For a square membrane:

$$w_{\max} = 0.00406 \frac{pa^4}{D}$$

## C.2. Diaphragm Stiffness under Concentrated Loading (Hinged Boundary Condition)

The stiffness calculations are greatly simplified using the Szilzard solution the the Navier bending equation:

$$w = \frac{Pa^2}{D\pi^3} \sum_{m=1}^{\infty} \left( (1 + \beta_m \coth(\beta_m)) - \frac{\beta_m y_1}{b} \coth\left(\frac{\beta_m y_1}{b}\right) - \frac{\beta_m \eta}{b} \coth\left(\frac{\beta_m \eta}{b}\right) \right) \times \frac{\sinh\left(\frac{\beta_m \eta}{b}\right) \sinh\left(\frac{\beta_m y_1}{b}\right) \sinh\left(\frac{\beta_m \xi}{a}\right) \sinh\left(\frac{\beta_m x}{a}\right)}{m^3 \sinh(\beta_m)}$$

$w$  : Deflection

$P$  : Concentrated load

$$\beta_m = \frac{m\pi b}{a}$$

$x$  : X-location on the diaphragm surface

$y$  : Y-location on the diaphragm surface

Let:

$$a = b$$

and

$$y_1 = \eta = x = \xi$$

$$w = \frac{Pa^2}{D\pi^3} \sum_{m=1}^{\infty} (1 + \beta_m \coth(\beta_m)) \times \frac{\sinh^4\left(\frac{\beta_m}{2}\right)}{m^3 \sinh(\beta_m)}$$

$$w = \frac{Pa^2}{D\pi^3} (3.087)$$

$$P = \frac{wD\pi^3}{(3.087)a^2}$$

$$\frac{dP}{dw} = \frac{D\pi^3}{(3.087)a^2}$$

Stiffness:

$$\frac{dP}{dw} = 8.45 \times 10^4 \text{ N/m}$$

The stiffness of a relatively large diaphragm has high stiffness relative to the DVRT spring thus we can assume that the deflection caused by the DVRT is minimal and has little to no effect on the measurements of the diaphragm deflection in the case of a diaphragm that is 100  $\mu\text{m}$  thick and has side length  $< 2500 \mu\text{m}$  square.

## **APPENDIX D. PRESSURE TESTING APPARATUS OPERATIONAL NOTES**

The apparatus used in the pressure testing experiments consists of a pressure vessel for creating the pressurized load on the diaphragm surface and a Differential Voltage Reluctance Transducer (DVRT model: M-DVRT-PE-3) from Microstrain, Inc. The DVRT specifications can be found below in section 1.1 of this appendix.

### **D.1. DVRT Specifications**

The pressure equalized M-DVRT-PE-3 was used for these experiments with a 3 mm stroke. The pressure equalized version comes with a threaded casing and is capable of having the tip submerged in a pressurized environment up to 1000 psig, however in this apparatus this feature was not used because the entire body of the DVRT was submerged in the pressurized environment. A schematic of the M-DVRT-PE-3 can be found in. The DVRT consists of a coil with a free sliding core and measures to micron resolution by measuring the differential reluctance of the coil. A sine-wave excitation is generated by the DEMOD DC2 at 75 kHz. In this setup the DEMOD-DC2 is powered by a 13 VDC power supply and the power output is measured by a Benchlink data acquisition system and corresponding output recorded on a computer. The pressure output from the pressure transducer are simultaneously measured with the DEMOD-DC2 output which allows for the generation of a deflection vs. pressure output.

## D.2. DVRT Apparatus

The DVRT was mounted onto the apparatus seen below in Figure 44 using the 10-32 UNF case threads while mounted on the bolt rail. The diaphragms were hermetically sealed to a substrate using a silver paste. The sealed diaphragms were then held in place on the sample chuck using double-stick tape. The residual error of the DVRT output as given in the Microstrain, Inc. calibration indicates that the readings of the DVRT are more accurate above -1.0 mm where the full scale of the DVRT is from -1.5 mm to +1.5 mm. A detailed schematic of the DVRT apparatus can be seen below in Figure 45 where it can be seen that the PTFE housing holds the DVRT probe, DVRT spring and the Tungsten probe in place where the Tungsten probe is prevented from sliding out of the housing by a small epoxy bead applied to its end and the assembly is held in place by the PTFE housing which is threaded to the DVRT case. The DVRT spring is pre-strained by using the fine adjustment screw which has a pitch of 100 threads per inch. The effect of submerging the DVRT apparatus in a pressurized environment can be seen in Figure 46 where the left hand side indicates a diaphragm under no pressurized load and the right hand side indicates the diaphragm exhibiting some deflection resulting in a change in the position of the DVRT. This absolute position of the DVRT is measured and a relative displacement from the starting position is used to determine the diaphragm deflection.

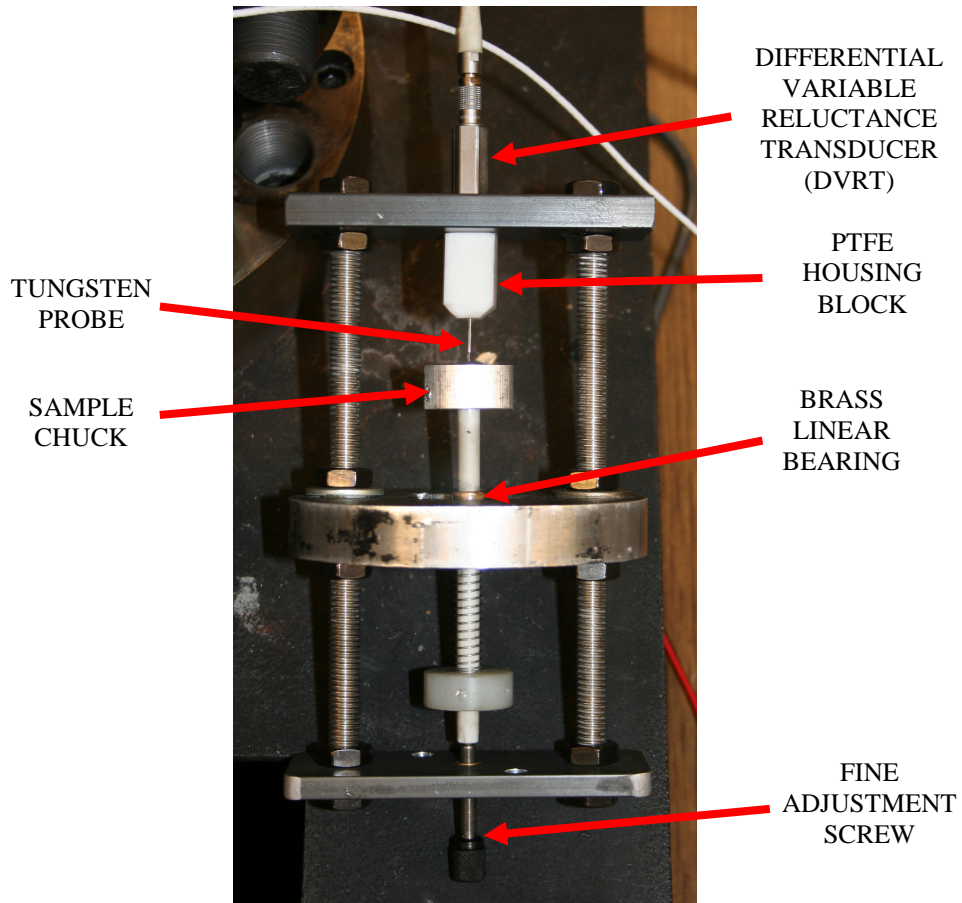


Figure 44. DVRT pressure testing apparatus

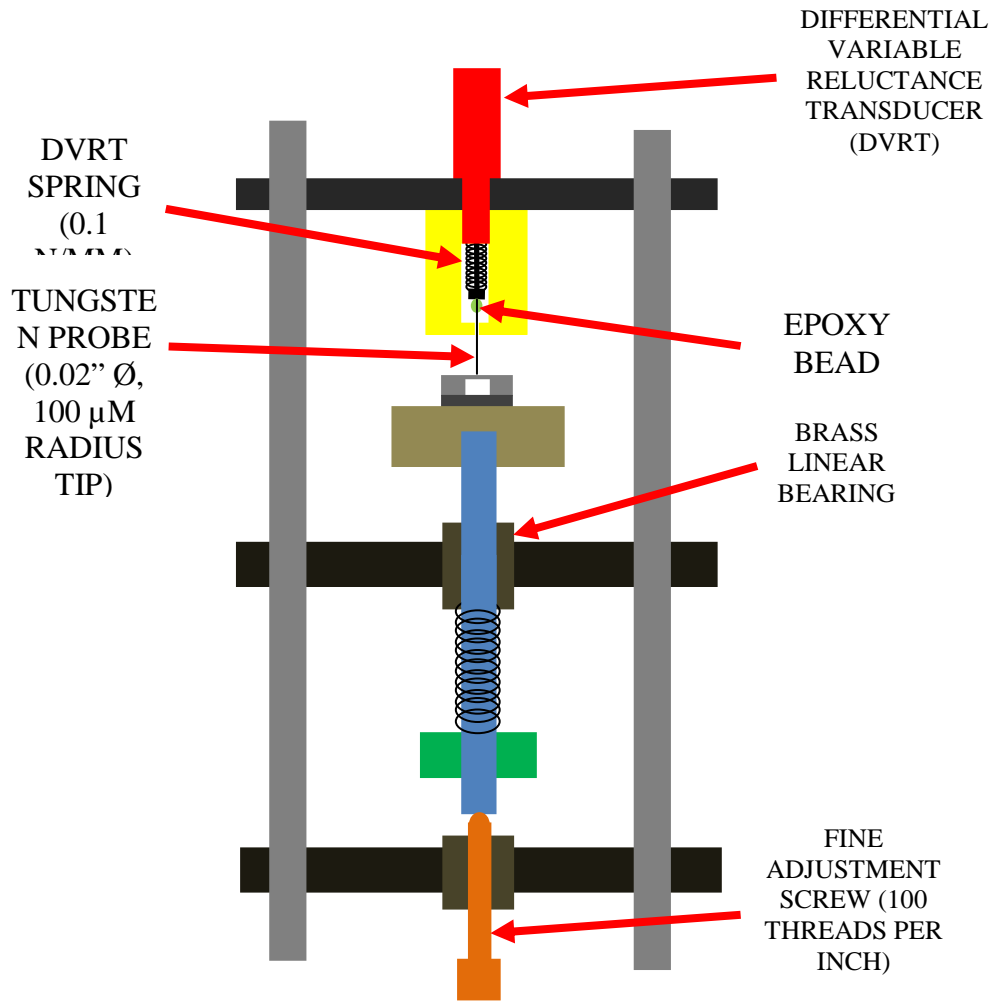
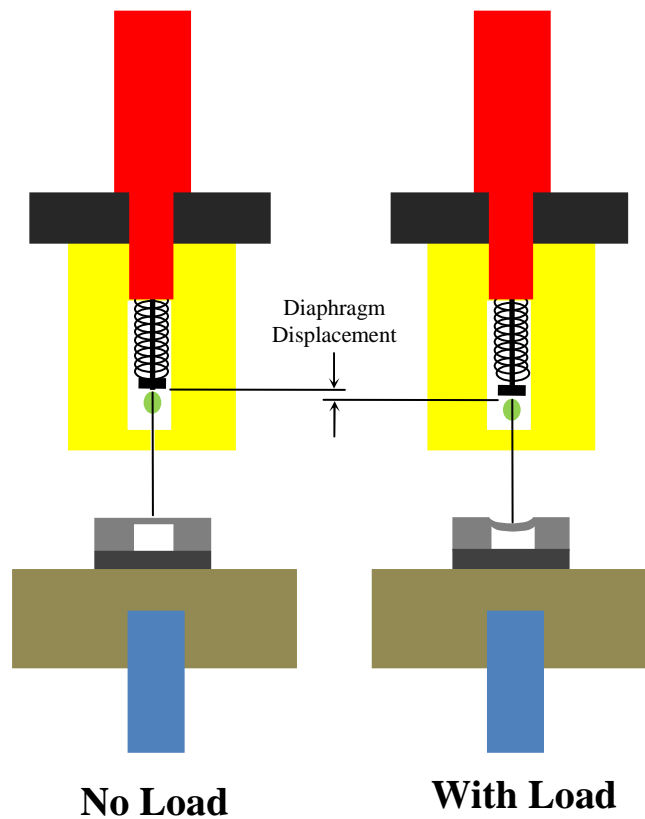


Figure 45. DVRT pressure testing apparatus schematic



**Figure 46. DVRT operational Schematic**

### **D.3. Pressure Vessel Apparatus**

The pressure vessel used for these experiments is a 1 gallon capacity autoclave from Autoclave Engineers, Inc a division of Snap-tite, Inc. as part of the Venus Chamber apparatus capable of achieving pressures ( $< 100$  atmospheres) and temperatures ( $< 500$  C) to simulate the atmospheric conditions on the planet Venus. The chamber system was developed in conjunction with the Iowa NASA space grant consortium and Softronics, Ltd. (Cedar Rapids, IA) for a High Temperature Telemetry Transmitter for Venus Exploration (proposal number: 04 S4.02-9279). The pressure vessel is mounted on a cart as indicated in

Figure 6 and has a system of valves and gauges to obtain the desired pressure. The pressure source used in these experiments was a 255 cubic foot compressed N<sub>2</sub> tank and the pressure measurements were made using an Omega pressure transducer using a 15 VDC input. The voltage output from the pressure transducer was logged along with the DVRT output on the Benchlink Data Logger.

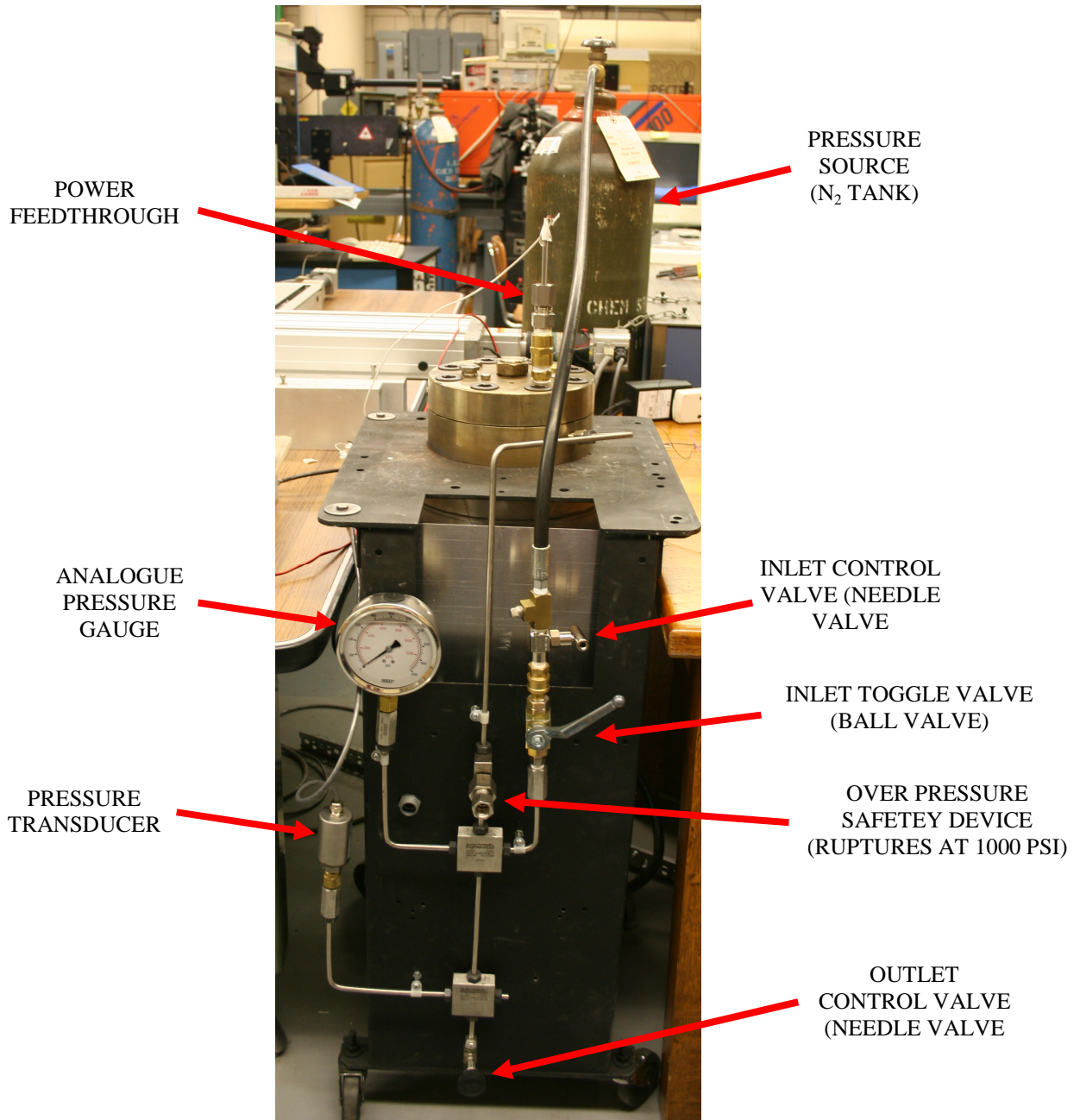


**Figure 47. Pressure vessel used for testing the diaphragms**

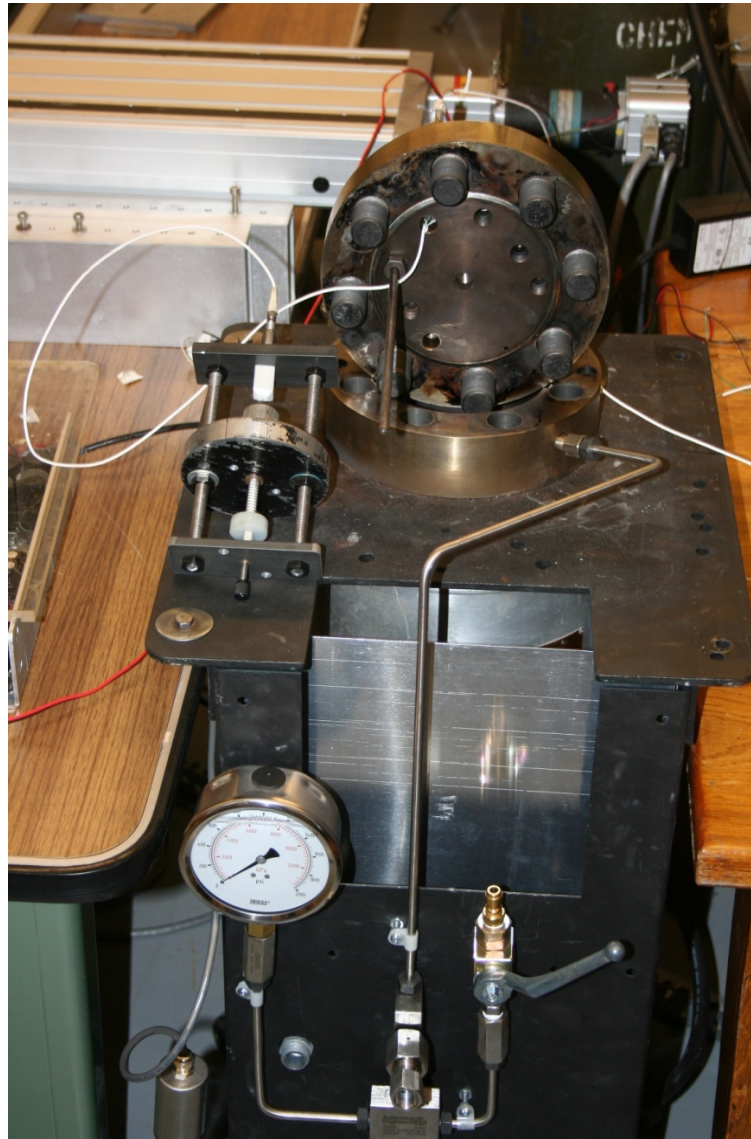


**Figure 48. Pressure vessel and DVRT apparatus**

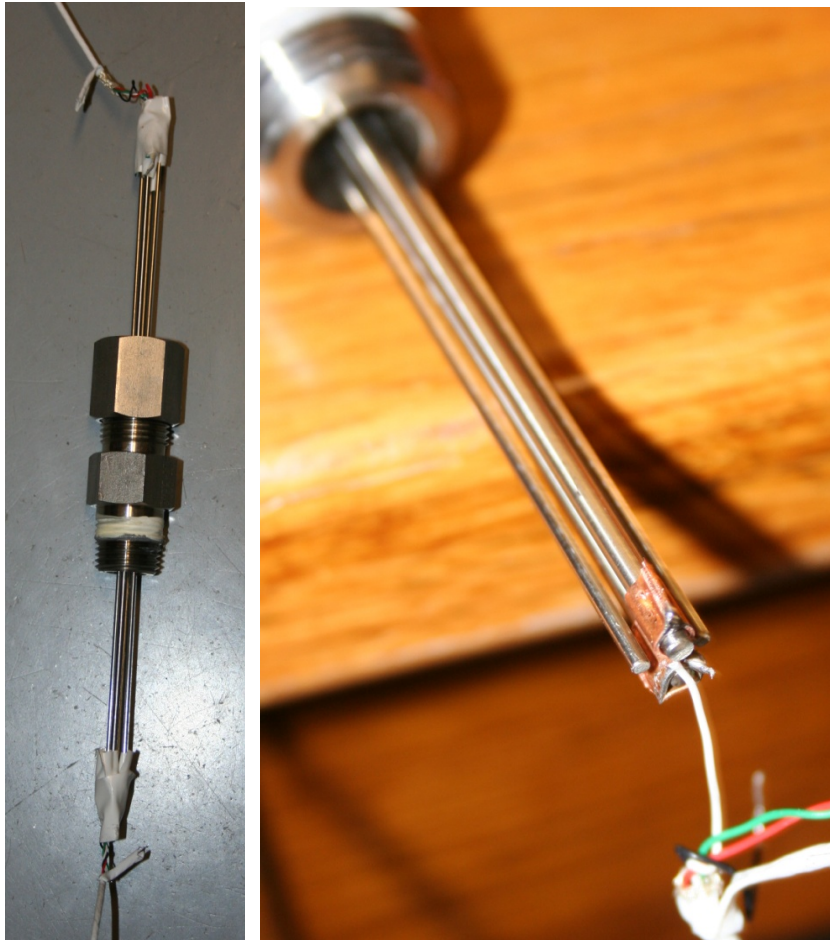


**Figure 49. Feedthrough used on the apparatus**

## APPENDIX E. Nd:YAG MICROMACHINING OF 3C-SiC THIN FILM CANTILEVERS

### E.1. Introduction

3C-SiC is of interest for thinfilm based MEMS devices because of advances in the technology that allows it to be deposited as a single crystalline thin film on Si (100) wafers via CVD. 3C-SiC is highly sought after as an RF switch due to its high young's modulus that could lead to devices with a higher resonant frequency [1].

Nd:YAG lasers have been widely employed for thin film micromachining applications such as scribing, hole drilling, resistor trimming, and thin film patterning [2]. Machining of 3C-SiC by Nd:YAG laser has been limited due to its poor optical absorption at the fundamental frequency (1064 nm) ( $< 250 \text{ cm}^{-1}$ ) and frequency doubled wavelength (532 nm) which is substantially lower [3]. Additionally the wavelength of the 1064 nm Nd:YAG laser (1.17 eV) exceeds the bandgap for crystalline silicon (1.12 eV) indicating a high optical absorption. Indeed, 1064 nm Nd:YAG lases have been shown to have high absorption on silicon with the effect of disordering the region which can be quickly removed with subsequent chemical etching [4, 5].

### E.2. Experimental Details

Cantilevers on 3C-SiC were fabricated using a Q-switched Nd:YAG laser operating at 1064nm, 10 kHz, using a reflective objective lens. Structures were direct written on the 3C-SiC thin film using a computer controlled XY table (LabMotion series, Coherent, Inc.) capable of  $10 \text{ mm s}^{-1}$  and a minimum resolution of  $1 \mu\text{m}$ . Cantilevers were micromachined

and released using an isotropic etchant solution and tested on a MTS Nano G200 nanoindenter to test the stiffness. A series of laser passes at an average power of 0.5 W and scan speeds ranging from  $1 \text{ mm s}^{-1}$  to  $9 \text{ mm s}^{-1}$ . SEM images taken of the various scan speeds (Figure 50) indicated that there was little difference of the scanned range except that at lower speeds the separation between the edges of the 3C-SiC were more pronounced and the recast of the underlying Si substrate seemed to be lower suggesting more of the Si substrate was ablated where recast layers were more prevalent at  $5\text{-}9 \text{ mm s}^{-1}$ .

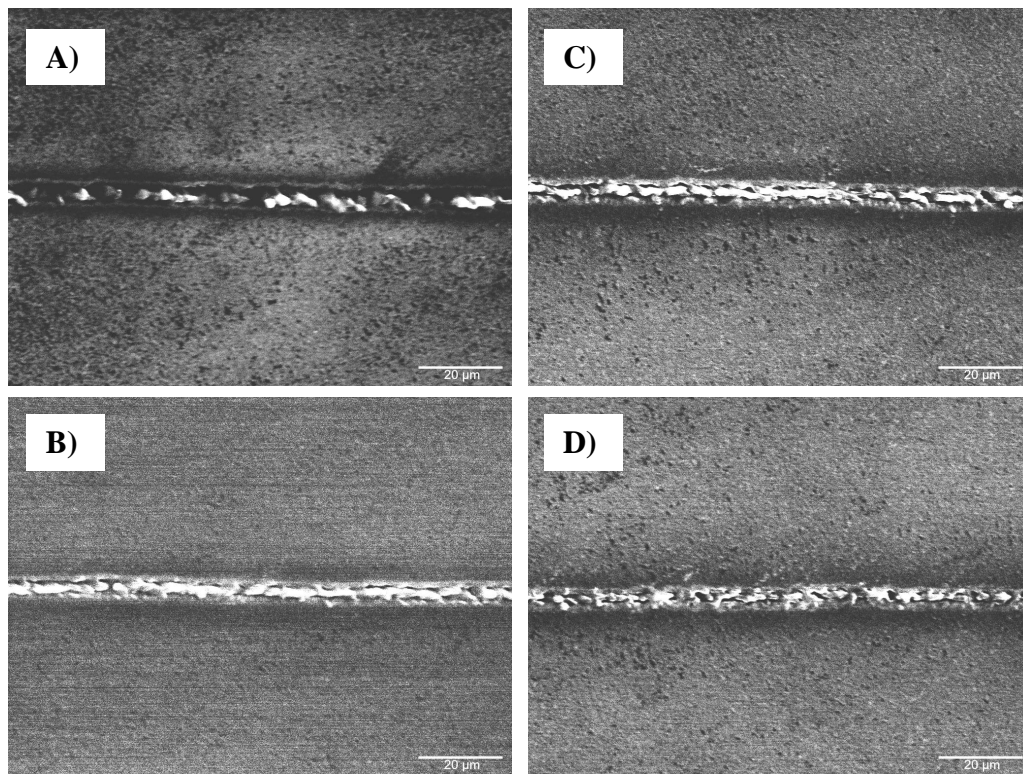


**Figure 50. Laser passes on 3C-SiC A)  $1 \text{ mm s}^{-1}$  B)  $5 \text{ mm s}^{-1}$  C)  $7 \text{ mm s}^{-1}$  D)  $9 \text{ mm s}^{-1}$**

The laser machining proceeded with two groupings of a number of parallel passes with an overlap of  $10 \mu\text{m}$  all starting from the same location to minimize the damage to the cantilever structure from the initial high energy first pulse of the laser. This phenomenon is

sometimes known as giant pulse syndrome (GPS). A series of parallel passes were made perpendicular to the first and second groupings to create a cantilever outline as indicated below in Figure 51.

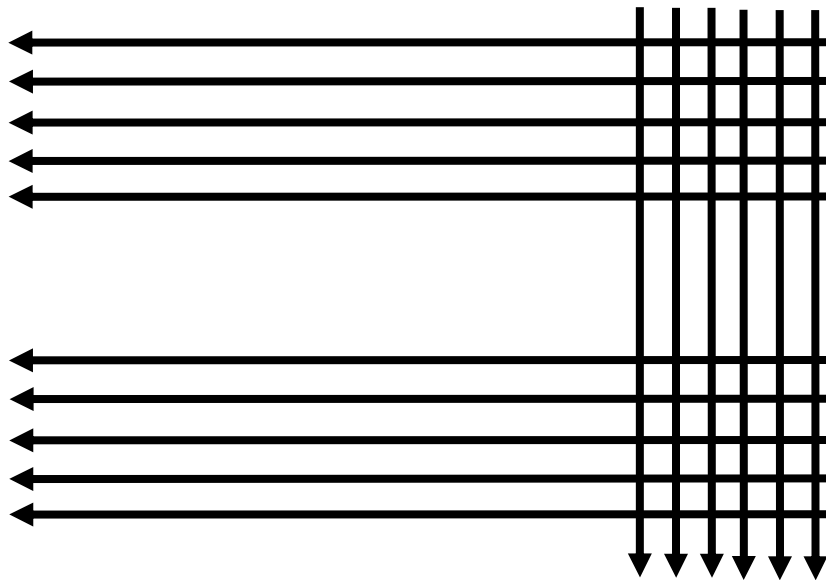


**Figure 51. Cantilever micromachining schematic**

The SEM image of a micromachined cantilever structure can be seen before the substrate release in Figure 52 and after the release in Figure 53. It can be seen from the released structure in Figure 53 that the edges remain jagged and materials appear to have not released from the substrate remain attached. The edge quality can be greatly improved by conducting a set of finishing passes Figure 54 whereby a duplicate pass is made along each edge to ablate more material. Replicating the edge passes results in a much smoother edge profile as seen in Figure 55. However, cracks can be seen in the structure at the corners of the machined area.

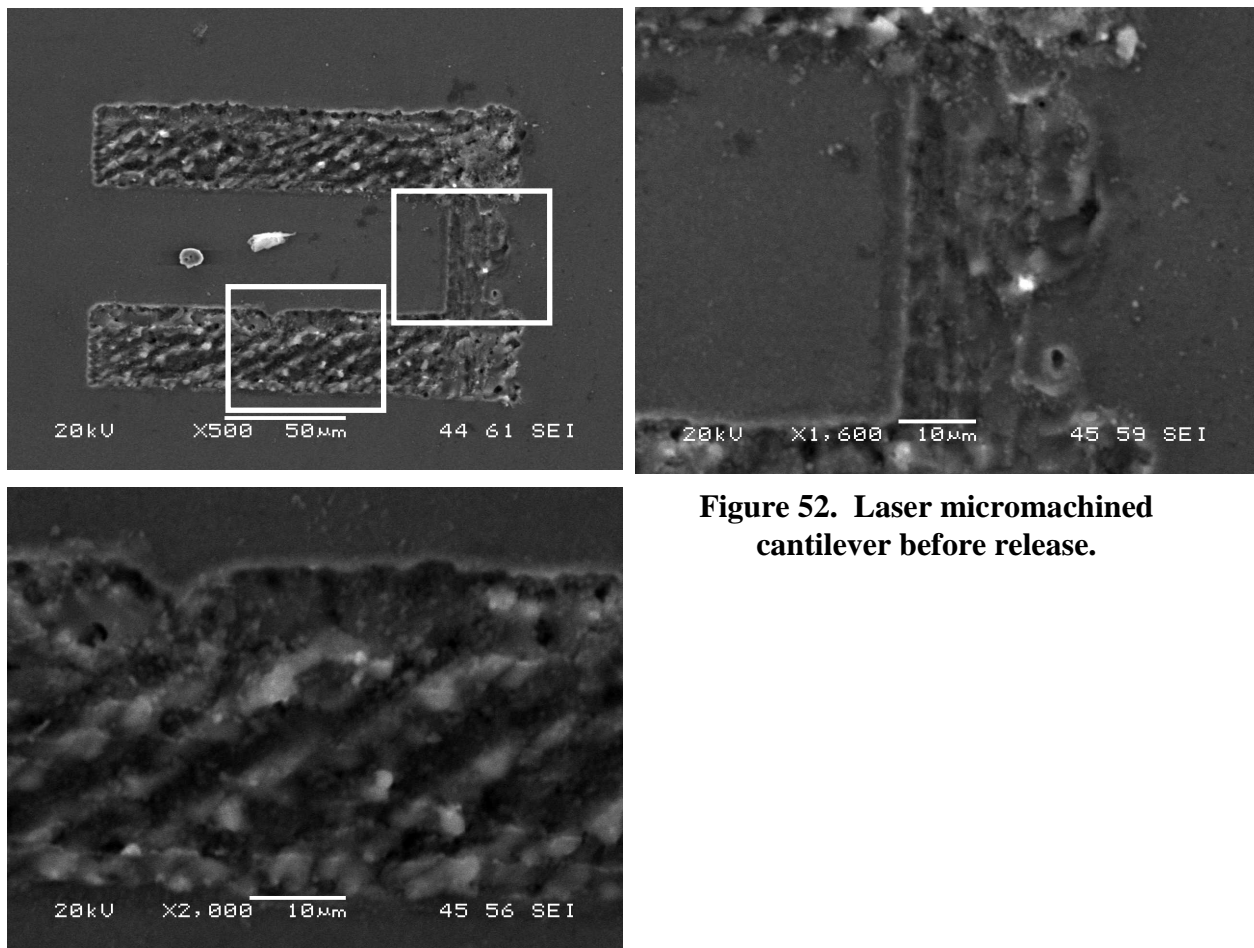


**Figure 52. Laser micromachined cantilever before release.**

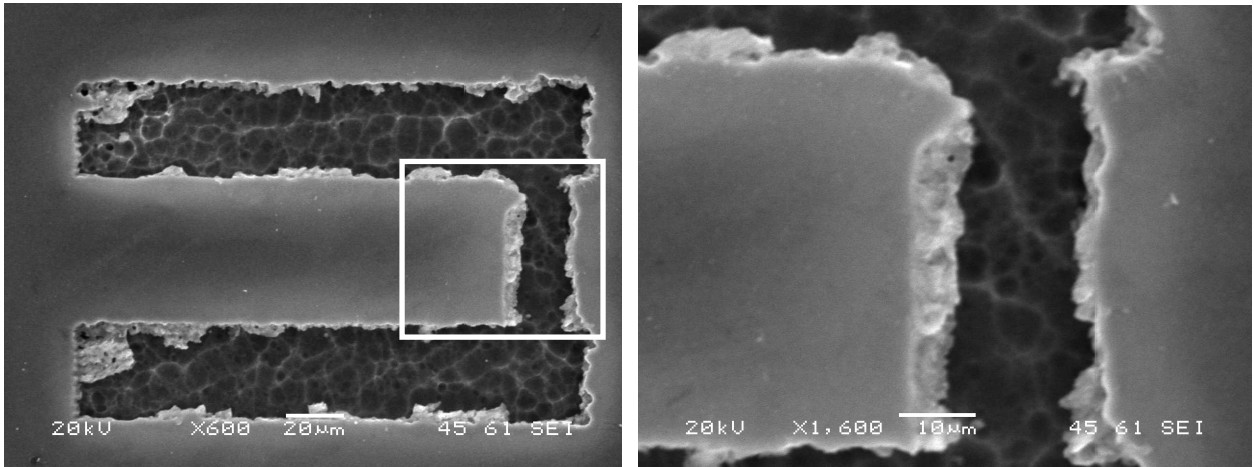


Figure 53. Cantilever structure after release

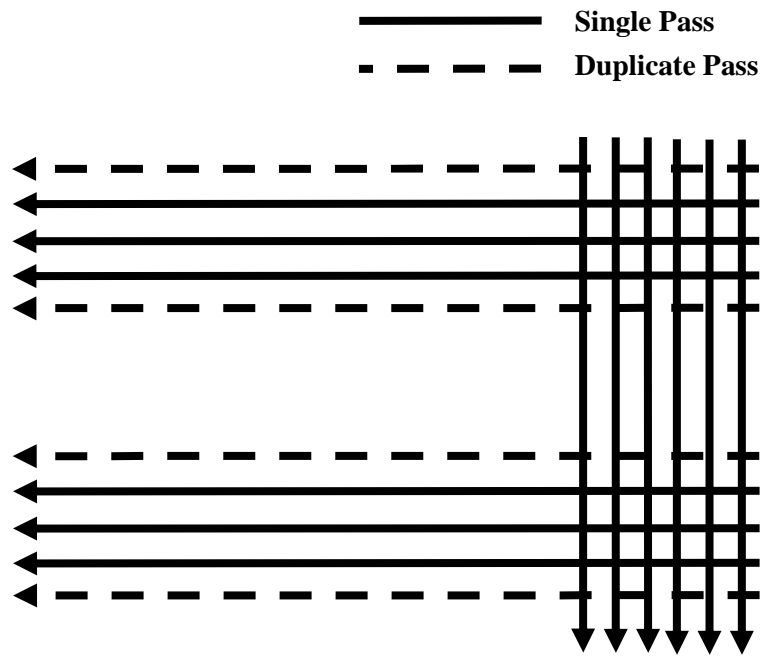
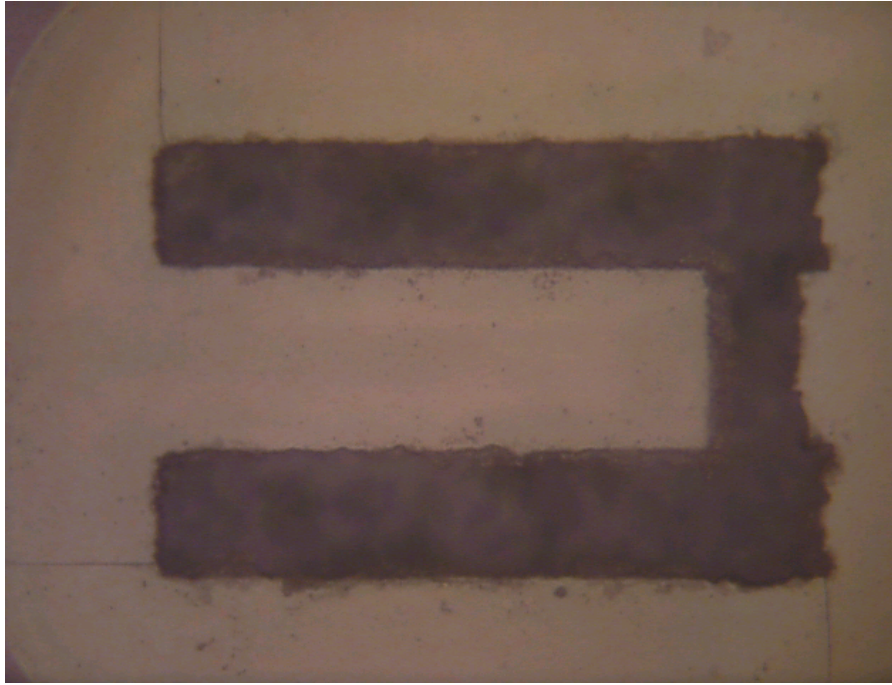


Figure 54. Cantilever micromachining schematic with duplicated passes to improve the edge quality



**Figure 55. Microscope image of a 3C-SiC cantilever fabricated using the finishing passes and released using the anisotropic etch**

Three samples were tested using an MTS Nano G200 indenter . Two samples  $75 \times 150 \mu\text{m}$  and one samples at  $100 \times 150 \mu\text{m}$  were tested. One of the  $75 \times 150 \mu\text{m}$  samples fractured upon testing. It is evident from the micrographs that Q-switched Nd:YAG laser micromachining of 3C-SiC on Si(100) results in the propagation of cracks that substantially reduce the functionality of the components. Alternative processes such as femtosecond laser micromachining and ICP processes result in structures with greater edge quality and do not suffer from thermally induced cracking.

**Table 17. 3C-SiC cantilever structure indentation testing**

<b>Sample</b>	<b>Size</b>	<b>Stiffness (N/m)</b>
1	100 x 150 μm	7.288
2	100 x 150 μm	7.892
3	75 x 150 μm	7.783

## References

1. Melzak, J.M., *Silicon Carbide for RF MEMS*. IEEE MTT-S International Microwave Symposium digest, 2003. **3**: p. 1629-1632.
2. Kripesh, V., et al., *Effect of Nd:YAG laser micromachining on gold conductor printed over ceramic substrates* Materials Letters, 2000. **44**(6): p. 347-351.
3. *Properties of Advanced Semiconductor Materials: GaN, AlN, InN, BN, SiC, SiGe*, ed. M.E. Levinshtein, S.L. Rumyantsev, and M.S. Shur. 2001, New York, NY, USA: John Wiley & Sons, Inc. 194.
4. Alavi, M., et al., *Laser machining of silicon for fabrication of new microstructures*, in *International Conference on Solid-State Sensors and Actuators*. 1991, IEEE: San Francisco, CA, USA. p. 512-515.
5. Alavi, M., et al., *Fabrication of microchannels by laser machining and anisotropic etching of silicon*. Sensors and Actuators A, 1992. **32**: p. 299-302.